The Pennsylvania State University

The Graduate School

Department of Meteorology

A THEORETICAL INVESTIGATION OF HYDROSTATIC AND GEOSTROPHIC ADJUSTMENT IN A COMPRESSIBLE ATMOSPHERE

A Thesis in

Meteorology

by

Jeffrey M. Chagnon

Submitted in Partial Fulfillment
of the Requirements
for the Degree of

Doctor of Philosophy

December 2003

The thesis of Jeffrey M. Chagnon has been reviewed and approved* by the following:

Peter R. Bannon
Professor of Meteorology
Thesis Advisor
Chair of Committee

Sukyoung Lee
Associate Professor of Meteorology

John H. E. Clark
Associate Professor of Meteorology

Sabih I. Hayek
Distinguished Professor Emeritus of
Engineering Science and Mechanics

William H. Brune
Professor of Meteorology
Head of the Department of Meteorology

*Signatures are on file in the Graduate School

ABSTRACT

The adjustment of a compressible, stably stratified atmosphere to sources of hydrostatic and geostrophic imbalance is investigated using a linear model. Imbalance is produced by prescribed, time-dependent injections of mass, heat, or momentum that model those processes considered "external" to the scales of motion on which the linearization and other model assumptions are justifiable. Solutions are demonstrated in response to localized warming characteristic of small isolated clouds, larger thunderstorms, and convective systems in order to determine how the spatial and temporal details of the injection affect the adjustment. The response to injections of different type (e.g. mass versus heat versus momentum) is also demonstrated in order to determine how the injection type affects the adjustment.

For a semi-infinite atmosphere, solutions consist of a set of vertical modes of continuously varying wavenumber, each of which contains time dependencies classified as steady, acoustic-wave, and buoyancy-wave contributions. Additionally, a rigid lower boundary condition implies the existence of a discrete mode - the Lamb mode - containing only a steady and acoustic-wave contribution. The forced solutions are generalized in terms of a temporal Green's function, which represents the response to an instantaneous injection.

The partitioning of the energy among the acoustic, buoyancy, and Lamb waves and the steady state is examined. The energy associated with each of these classes is distinct and, after the external injection is shut off, constant in time. The characteristics of

this partitioning depend on the spatial-temporal detail of the injection, as well as whether the imbalance is generated by injection of heat, mass, or momentum.

Injections that generate identical potential vorticity distributions constitute an interesting set of cases for comparison. Although the asymptotic steady state is identical in these cases, the energy of such potential-vorticity-equivalent injections depends on the manner by which the potential vorticity is introduced. If the potential vorticity is introduced rapidly rather than slowly, then more high frequency waves will be generated. Unlike the steady-state response, the transient response to a given injection may be very different than that to its averaged injection.

TABLE OF CONTENTS

LIST OF FIGURES

LIST OF TABLES

ACKNOWLEDGEMENTS

The National Science Foundation provided partial financial support for this work under grants ATM-9521299, -9820233, and -0215358. Professor Peter Bannon provided the patient and insightful scientific advising that made this endeavor possible. The critical review of this work by Professors Sukyoung Lee, John Clark, and Sabih Hayek significantly improved its quality. The professors of the many courses I took at Oswego and Penn State prepared me crucially to begin and finish this work independently.

The support I have received in my life outside of the university has been paramount to my ability to function effectively as a scientist. I therefore am foremost indebted to my parents Kathryn and Jeffrey who have always provided the most basic and unconditional emotional, financial, and developmental support. My mother would have liked to attend the Bronx High School of Science, and I hope this dissertation may in part be a surrogate for that missed experience. From my wife Rachael I receive the companionship and love whose value is beyond the capacity of the scientific method. From my siblings, grandparents, extended family, and friends I receive similarly invaluable support. Finally, the late Emil J. Chagnon and Dr. Karl J. Swyler were my intellectual role models whose presence and interest in my life directed me on a path toward the completion of this dissertation.

Chapter 1

Introduction

1.1 Definition of the Problem

Hydrostatic and geostrophic adjustment is the process by which a geophysical fluid evolves toward a state of hydrostatic and geostrophic balance. The process involves 1) the production of a localized unbalanced state, 2) the communication of the imbalance to the surrounding atmosphere by waves, and 3) the gradual establishment of a new balanced state. For example, atmospheric convection is a source of such imbalance. Viewed from the perspective of the larger-scale environment, rapid heating and the vertical redistribution of mass, thermal, and momentum fields associated with atmospheric convection generate an unbalanced configuration of the fields. Consequently, a spectrum of buoyancy and compression waves is generated. The waves propagate away from the source region and into the surrounding environment, adjusting the mass, thermal, and momentum fields toward a hydrostatic and geostrophic state that is in balance with the source region. This adjustment of the larger-scale environment to the localized imbalance by the action of waves is the subject of this thesis.

There are several reasons for investigating this topic. Foremost, it is a basic dynamical process of fundamental relevance to the theory of atmospheric dynamics. Furthermore, because the adjustment problem is defined in such a general manner, the theory may improve our understanding of a diverse range of phenomena. Such theoretical

investigation is crucial to the design of numerical models that simulate or parameterize these phenomena. Finally, the adjustment problem provides a convenient context for analyzing the applicability and limitations of such basic concepts as the potential vorticity and the spectral energy density.

This thesis adopts an analytic approach to investigate these issues. At the core of the analytic approach is a linear model of the larger-scale environment in which the adjustment takes place. The model is designed to provide insight into the aforementioned general theoretical issues concerning hydrostatic and geostrophic adjustment while also permitting demonstration of the dynamics of adjustment in specific cases.

1.2 Background

The hydrostatic and geostrophic adjustment problem has been the topic of many previous analyses. These studies have been conducted in a variety of theoretical and practical contexts with emphasis placed on a variety of features of the adjustment. Rossby (1937, 1938) first considered the geostrophic adjustment problem - the mutual adjustment of mass and velocity fields under the influence of the Earth's rotation - in a shallow water model subjected to a sudden, localized acceleration of the fluid. Rossby demonstrated that this accelerated "strip" of fluid would be Coriolis deflected to the right in the northern hemisphere, leading to an increase (decrease) in the fluid depth to the right (left) of the current and the production of horizontal pressure gradients. The initial imbalance between the mass and velocity fields generates surface gravity waves. Rossby solved for the state of the flow after these waves had propagated away - a steady, balanced state in

geostrophic balance characterized by a remainder of unconverted available potential energy (i.e. horizontal pressure gradients balanced by the geostrophic currents). Obukhov (1949) similarly considered the "adaptation" of a rotating fluid to an external disturbance, noting the problem of geostrophic degeneracy and the need for potential vorticity consideration in order to solve for the asymptotic steady state. Lamb (1932) considered the hydrostatic adjustment problem - the response of a fluid in the vertical direction to an imbalance between the upward directed pressure gradient force and the weight of the fluid column. Lamb's problem consisted of an initially resting, compressible atmosphere subjected to a prescribed harmonic vibration in the vertical momentum field confined to a horizontal plane (i.e. an infinitesimally deep disturbance). The disturbance was communicated to the surrounding environment by rapid, vertically propagating acoustic waves that displace the fluid vertically in order to establish hydrostatic balance.

A series of papers followed Rossby's seminal investigation of geostrophic adjustment. Cahn (1949) contributed the time-dependent solution to Rossby's adjustment problem. The initial elevation and depression of the ocean surface were shown to propagate away from the source region as gravity wave fronts with velocity $(g\ D_0)^{1/2}$, (where D_0 is the undisturbed depth of the ocean), leaving behind an inertial oscillation of decaying amplitude superimposed on the steady state. Bolin (1953) further improved upon Cahn's solution by considering Rossby's adjustment problem in a density-stratified fluid with a depth-dependent basic state velocity profile. The initial imbalance generated a spectrum of internal gravity waves whose propagation velocities are slightly smaller than that of the external surface-gravity waves of Rossby's adjustment. An examination of the energetics of Rossby's adjustment problem was performed by Veronis (1956). This

analysis demonstrated that for a slowly generated imbalance a larger fraction of the added energy is retained by the geostrophic motions of the steady state. For an impulsively generated imbalance a minimum energy fraction of 26% is retained by the geostrophic motion - the remaining 74% is lost to the inertia-gravity waves.

Following these benchmark studies, investigators have applied the hydrostatic and geostrophic adjustment problem to a variety of particular geophysical flows. Blumen (1972) and Gill (1982) have provided general reviews of the theoretical aspects of adjustment, including classification and description of the transient features and energetics. A compressible, density-stratified fluid under the influence of gravity, such as the atmosphere, may contain acoustic waves, internal gravity waves, and hydrostatic waves of compression, i.e. Lamb waves. Under the influence of Earth's rotation, an inertial oscillation interacts with these waves, limiting the maximum wave period to one half of a pendulum day. The frequency of the internal gravity waves may not exceed the buoyancy frequency, whereas the frequency of the acoustic waves may not be less than the acoustic cut-off frequency.

The wide variety of physical circumstances addressed in investigations of adjustment underscores the relevance of this problem to geophysical fluid dynamics. The specific physical circumstance addressed in a study is usually incorporated into the nature of the initial imbalance. These localized sources of imbalance may be categorized as momentum, mass, or heat injections. Although convenient for organizational purposes, these strict categories do not uniquely or completely describe all physical circumstances of interest. For example, convection may be modeled as either a mass or heat source. Additionally, several investigators considered the response of a compressible atmosphere

to localized energy sources (Pierce 1963, Cole and Greifinger 1969) such as those generated by atomic blasts or volcanic eruptions.

An example of a momentum injection problem is the classic Rossby adjustment problem, which models the initial response of an ocean to the sudden addition of momentum to a "strip" of ocean by the surface wind stress. A recent example was that considered by Vadas and Fritts (2001). The deposition of momentum into stratospheric flow by breaking or dissipating gravity waves is hypothesized to be a secondary source of gravity waves. Lane et al. (2001) demonstrated that the buoyancy waves emerging from a numerically simulated convective storm originated primarily from terms in the vertical momentum equation associated with the accelerating updraft. In fact, those sources were much larger than those originating in the heat equation.

Examples of mass injection problems are found commonly throughout physical oceanography. The rapid production of horizontal density gradients in large bodies of water by "sudden convection" and the subsequent geostrophic adjustment has been studied by a large number of investigators (e.g. Csanady 1971, Ou 1983, 1984, Gill 1982, Glendening 1993, Blumen and Wu 1995a,b). An unbalanced horizontal density gradient is imposed in each of these studies to represent the consequence of rapid overturning in a differentially cooled body of water. The adjustment of an ocean to isolated convective plumes has been modeled by McDonald (1990). Glendening (1993) describes these investigations as complementary to Rossby's geostrophic adjustment, which treat "...the adjustment of a horizontally homogeneous *momentum* field to a horizontally varying *mass* forcing." Gill (1982) presents a complete discussion of the adjustment of an ocean to an initially displaced ocean surface under the influence of rotation. The adjustment to

mass sources has also been studied in atmospheric contexts. Bretherton (1988) suggests that flow over fluid or rigid obstacles may be equivalently modeled as sources of mass. Raymond (1983) investigated the effect of gravity waves generated by mass flux divergence in cumulus clouds on the generation and maintenance of convection. Shutts (1994) suggests that the convective redistribution of mass by large thunderstorms may be modeled as a dipole of mass source/sink. Such a simple conceptualization of the effects of convection on the larger scale environment is suggested as a potential cumulus parameterization for coarse-resolution numerical models.

Convection embedded in a large-scale flow may also be modeled as a heat source, such as that which may be the result of latent heating due to phase changes within a cloud. The conceptualization of isolated convection as a "warm bubble" or region of positive buoyancy rising from the surface is another justification for modeling convection as a heat source. The adjustment to such localized heat sources as representations of convection has been considered by a large number of authors (e.g. Lin and Smith 1986, Raymond 1986, Bretherton and Smolarkiewicz 1989, Nicholls et al. 1991, Nicholls and Pielke 1994a,b, Nicholls and Pielke 2000, Lane and Reeder 2001). Heat sources may also be applied to model other disturbances. For example, Bannon (1995) suggests that the rapid radiative heating of a stratus layer may be modeled as a horizontally homogeneous heat source of finite vertical extent. Tjim and Van Delden (1999) consider the generation of acoustic and gravity waves by the differential heating associated with the initiation of a sea-breeze. Vadas and Fritts (2001) employ a heat source to model heating due to gravity wave dissipation in the stratosphere. Given such a wide range of potential initial

imbalance mechanisms, it is prudent to investigate the extent to which injection of different types induce equivalent responses.

Another issue fundamental to the linear adjustment problem is the relationship between the characteristics of the imbalance and that of the preferentially excited waves. The vertical, horizontal, and temporal structures of a wave are given by an eigenvalue (dispersion) equation. Vadas and Fritts (2001) demonstrated that an injection of duration much longer than the characteristic period of a given buoyancy wave will not project a significant proportion of energy onto such waves. Holton et al (2002) makes a similar argument to challenge the popular notion that the dominant gravity waves generated by convective heating have vertical wavelength equal to twice the depth of the heating. These analyses are an improvement on many previous analyses that simply prescribe an unbalanced initial condition. The latter design is tantamount to prescribing an impulsive injection, overstates the role of particular wave modes in an adjustment process, and does not adequately address the origin of the injection in the governing equations.

The overwhelming majority of studies have employed incompressible models. Fully compressible models are inherently more complicated given the existence of acoustic and Lamb waves. However, compressible numerical codes are growing in popularity (e.g. Bryan and Fritsch, 2002). It is therefore necessary to analyze the potential effects of compressibility on basic atmospheric processes such as geostrophic and hydrostatic adjustment. Chagnon and Bannon (2001) demonstrated that the steady-state solutions in anelastic and other sound filtering models exhibit significant differences from a fully compressible model. Bannon (1995) theorizes that acoustic waves can provide the vertical displacements necessary to adjust a heated cloud layer toward

hydrostatic balance. In a fully compressible numerical simulation of an isolated convective cloud, Nicholls and Pielke (2000) identified a Lamb wave propagating away from the cloud containing internal and gravitational potential energy approximately equal to the total latent heating within the cloud.

1.3 Statement of Intent

This thesis investigates the acoustic-, Lamb-, and buoyancy-wave response to rapid, localized sources of hydrostatic and geostrophic imbalance. In particular, our goal is to determine how the following qualities of a model affect the qualities of adjustment: 1) the spatial and temporal detail as well as type of injection, 2) fully compressible dynamics with a rigid lower boundary. We intend to describe the transient response to a given injection according to several regimes dominated by acoustic waves, nonhydrostatic buoyancy waves, Lamb waves, or inertia-gravity waves. The association of the various response regimes to a given imbalance generation mechanism may then be examined in terms of the spatial and temporal detail and type of the injection.

The investigation consists of two primary parts: Chapter 3 presents the time-dependent solution of a linear model in order to illustrate the various response regimes. Chapter 4 examines the potential vorticity and total energy of the model, the latter of which is partitioned among the various wave classes. Motivated by Nicholls and Pielke (2000) and Chagnon and Bannon (2001), the model is fully compressible with a rigid lower boundary and therefore contains Lamb and acoustic waves. We seek to determine

under what circumstances the effects of compressibility may be significant to hydrostatic and geostrophic adjustment.

Chapter 2

Analytic Approach

2.1 The Model

The framework for this investigation is a compressible, dry, inviscid model atmosphere in Cartesian coordinates that is linearized on an *f*-plane about an isothermal, resting base state and is homogeneous in the *y*-direction. This highly idealized model is chosen for its tractability while maintaining many essential physical characteristics of mid-latitude, large-scale atmospheric flows. The assumption of homogeneity in one horizontal dimension conveniently separates the dynamic effects associated with the divergent from the Coriolis-deflected portions of the horizontal motion. The nonhomogeneous terms in the model represent injections of mass, momentum, and heat by the smaller-scale and/or smaller amplitude disturbances. The governing equations are

$$\bar{\rho}_s \frac{\partial u'}{\partial t} = -\frac{\partial p'}{\partial x} + \bar{\rho}_s f v' + \bar{\rho}_s \dot{u} \quad , \tag{2.1a}$$

$$\bar{\rho}_s \frac{\partial v'}{\partial t} = -\bar{\rho}_s f u' + \bar{\rho}_s \dot{v} \quad , \tag{2.1b}$$

$$\bar{\rho}_s \frac{\partial w'}{\partial t} = -\frac{\partial p'}{\partial z} - \rho' g + \bar{\rho}_s \dot{w} \quad , \tag{2.1c}$$

$$\frac{\partial \rho'}{\partial t} + w' \frac{\partial \bar{\rho}_s}{\partial z} = 0 \quad , \tag{2.1d}$$

$$\frac{\partial \rho'}{\partial t} + \frac{\partial}{\partial x}(\bar{\rho}_s u') + \frac{\partial}{\partial z}(\bar{\rho}_s w') = 0 \quad , \tag{2.1e}$$

$$\frac{\rho'}{\bar{\rho}_s} = \frac{p'}{\bar{p}_s} - \frac{T'}{\bar{T}_s} \quad , \tag{2.1f}$$

where g is the acceleration due to gravity, f is the constant Coriolis parameter, and $\gamma = c_p/c_v = 1.4$ is the ratio of specific heat capacities. A subscript s denotes a static, base-state quantity, and a superscript prime denotes a perturbation from the base state. The base-state quantities are assumed to be functions of height only [e.g. $p(x, z, t) = p_s(z) + p'(x, z, t)$)]. The isothermal base state is described by

$$\begin{aligned} T_s &= T_* \ , \\ p_s &= p_* \exp(-z / H_s) \ , \\ \rho_s &= \rho_* \exp(-z / H_s) \ , \\ \theta_s &= \theta_* \exp(\kappa z / H_s) \ , \end{aligned} \tag{2.2}$$

where T_* , p_* , ρ_* , and θ_* are constants satisfying the ideal gas law and Poisson's relation. Here, $\kappa = R/c_p$, and $H_s = RT_s/g$ is the density scale height in an isothermal atmosphere. The rates of injection of x-momentum, y-momentum, z-momentum, potential temperature, and density are represented by $\dot{u}$, $\dot{v}$, $\dot{w}$, $\dot{\theta}$, and $\dot{\rho}$, respectively and have arbitrary spatial and temporal structure.

The model equations are simplified by the introduction of "field variables", which remove any height dependence of the coefficients in the system of partial differential equations (Eckart 1960). The field variables are defined as

$$\begin{aligned} \mathbf{U} &= \rho_s^{1/2} \, \mathbf{u} \ , \\ P &= \frac{1}{\rho_s^{1/2}} \, p' \ , \\ R &= \frac{1}{\rho_s^{1/2}} \, \rho' \ , \\ S &= \frac{\rho_s^{1/2}}{\rho_s} \, \theta' \ . \end{aligned} \tag{2.3}$$

Applying (2.3) to (2.1) we obtain the simplified system of equations:

$$\frac{\partial \underset{\sim}{\square}}{\partial t} + \underset{\approx}{\mathbf{A}}\,\underset{\sim}{\square} = \underset{\sim}{\mathbf{F}} \quad , \tag{2.4}$$

where the solution state vector is $\underset{\sim}{\square}^{\mathbf{T}} = (U,\ V,\ W,\ S,\ P)$, the matrix operator $\underset{\approx}{\mathbf{A}}$ is given by

$$\underset{\approx}{\mathbf{A}} = \begin{bmatrix} 0 & -f & 0 & 0 & \dfrac{\partial}{\partial x} \\ f & 0 & 0 & 0 & 0 \\ 0 & 0 & 0 & -g & \dfrac{\partial}{\partial z} + \square \\ 0 & 0 & \dfrac{\square}{H_s} & 0 & 0 \\ c_s^2 \dfrac{\partial}{\partial x} & 0 & c_s^2 \left(\dfrac{\partial}{\partial z} - \square \right) & 0 & 0 \end{bmatrix} \quad , \tag{2.5}$$

where Eckart's (1960) vertical expansion parameter is defined as

$$\square \equiv \left(\frac{1}{\square} - \frac{1}{2} \right) \frac{1}{H_s} \quad , \tag{2.6}$$

and the injection vector is $\underset{\sim}{\mathbf{F}} = (\dot{U},\ \dot{V},\ \dot{W},\ \dot{S},\ \dot{P})$ where the mass-weighted injection terms are given by

$$\begin{gathered} (\dot{U}, \dot{V}, \dot{W}) = \square_s^{1/2} (\dot{u}, \dot{v}, \dot{w}) , \dot{R} = \square_s^{-1/2} \square \ , \\ \dot{S} = \frac{\square_s^{1/2}}{\square_s} \square \quad . \end{gathered} \tag{2.7}$$

The density field may be obtained via the transformed Poisson's relation $P = c_s^{\,2}\,(S + R)$. The horizontal dependence of the fields is represented by a Fourier transform,

$$\begin{aligned} \square_k (k) &= \int_{-\infty}^{\infty} \square(x)\, e^{-i k x} \, dx \quad , \\ \square(x) &= \frac{1}{2\square} \int_{-\infty}^{\infty} \square_k (k)\, e^{i k x} \, dk \quad , \end{aligned} \tag{2.8}$$

where $i = \sqrt{-1}$. Under the transform (2.8) the operator $\underset{\approx}{\mathbf{A}}$ becomes

$$\underset{\approx}{\mathbf{A}} = \begin{bmatrix} 0 & -f & 0 & 0 & ik \\ f & 0 & 0 & 0 & 0 \\ 0 & 0 & 0 & -g & \frac{\partial}{\partial z} + \square \\ 0 & 0 & \frac{\square}{H_s} & 0 & 0 \\ ik\, c_s^2 & 0 & c_s^2 \left(\frac{\partial}{\partial z} - \square \right) & 0 & 0 \end{bmatrix} .$$

The subscript k denoting the Fourier transform is hereafter dropped. Our goal is to solve (2.4) subject to the initial condition that all of the fields are undisturbed for $t < 0$,

$$\underset{\sim}{\square} = \underset{\sim}{0} \ , \ t < 0 \ , \tag{2.9}$$

and the boundary conditions that $w = 0$ at heights $z = 0, 2D$,

$$\left(\left(\frac{\partial}{\partial z} + \square \right) U \ , \left(\frac{\partial}{\partial z} + \square \right) V \ , W, S, \left(\frac{\partial}{\partial z} + \square \right) P \right) = \underset{\sim}{0}^{\mathbf{T}} \ , z = 0, 2D \ . \tag{2.10}$$

The application of the homogeneous boundary condition (2.10) is valid when the injection is zero on the boundaries. The structure of the solutions in the semi-infinite atmosphere is identical to those in the finite atmosphere in the limit as $D \to \infty$. The practical application of the solution procedure is restricted to a finite domain, which must be that of a finite atmosphere. The rigid lower boundary condition implies the existence of a boundary wave (i.e. a wave with maximum amplitude along the boundary whose existence is owed to the presence of the boundary), which we identify as the Lamb wave (Lamb 1932, section 311a). We need not worry about a spurious boundary wave corresponding to the rigid upper boundary, because $g > N_s c_s$ (Iga 2001) where $N_s = (g/\square_s)\, d\square_s/dz$ is the buoyancy

frequency. The Lamb wave is a hydrostatic, adiabatic, horizontally propagating wave that responds to changes in the column pressure that act against the rigid lower boundary.

2.2 Homogeneous Solutions

Examination of the homogeneous solutions of (2.4) reveals the fundamental dynamic components of the adjustment process. We look for separable solutions: $\underset{\sim}{\square}^{T} = ($ $U_n(t)f_n(z)$, $V_n(t)f_n(z)$, $W_n(t)g_n(z)$, $S_n(t)g_n(z)$, $P_n(t)f_n(z)$ $)$. Two distinct vertical structure functions f_n and g_n are sought to satisfy the distinct vertical boundary conditions in (2.10). For W and S we require $g_n = 0$ on the boundaries, and for U, V, and P we require $[d/dz + \square]f_n = 0$ on the boundaries. Substituting the separable form of $\underset{\sim}{\square}$ into the homogeneous form of (2.4) implies that the vertical structure functions must satisfy

$$f_n''(z) + m^2 f_n(z) = 0 \quad , g_n''(z) + m^2 g_n(z) = 0 \quad , \tag{2.11a,b}$$

where the vertical decay scale m is a constant of proportionality between the vertical and temporal structure equations. The simple form of (2.11) gives way to more complicated forms when the base state is spatially varying (e.g. Fritts and Yuan 1989). Because (2.11) are Sturm-Liouville boundary-value problems, the collection of linearly independent solutions forms orthogonal basis sets between the boundaries. These sets are given by

$$\begin{gathered} f_0 \, , f_1 \, , f_2 \, , f_3 \, , \ldots \quad ; \\ f_0 = e^{-mz} \; where \; m = \square \quad , \\ f_n = m \cos[mz] - \square \sin[mz] \quad where \quad m = \frac{n\square}{2D} \quad , \end{gathered} \tag{2.12a}$$

and

$$(g_0 = 0), g_1, g_2, g_3, \ldots$$
$$g_n = \left[\frac{d}{dz} + \right] f_n = -(m^2 + \,^2)\sin[m z] \quad where \quad m = \frac{n}{2D} \quad . \tag{2.12b}$$

Here and elsewhere, *mode* refers to a specific spatial structure given by the set (2.12) with the Fourier transform. Note that in the semi-infinite limit the discrete wavenumber m becomes continuous. The zeroth vertical mode f_0 is the Lamb mode that is hydrostatic and contains zero entropy and remains discrete in the semi-infinite limit. Figure 2.1 plots the profile of the first three modes in (2.12). The modes describing the vertical velocity are zero on the boundaries. With the exception of the Lamb mode, the modes describing the pressure have equal magnitude on the upper and lower boundary but alternate between equal and opposite signs. The solution may be written as a linear combination of the vertical basis functions,

$$\underset{\sim}{}^T = \sum_{n=0} (U_n f_n, V_n f_n, W_n g_n, S_n g_n, P_n f_n) \quad . \tag{2.13}$$

The time dependence of the n-th mode must satisfy

$$\frac{d\underset{\sim}{n}}{dt} + \underset{\approx}{\mathbf{A_n}}\,\underset{\sim}{n} = 0 \quad , \tag{2.14}$$

where $\underset{\sim}{\mathbf{n}}^{\mathbf{T}} = (U_n, V_n, W_n, S_n, P_n)$, and

$$\underset{\approx}{\mathbf{A_n}} = \begin{bmatrix} 0 & -f & 0 & 0 & ik \\ f & 0 & 0 & 0 & 0 \\ 0 & 0 & 0 & -g & 1 \\ 0 & 0 & \frac{}{H_s} & 0 & 0 \\ ik\,c_s^2 & 0 & -c_s^2(m^2 + \,^2) & 0 & 0 \end{bmatrix} \tag{2.15}$$

The eigenvalues of $\underset{\approx}{\mathbf{A_n}}$ are the five roots of the dispersion relation

$$\omega_i \left(\omega_i^4 + \beta \omega_i^2 + \gamma \right) = 0 \quad , \tag{2.16}$$

where

$$\beta = \left(c_s^2 k^2 + f^2 \right) + c_s^2 \left(\alpha^2 + m^2 \right) + N_s^2 \quad ,$$
$$\gamma = c_s^2 f^2 \left(\alpha^2 + m^2 \right) + N_s^2 \left(c_s^2 k^2 + f^2 \right) \quad .$$

Solutions of (2.14) have temporal dependence $e^{-i\omega t}$, as will be demonstrated below. The eigenvalue $\omega_1 = 0$ corresponds to a steady solution. The four other eigenvalues are complex: $\omega_{2,3} = +/- i \omega_a$, $\omega_{3,4} = +/- i \omega_b$ where ω_a and ω_b are frequencies characteristic of acoustic and buoyancy waves, respectively. Figure 2.2 presents the dependence of the frequencies on the horizontal k and vertical m wavenumbers. Equation (2.16) and Fig. 2.2 suggest three classes of time dependence for each mode: steady, acoustic-wave, and buoyancy-wave. Here and elsewhere, *class* refers to these time dependencies. The Lamb mode contains only two classes: steady and acoustic-wave (i.e. the Lamb wave). The buoyancy frequency cannot exceed N_s, whereas the acoustic waves have lower bound $N_a = c_s/2H_s$, the acoustic cut-off frequency. The lower bound on all oscillations is twice the angular velocity of the coordinate frame f. A similar diagram exists in Gill (1982, Fig. 6.18) for the nonrotating case ($f = 0$), but is provided here as a convenient reference for the interpretation of the solutions presented in chapter 3 and the energetics of chapter 4.

The eigenvectors of $\underset{\sim}{\mathbf{A}}_{\mathbf{n}}$ are

$$\mathbf{e}_{\mathbf{i}}^{\mathbf{T}} = P_n \left(\frac{i k \omega_i}{\omega_i^2 + f^2} , \frac{i k f}{\omega_i^2 + f^2} , \frac{\omega_i}{\omega_i^2 + N_s^2} , \frac{\omega / H_s}{\omega_i^2 + N_s^2} , 1 \right) \quad . \tag{2.17}$$

Figure 2.1

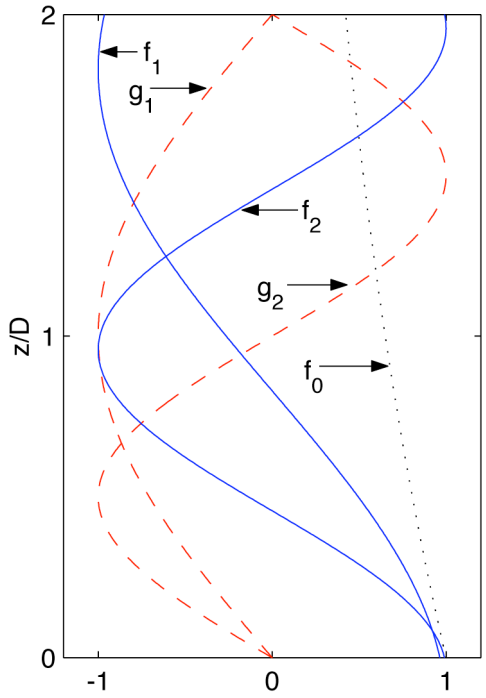

Figure 2.1: Vertical profiles of the first three vertical basis functions. The pressure and horizontal velocity fields are described by f_n. The potential temperature and vertical velocity fields are described by g_n. The Lamb mode is f_0. Here, D = 15 km, H_s = 7.47 km.

Let $\underset{\approx}{\mathbf{E}}_{\mathbf{n}}$ be the matrix whose columns vectors are the eigenvectors (2.17),

$$\underset{\approx}{\mathbf{E}}_{\mathbf{n}} \equiv \left[\underset{\sim}{\mathbf{e}}_1 : \underset{\sim}{\mathbf{e}}_2 : \underset{\sim}{\mathbf{e}}_3 : \underset{\sim}{\mathbf{e}}_4 : \underset{\sim}{\mathbf{e}}_5\right]_{\mathbf{n}} . \tag{2.18}$$

The matrix $\underset{\approx}{\mathbf{E}}_{\mathbf{n}}^{-1}\ \underset{\approx}{\mathbf{A}}_{\mathbf{n}}\ \underset{\approx}{\mathbf{E}}_{\mathbf{n}}$ is the diagonal matrix containing the eigenvalues ω_i.

Transforming $\underset{\sim}{\Phi}_{\mathbf{n}} = \underset{\approx}{\mathbf{E}}_{\mathbf{n}}\ \underset{\sim}{\Psi}_{\mathbf{n}}$ implies that $d\underset{\sim}{\Psi}_{\mathbf{n}}/dt = -\underset{\approx}{\mathbf{E}}_{\mathbf{n}}^{-1}\ \underset{\approx}{\mathbf{A}}_{\mathbf{n}}\ \underset{\approx}{\mathbf{E}}_{\mathbf{n}}\ \underset{\sim}{\Psi}_{\mathbf{n}}$. The i-th element of $\underset{\sim}{\Psi}_{\mathbf{n}}$ is therefore $\Psi_i = C_i\ exp(-\omega_i t)$ where C_i is constant. That is, the 5 elements of the transformed solution vector correspond to steady, acoustic-wave, and buoyancy-wave classes. The solution vector is therefore given by

$$\underset{\sim}{\Phi}_{\mathbf{n}} = \begin{bmatrix} 0 & \frac{-k\,\omega_a}{f^2 - \omega_a^2} & \frac{k\,\omega_a}{f^2 - \omega_a^2} & \frac{-k\,\omega_b}{f^2 - \omega_b^2} & \frac{k\,\omega_b}{f^2 - \omega_b^2} \\ \frac{i\,k}{f} & \frac{i\,k\,f}{f^2 - \omega_a^2} & \frac{i\,k\,f}{f^2 - \omega_a^2} & \frac{i\,k\,f}{f^2 - \omega_b^2} & \frac{i\,k\,f}{f^2 - \omega_b^2} \\ 0 & \frac{i\,\omega_a}{N_s^2 - \omega_a^2} & \frac{-i\,\omega_a}{N_s^2 - \omega_a^2} & \frac{i\,\omega_b}{N_s^2 - \omega_b^2} & \frac{-i\,\omega_b}{N_s^2 - \omega_b^2} \\ \frac{1}{g} & \frac{\omega / H_s}{N_s^2 - \omega_a^2} & \frac{\omega / H_s}{N_s^2 - \omega_a^2} & \frac{\omega / H_s}{N_s^2 - \omega_b^2} & \frac{\omega / H_s}{N_s^2 - \omega_b^2} \\ 1 & 1 & 1 & 1 & 1 \end{bmatrix}_n \begin{bmatrix} C_1 \\ C_2\, e^{-i\,\omega_a t} \\ C_3\, e^{i\,\omega_a t} \\ C_4\, e^{-i\,\omega_b t} \\ C_5\, e^{i\,\omega_b t} \end{bmatrix}_n . \tag{2.19}$$

The constants C_i are determined by the initial conditions. The column vectors of $\underset{\approx}{\mathbf{E}}_{\mathbf{n}}$ describe the structure of the steady, acoustic-wave, and buoyancy-wave classes that contribute to the homogeneous solution of the n-th mode. The first column vector gives the structure of the hydrostatic and geostrophic contribution, which contains zero contribution from the U and W fields. The next four column vectors indicate the structure

of the acoustic and buoyancy waves. A 90 degree temporal phase difference exists between the *U,W* and *P,V,S* fields. A 90 degree horizontal phase difference exists between the *U,V* and *P,W,S* fields. Because the frequency of the acoustic and buoyancy waves depend differently on the modal parameters *m* and *k*, the characteristics of energy propagation will differ between these wave classes. In particular, the phase and group velocities are orthogonal for the buoyancy waves and parallel for the acoustic waves.

Figure 2.2

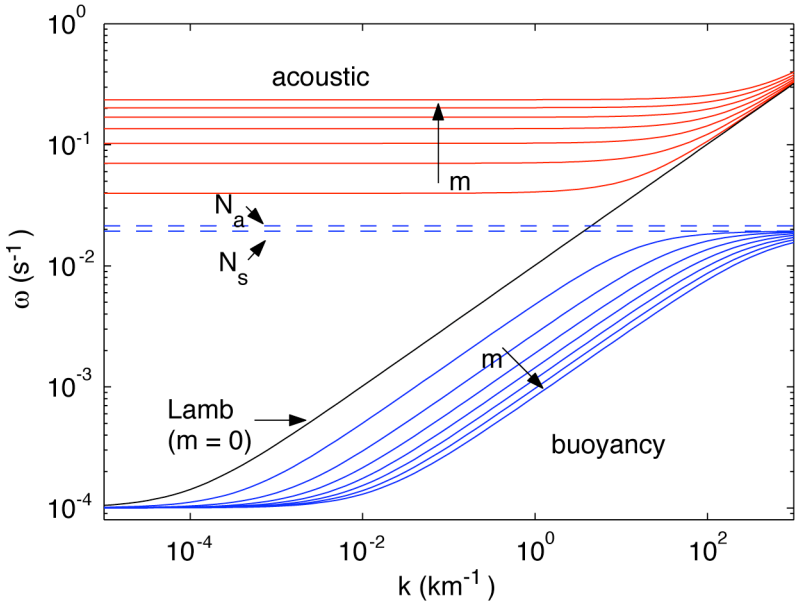

Figure 2.2: Dispersion curves for the first eight vertical modes *m* as a function of the horizontal wavenumber *k*. Here, T_s = 255 K and the domain depth is 2D = 30 km. The acoustic cut-off frequency is N_a = .0214 s^{-1} , the maximum buoyancy frequency is N_s = .0194 s^{-1}, and $f = 10^{-4}$ s^{-1}.

2.3 Response to External Injection

We seek the solution to the nonhomogeneous form of (2.4) using the properties of the homogeneous solutions. If the injection vector is expanded about the vertical basis functions,

$$\underset{\sim}{\mathbf{F}}^{\mathbf{T}} = \Box_t(t)\,\Box_k(k) \sum_{n=0} \left(s_{U,n} f_n(z) , s_{V,n} f_n(z) , s_{W,n} g_n(z) , s_{S,n} g_n(z) , s_{P,n} f_n(z) \right) , \quad (2.20)$$

where $\Box_t$ is the time dependence of the injection, $\Box_k$ is the Fourier transformed horizontal dependence of the injection, and the $s_{\Box,n}$ are the projections onto the vertical modes, then (2.4) may be written as

$$\frac{d\underset{\sim}{\Box_{\mathbf{n}}}}{dt} + \underset{\approx}{\mathbf{A}_{\mathbf{n}}}\,\underset{\sim}{\Box_{\mathbf{n}}} = \underset{\sim}{\mathbf{F}_{\mathbf{n}}} \quad , \quad (2.21)$$

where $\underset{\sim}{\mathbf{F}}_{\mathbf{n}}^{\mathbf{T}} = \Box_t\,\Box_k(s_{U,n},\, s_{V,n},\, s_{W,n},\, s_{S,n},\, s_{P,n})$. The particular solution of (2.21) may be expressed in terms of the temporal Green's function $\underset{\sim}{\widehat{\Box}_{\mathbf{n}}}$,

$$\underset{\sim}{\Box_{\mathbf{n}}}(t) = \int_0^t \underset{\sim}{\Box_{\mathbf{n}}}(t - t')\,\Box_t(t')\,dt' . \quad (2.22)$$

The Green's function is the particular solution of

$$\frac{d\underset{\sim}{\Box_{\mathbf{n}}}}{dt} + \underset{\approx}{\mathbf{A}_{\mathbf{n}}}\,\underset{\sim}{\Box_{\mathbf{n}}} = \underset{\sim}{\widehat{\mathbf{F}}_{\mathbf{n}}} \quad , \quad (2.23)$$

where $\underset{\sim}{\widehat{\mathbf{F}}}_{\mathbf{n}}^{\mathbf{T}} = \Box(t)\,\Box_k(s_{U,n},\, s_{V,n},\, s_{W,n},\, s_{S,n},\, s_{P,n})$. We may look for a solution $\underset{\sim}{\Box_{\mathbf{n}}}$ of (2.23) resembling that of the homogeneous problem given by (2.19), i.e. $\underset{\sim}{\widehat{\Box}_{\mathbf{n}}} = \underset{\approx}{\mathbf{E}_{\mathbf{n}}}\,\underset{\sim}{\Box_{\mathbf{n}}}$. The conditions on the constants C_i of $\underset{\sim}{\Box_{\mathbf{n}}}$ are found by integrating (2.23) about an

infinitesimal region in time containing $t = 0$ and applying the initial condition that $\hat{\underset{\sim}{\Gamma}}_{\mathbf{n}} = \underset{\sim}{0}$ for $t < 0$. The constants must therefore satisfy the linear system given by

$$lim_{t \to 0^+} \left(\underset{\approx}{\mathbf{E}}_{\mathbf{n}} \underset{\sim}{\Gamma}_{\mathbf{n}} \right) = lim_{\Delta \to 0} \int_{-\Delta}^{\Delta} \underset{\approx}{\hat{\mathbf{F}}}_{\mathbf{n}} \, dt \ , \tag{2.24}$$

which may be solved readily upon inverting the eigenvector matrix $\underset{\approx}{\mathbf{E}}_{\mathbf{n}}$. Appendix A provides the solution of (2.24). Although the form of the coefficients given by (A1-A5) is not extremely elegant, we may still recognize some physically meaningful properties. For example, the coefficient of the steady contribution C_1 is zero when the injection is by x-velocity or vertical velocity, neither of which may generate potential vorticity (see section 4.5). For these same injections $C_2 = -C_3$, $C_4 = -C_5$, which implies that the pressure field varies like a sine in time and is initially zero. For an injection of y-velocity $C_2 = C_3$, $C_4 = C_5$ which implies pressure varies like a cosine in time that is exactly offset by the steady contribution initially. For injection of heat or mass the solution contains a steady state (C_1 nonzero) and varies like a cosine in time with nonzero initial perturbation.

The temporal convolution (2.22) may be expressed as $\underset{\sim}{\Gamma}_{\mathbf{n}}(t) = \underset{\approx}{\mathbf{E}}_{n} \, \underset{\sim}{\mathbf{G}}_{\mathbf{n}}(t)$ where the i-th element of $\underset{\sim}{\mathbf{G}}_{\mathbf{n}}(t)$ is $G_{n,i} = c_i(t) \, exp(i \omega_i t)$ with

$$c_i(t) = C_i \int_0^t e^{-i \omega_i t'} \Phi_I(t') \, dt' . \tag{2.25}$$

The kernel functions $C_i \, exp(-i \omega_i t)$ in (2.25) depend on the nature of the eigenvalue spectrum and the spatial projection of the injection onto the modes. The time-dependent coefficients $c_i(t)$, given by (2.25), may be calculated readily given the temporal structure

of the injection $\square_t$. The resulting solution in spectral space must be summed over the vertical basis functions and inverse Fourier transformed to obtain the solution in physical space. The field variables may then be transformed via (2.3) to remove the mass weightings of the basic state.

2.4 Summary

This chapter presents an analytic model for investigation of hydrostatic and geostrophic adjustment. A fully compressible linear model is solved subject to external injection of mass, momentum, or heat. The injection is intended to model the net effect of processes with characteristic scales smaller than those on which the linear model is justifiable. The spatial structure of solutions is described by a set of basis functions satisfying the rigid lower boundary condition. One such structure is the Lamb mode that decays exponentially from the lower boundary. Because the rigid lower boundary condition is of a different form for the vertical velocity and pressure fields, there are two sets of basis functions describing the solution state. Only the pressure and horizontal velocity components contain the Lamb mode.

The time-dependence of each spatial mode is generalized in terms of a temporal Green's function. This function resembles a solution to the homogeneous problem, which is solved as an eigenvalue-eigenvector problem. The eigenvalues correspond to steady, acoustic-wave, and buoyancy-wave classes. The exception is the Lamb mode, which contains only a steady and an acoustic class. When the heating is of finite duration, the

time-dependence of each spatial mode may still be written as a sum of these distinct time-dependencies except that the projections onto each of these classes are time dependent.

Chapter 3

Transient Dynamics

3.1 Experiment Description

The solution presented in the previous chapter consists potentially of a broad spectrum of waves that accomplish a broad range of motions. The response to any given injection is likely to excite preferentially a specific region of this spectrum. We therefore expect the characteristics of the response to depend on the spatial and temporal detail of the injection. The series of experiments in section 3.2 examines this dependence and demonstrates several stages of the adjustment process following a heat injection. We also anticipate the response to depend on the type of injection. Section 3.3 demonstrates the manner by which the response to injections of mass and momentum differ from one another and that of the heat injection of section 3.2.

In section 3.2, we consider the response to an injection of heat of the form

$$\dot{Q} = 2\dot{Q}_0 \left[\frac{1}{1 + \left(\frac{x}{a}\right)^2} \right] H^*(z, d_g, d + d_g) \sin^2\left[\frac{\pi}{d}(z - d_g)\right] H^*(t, 0, \tau) \sin^2\left[\frac{\pi t}{\tau}\right] , \quad (3.1)$$

where a is the heating half-width, d is the heating depth, d_g is the heating elevation, τ is the heating duration, $\dot{Q}_0$ is the heating amplitude, $H^*(x, x_1, x_2) = H(x - x_1) - H(x - x_2)$ is the top-hat function between $x = x_1$ and $x = x_2$ and H is the Heaviside step function . Figure 3.1 presents the spatial structure of this heating. The heating aspect ratio $\varepsilon = O(d / 2a)$ and the duration τ are varied through a range of scales representing individual

clouds to organized convective systems. For each of the experiments, the base state is described by $T_* = 255$ K, $p_* = 1000$ mb, $\rho_* = 1.37$ kg m^{-3}, $N_s = .0194$ s^{-1}, $H_s = 7.48$ km, $c_s = 320$ m s^{-1} , $f = 10^{-4}$ s^{-1}, and the heating amplitude is $\Delta\Theta = 1$ K. The base state temperature is chosen such that the scale height, buoyancy frequency, and sound speed are representative of the middle troposphere. The base state pressure is chosen such that the total column mass is of a typical atmospheric value. In each experiment 512 horizontal modes and 51 vertical modes are used to construct the solutions, and the domain depth is taken to be several scale heights, $2D = 30$ km. A Lanczos smoother (Arfken, 1970) is applied to improve the convergence properties of derivatives of Fourier transformed variables.

A useful quantity for examining the characteristics of the response is the parcel displacement. The time-dependent parcel displacement fields (ξ_x, ξ_z) are found by integrating the *y*-momentum (2.1b) and heat (2.1d) equations in time to yield,

$$\xi_x(t) = -\frac{1}{f}\left[v_\Delta - \int_{t_0<0}^{t} \dot{v}\, dt\right] \quad ,$$
$$\xi_z(t) = -\frac{g}{\rho_s N_s^2}\left[\rho_\Delta - \int_{t_0<0}^{t} \dot{\rho}\, dt\right] \quad . \tag{3.2}$$

Chagnon and Bannon (2001) discuss the salient features of this net displacement field at $t \gg$. The mechanism by which the net upper-level outflow, lower-level inflow, and upward displacement of the heated column is achieved is demonstrated by observing the time-dependent evolution of the displacement fields. In the following three experiments of section 3.2, the size and duration of the heat injection are chosen to represent cumulus-scale, mesoscale, and intermediate-scale injections.

Figure 3.1

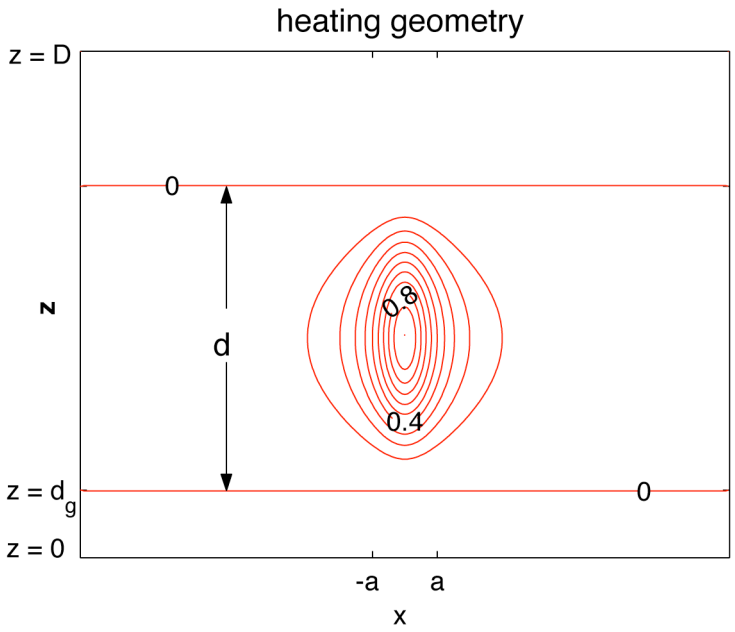

Figure 3.1: Geometry of the heat injection, demonstrating the heating half-width a, the depth d, the elevation d_g, and domain half-depth D. A rigid upper boundary is placed at $z = 2D$.

3.2 Transient Response to Injection of Heat

3.2.1 Cumulus-scale Heating

In the first experiment, we let a = 2 km, d = 5 km, d_g = 1 km, and τ 0 such that the heating is impulsive (i.e. Dirac delta function in time) with aspect ratio of unity. Although the instantaneous heating is not physical, the solution is informative because it represents the temporal Green's function solution $\widehat{\Phi}$ but it overemphasizes the response by the highest frequency waves. The characteristics of such an injection are most representative of a small isolated convective cloud.

Figure 3.2 presents the time-dependent displacement field in the first minute following the heat injection. The initial adjustment is dominated by acoustic waves generated in the regions of heating gradient. The displacements occur in the direction of energy propagation and accomplish a net expansion of the heated region. The portion of the acoustic signal that propagates horizontally with maximum along the lower boundary is the Lamb wave.

Figure 3.3 presents temporal cross sections of the pressure field. During the acoustic stage, the initial pressure perturbation of 307 Pa is drastically reduced in amplitude. Two distinct vertically propagating wave fronts are evident in Fig. 3.3a emanating from the upper and lower halves of the heated region. The leading edge of each front is a large high pressure perturbation, followed by a region of smaller amplitude

negative perturbation. The approach of the upward propagating high (low) pressure perturbation is associated with upward (downward) acceleration. The downward propagating wave front is reflected off the lower boundary. The vertical profile of pressure perturbation remaining after these waves have left the heated region differs qualitatively from the steady state of Bannon (1995) in that a low pressure perturbation exists below the heated region and is not strictly hydrostatically balanced. Figure 3.3b demonstrates the horizontal propagation of the acoustic signal along the lower boundary (i.e. the Lamb wave). Because the heating is elevated, the signal appears along the lower boundary a few seconds following the heating. The wide signal that first appears on the lower boundary consists of some vertically propagating acoustic waves. After these waves have reflected off the lower boundary, the primary signal is the Lamb wave. In this two-dimensional problem, the acoustic wave signal decays as $t^{-1/2}$ (Lighthill 1978, section 1.4). However, the Lamb wave signal is essentially one-dimensional and therefore must not exhibit any decay in order for its energy to be conserved. The one-dimensional Lamb wave front consists of a large, narrow positive perturbation, whereas the two-dimensional acoustic wave fronts consist of the leading positive perturbation and trailing negative perturbation (Lighthill 1978, Fig. 20). The negative perturbation trailing the Lamb wave in Fig. 3.3 is mainly due to a loss of mass in the heated column at the onset of the upper level outflow and the buoyancy adjustment.

Figure 3.4 presents the time-dependent displacement field in the first twelve minutes following the heat injection. This stage of adjustment is dominated by the emergence of nonhydrostatic buoyancy waves. In the first minutes, these waves accomplish a net upward displacement of the heated layer accompanied by a pattern of

inflow/outflow. This initial circulation is evident at the end of the acoustic stage (see Fig. 3.2e,f). By the sixth minute an upper level pattern of inflow is established and sinking takes place in the core of the heated column, and the circulation that initially developed on the periphery of the heated region is propagating away from the heated column. The interaction of the downward propagating waves with the lower boundary results in localized circulation patterns confined to the lower boundary.

Figure 3.2

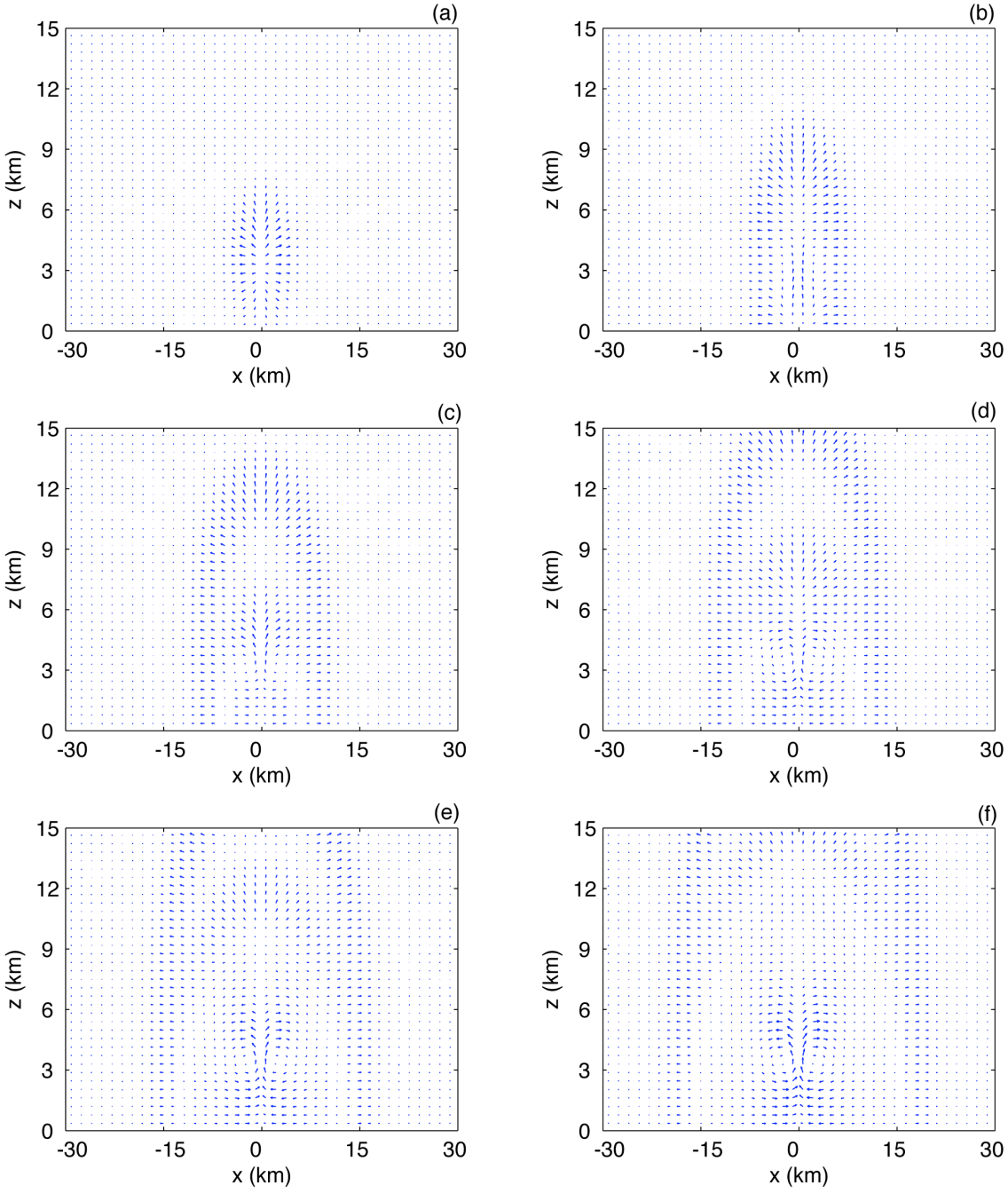

Figure 3.2: Time-dependent displacement fields calculated over ten second intervals ending (a) 10 (b) 20 (c) 30 (d) 40 (e) 50 and (f) 60 seconds following an impulsive heat injection. When the heating amplitude is 1 K, a head-to-tail length vector is 3.1 m (5.1 m) in the *x*- (*z*-) direction.

Figure 3.3

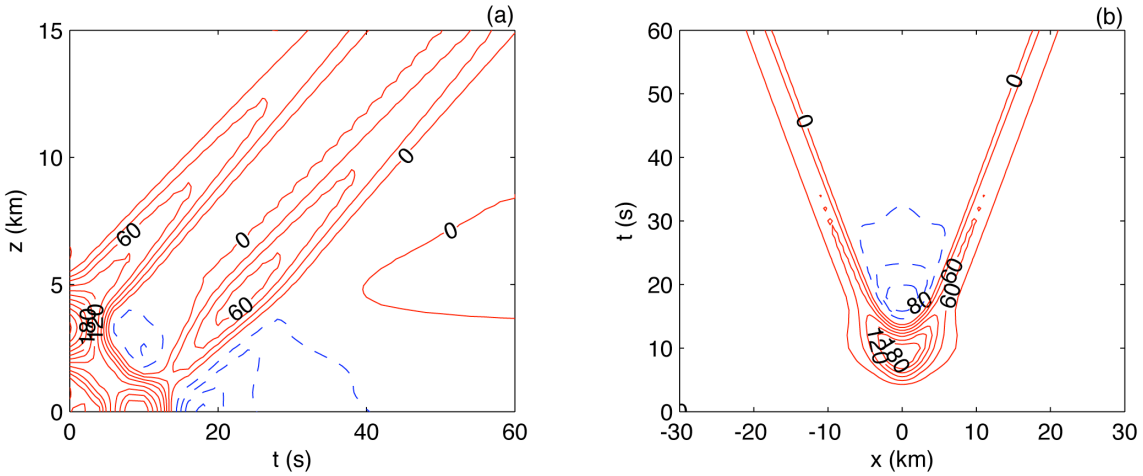

Figure 3.3: Temporal cross section of the pressure field at (a) $x = 0$ as a function of height z and time t and (b) at $z = 0$ as a function of distance x and time t following an impulsive heat injection. The heating depth and elevation are $d = 5$ km and $d_g = 1$ km with the peak heating occurring at $z = 3.5$ km. The contour interval is 20 Pa for $|p| < 60$ Pa and 30 Pa otherwise. Here and elsewhere, negative contours are dashed.

Figure 3.4

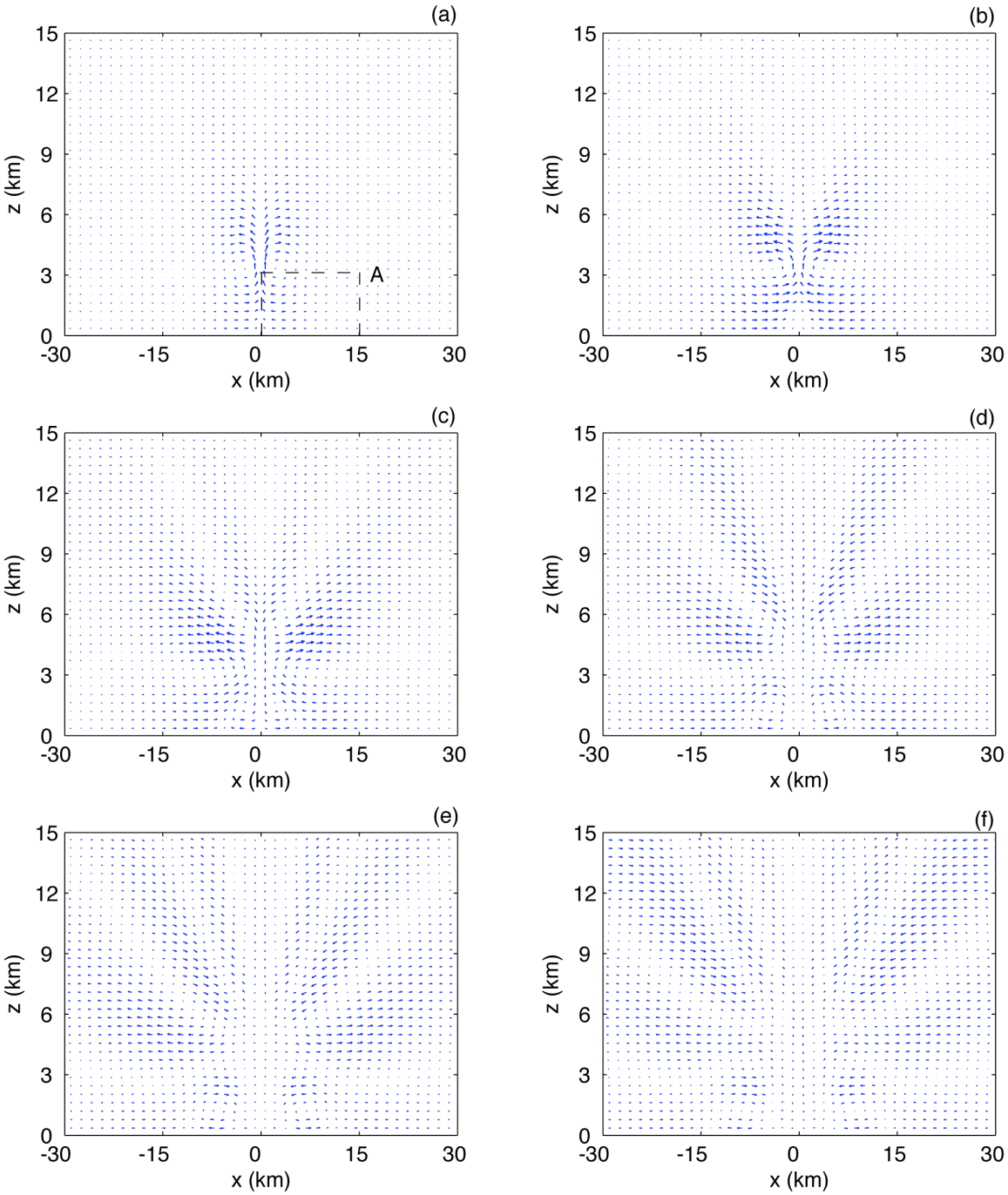

Figure 3.4: Time-dependent displacement fields calculated over two minute intervals ending (a) 2 (b) 4 (c) 6 (d) 8 (e) 10 and (f) 12 minutes following an impulsive heat injection. When the heating amplitude is 1 K, a head-to-tail length vector is 46.9 m (52.2 m) in the x- (z-) direction.

Figure 3.5 presents a refined view of these lower boundary rotors as they propagate through the region marked ‘A’ in Fig. 3.4 during the sixth to twelfth minutes. The outflow associated with these rotors is approximately 4 km wide, 1 km deep, and propagates at a horizontal speed of approximately 15 m/s. The rotors displace the location of maximum horizontal convergence away from the heated core and elevate the inflow region.

Figure 3.6 presents cross sections of the potential temperature field during the nonhydrostatic buoyancy stage. Integration of the heat equation (2.1d) with respect to time demonstrates that the potential temperature perturbation depends on the time-integrated heating as well as the time-integrated advection of the base state potential temperature. The time-integrated vertical advection is proportional to the net vertical displacement. Because the acoustic and Lamb waves do not produce very large vertical displacements wheras the buoyancy waves do produce large vertical displacements, the potential temperature perturbation effectively isolates the buoyancy waves. During the buoyancy stage, the amplitude of the initial potential temperature perturbation is drastically reduced. The shortest buoyancy period is $\tau_b = 2\pi/N_s \approx 324$ s, which corresponds to a wave with zero horizontal group velocity (i.e. Fig. 2.2 indicates that as the wave aspect m/k approaches zero, the slope of the dispersion curve in the buoyancy class approaches zero and the frequency approaches N_s). This oscillation is evident in Fig. 3.6a. After a period τ_b following the heat injection, the potential temperature perturbation is reduced by approximately 80%. Figure 3.6b demonstrates the continued emergence of several wave fronts from the heated region during the nonhydrostatic buoyancy stage.

The waves slowest to emerge from the heated region are of increasing vertical wavenumber (see Fig.3.4).

The distinction between the acoustic and buoyancy stages of adjustment is emphasized by examining vertical profiles (Fig. 3.7) of parcel trajectories on the periphery of the heated regions. During the acoustic stage, air parcels are displaced outward from the heated region. Aloft, the magnitude of the displacements is a decreasing function of height. During the buoyancy stage, the displacements are an order of magnitude larger and exhibit more detail than during the acoustic stage. Initially, air parcels located below the level of mid-heating are drawn toward the heated column while those located above are pushed outward. Sinking occurs at all levels below the top of the heating. This is the signal associated with the lowest vertical wavenumber modes that are in phase with the heating, described by Bretherton and Smolarkiewicz (1989). The lower boundary constrains the ability of air parcels to accelerate downward in the vicinity the boundary. Following the initial subsidence the air parcels accelerate upward toward their initial position, which they overshoot, and are subsequently accelerated downward. While this vertical oscillation occurs, air parcels located slightly above (below) the level of mid-heating continue moving outward (inward) horizontally. In the vicinity of the lower boundary, air parcels that initially are drawn inward are accelerated outward by the lower boundary rotors demonstrated in Fig. 3.5. Aloft, air parcels oscillate both vertically and horizontally about their initial position with amplitude decreasing with increasing height.

Figure 3.5

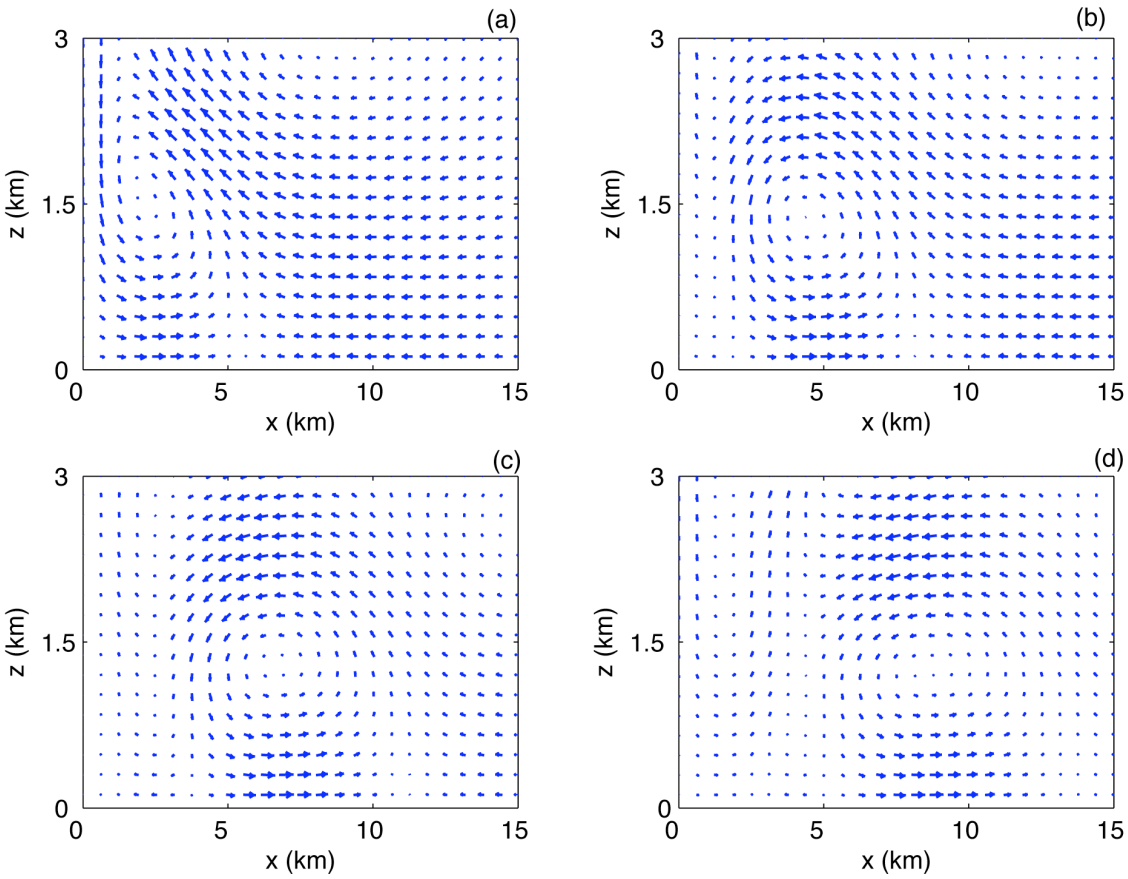

Figure 3.5: Refined view of region A in Fig.6a containing the outwardly propagating boundary rotor at times (a) 6 (b) 8 (c) 10 and (d) 12 minutes following an impulsive heating. A head-to-tail length vector is 23.5 m (26.1 m) in the x- (z-) direction.

Figure 3.6

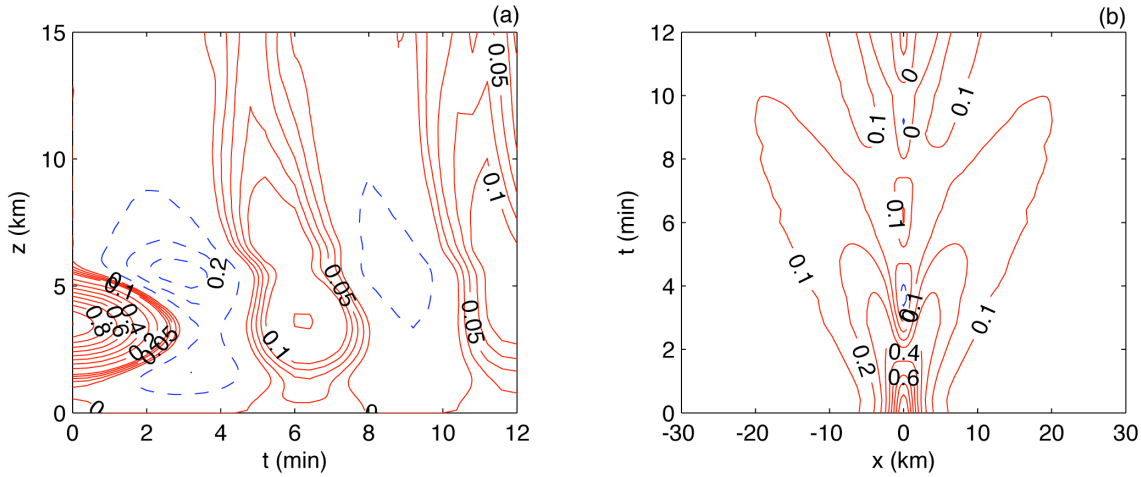

Figure 3.6: Temporal cross section of the potential temperature field at (a) $x = 0$ as a function of height z and time t and (b) at the level of mid-heating $z = 3.5$ km as a function of distance x and time t following an impulsive heat injection. The contour interval is .025 K for $|\Pi| < .1$ K Pa and .1 K otherwise.

Figure 3.7

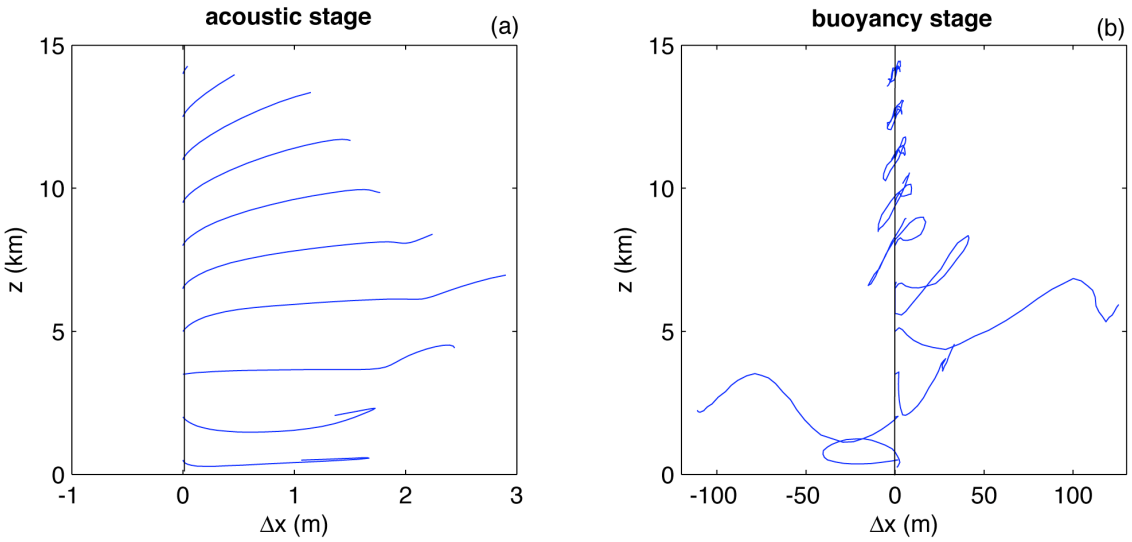

Figure 3.7: Trajectories of parcels during (a) the first thirty seconds and (b) the first twelve minutes at heights between z = .5 km and z = 11 km and at a horizontal distance of 5 km east of the center of an impulsive heat injection of half-width a = 2 km, depth d = 5 km, elevation d_g = 1 km, and amplitude □□= 1 K.

3.2.2 Intermediate-scale Heating

In the second experiment, we let a = 25 km, d = 9 km, d_g = 1 km, and τ = 20 min such that the aspect ratio is 0.1. Although the heating duration is much longer than an acoustic wave period, an acoustic adjustment is still very discernible in this experiment, as will be demonstrated. Such an injection models a large convective storm. The maximum pressure perturbation of 27 Pa is much smaller than that generated by the impulsive heating (307 Pa).

Figure 3.8 presents time-dependent displacement vectors computed over ten minute intervals during the first hour following the onset of heating. The displacement field is dominated by the action of buoyancy waves. As in Fig. 3.4, the injection initially displaces the heated column upward and circulating patterns of inflow and outflow emerge on the periphery of the heated column. The lower boundary rotors are again evidenced by the outward and upward displacement of the inflow region established initially beneath the heated core. The more complicated patterns of inflow and outflow that emerged above the heated region in the cumulus scale experiment are still present in this experiment but of smaller magnitude relative to the lowest vertical wavenumber circulation. The aspect ratio of the displacements is approximately 0.1, which implies that the dominant buoyancy waves are weakly nonhydrostatic. Vertical profiles of parcel trajectories along the periphery of the heated region resemble those presented in Fig. 3.7b except for an order of magnitude decrease in the trajectory aspect ratio.

Figure 3.9 presents temporal cross-sections of the potential temperature field, similar to Fig. 3.6. The high frequency buoyancy oscillations present in Fig. 3.6a are not present in Fig. 3.9a. These oscillations are not generated significantly by such long duration injection. The regions of negative perturbation that emerge both above and below the heated layer indicate upward vertical displacement (i.e. the advection of lower base state values of potential temperature). This vertical advection limits the maximum amplitude of the potential temperature perturbation to ~.55 K. Within twenty minutes of the cessation of heat injection, these anomalies are removed by the propagation of buoyancy waves. Figure 3.9b demonstrates the emergence of the waves from a location in the middle of the heated layer. The dispersive nature of the waves leads to a decay in the amplitude of these signals of more than 80% after they have propagated 200 km away from the heated region. Once again, the hydrostatic and geostrophic steady state towards which this atmosphere adjusts is approximately trivial (i.e. the perturbations in the asymptotic steady state are negligible compared to the initial and transient perturbations).

Figure 3.10a demonstrates the evolution of the vertical profile of pressure at $x = 0$ during the injection of heat. Vertically propagating acoustic waves are not evident as they were in Fig.3.3a. Rather, a deep region of positive pressure perturbation emerges smoothly above and throughout most of the heated region. The positive perturbation is mainly a hydrostatic contribution from the net upward expansion of the column. The negative perturbation along the lower boundary indicates the loss of mass from the column due to upper level outflow. Compressibility effects may also influence the pressure perturbation by encouraging a pressure increase/decrease in regions of convergence/divergence. Figure 3.10b demonstrates the evolution of the horizontal

profile of pressure along the lower boundary. Although the displacement field is dominated by buoyancy wave motions and the heating duration is longer than the acoustic wave period, a clearly discernible Lamb wave signal emerges from the heated layer and propagates horizontally. Unlike that in Fig. 3.3b, the amplitude of the Lamb wave signal increases in time. This amplification is the result of the accumulation of continuously generated Lamb waves during the application of the finite-duration heating.

Figure 3.8

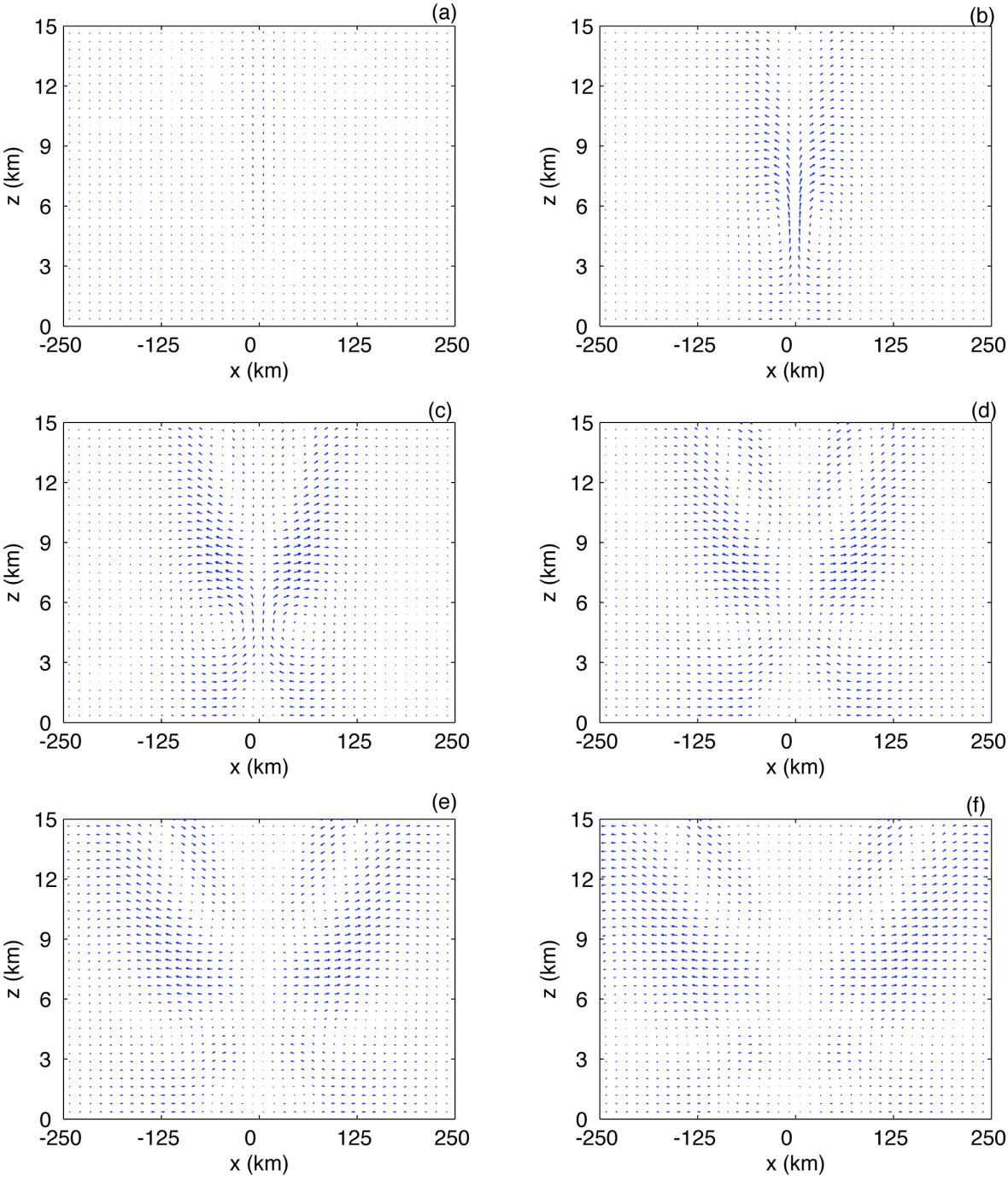

Figure 3.8: Time-dependent displacement fields calculated over ten minute intervals ending (a) 10 (b) 20 (c) 30 (d) 40 (e) 50 and (f) 60 minutes following a heat injection of duration 20 minutes. When the heating amplitude is 1 K, a head-to-tail length vector is 312 m (39.7 m) in the *x*- (*z*-) direction.

Figure 3.9

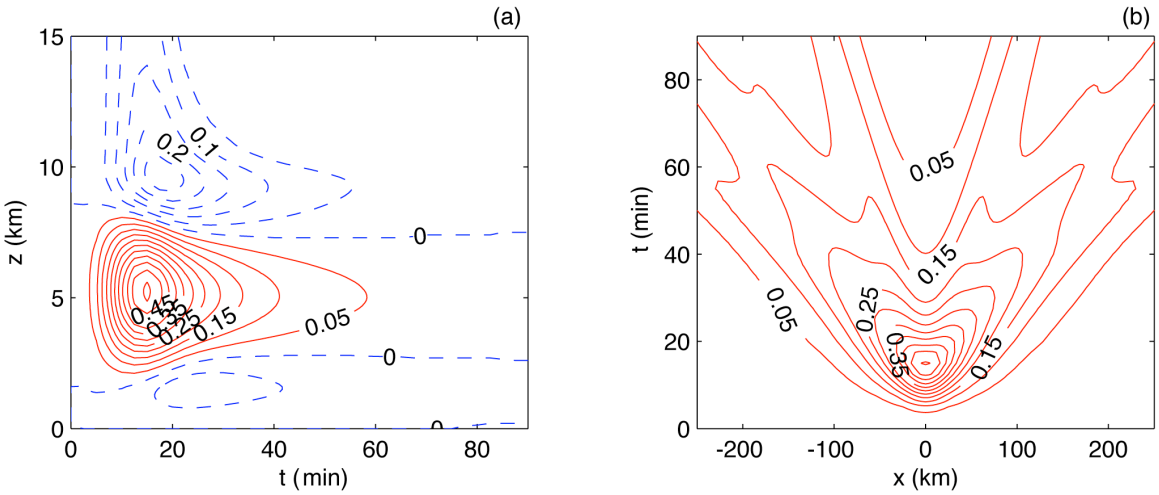

Figure 3.9: Temporal cross section of the potential temperature field at (a) $x = 0$ as a function of height z and time t and (b) at the level of mid-heating $z = 5.5$ km as a function of distance x and time t following a heat injection of duration 20 minutes. The contour interval is .05 K.

Figure 3.10

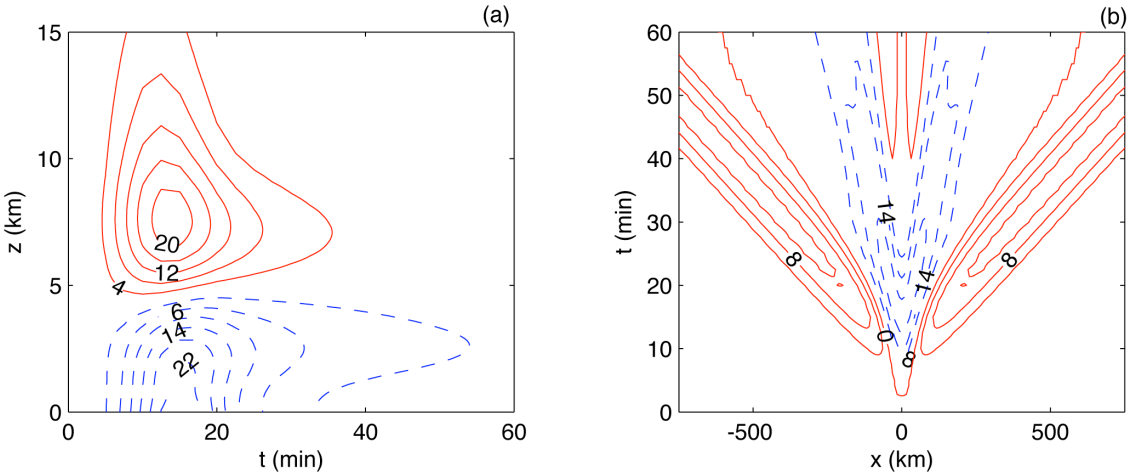

Figure 3.10: Temporal cross section of the pressure field at (a) $x = 0$ as a function of height z and time t and (b) at $z = 0$ as a function of distance x and time t following a heat injection of duration 20 minutes. The contour interval is (a) 4 Pa and (b) 4 Pa for $|p| < 12$ Pa and 8 Pa otherwise.

3.2.3 **Mesoscale Heating**

In the third experiment, we let a = 100 km, d = 9 km, d_g = 1 km, and τ = 2 hours such that the aspect ratio is 0.01. Here the heating duration is longer than a typical nonhydrostatic buoyancy wave period. Such an injection is intended to model a large organized mesoscale convective system. While the individual convective elements that comprise such a system are likely to excite a wave response similar to those presented above, a response to the conglomerate system by the larger synoptic-scale environment is likely to involve hydrostatic, rotating buoyancy waves, and a nontrivial hydrostatic and geostrophic steady state.

The time-dependent displacement vectors are omitted for this experiment because they resemble qualitatively those in Fig. 3.8 except on longer time and larger horizontal spatial scales with maximum horizontal and vertical displacements $\Delta x = O$(1 km) and $\Delta z = O$(10 m). The aspect ratio of these displacements is approximately 0.01 and the time scale of the transients is an order of magnitude longer than the maximum buoyancy wave period. These two conditions imply that the transients are approximately hydrostatic. The adjustment to the conglomerate system is therefore accomplished primarily by hydrostatic buoyancy waves.

Figure 3.11 presents temporal cross-sections of the potential temperature field, similar to Figs. 3.6 and 3.9. Unlike the previous two experiments, the potential temperature perturbation adjusts toward a nontrivial geostrophic and hydrostatic state. After approximately six hours the perturbation at $z = 0$ is comprised of this steady state

and inertia-gravity waves. The steady state qualitatively resembles the solutions presented in Chagnon and Bannon (2001). The lowest frequency waves form an inertial oscillation of maximum period $2\pi/f \approx 17.4$ hours.

In spite of the long duration and large horizontal scale of this injection, a Lamb wave signal is again discernible. Figure 3.12 presents temporal cross-sections of the pressure perturbation in the first four hours following the onset of heat injection. The magnitude of the Lamb signal is similar to that in the previous experiment. The primary difference is in the width of the signal, which is determined by the duration and width of the injection. The sharpness of the leading and trailing edges of the Lamb signal is determined by the time scale associated with the start-up and shut-off of the heat injection (3.1). To illustrate this, we replace the temporally smooth sine-squared heating in (3.1) with one that is a top-hat in time (of identical time-integrated amplitude). Figure 3.13 presents the temporal cross-sections of pressure following this "sharper" heat injection. The leading and trailing edges of the Lamb wave signal in Fig. 3.13b are indeed more abrupt than those generated by the sine-squared injection (see Fig. 3.12b). Figure 3.13a demonstrates that the sudden shut-off produces a rapid decrease in the amplitude of the profile at $z = 0$ at $t = 2$ hours. This indicates an acoustic adjustment accomplished by the Lamb waves and is an example of the presence of multiple time scales associated with the higher order derivatives of the injection.

Figure 3.11

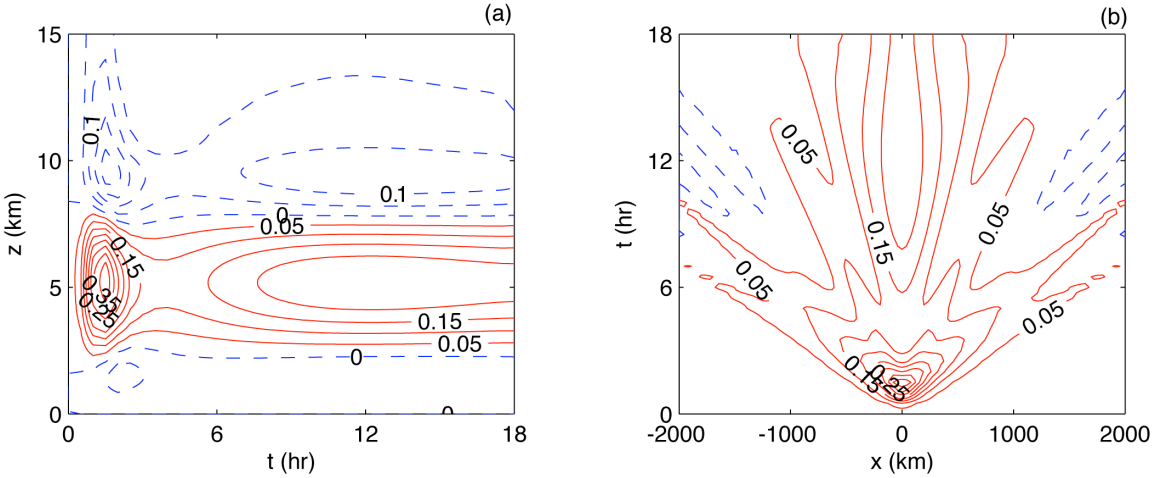

Figure 3.11: Temporal cross section of the potential temperature field at (a) $x = 0$ as a function of height z and time t and (b) at the level of mid-heating $z = 5.5$ km as a function of distance x and time t following a heat injection of duration 2 hours. The contour interval is .05 K.

Figure 3.12

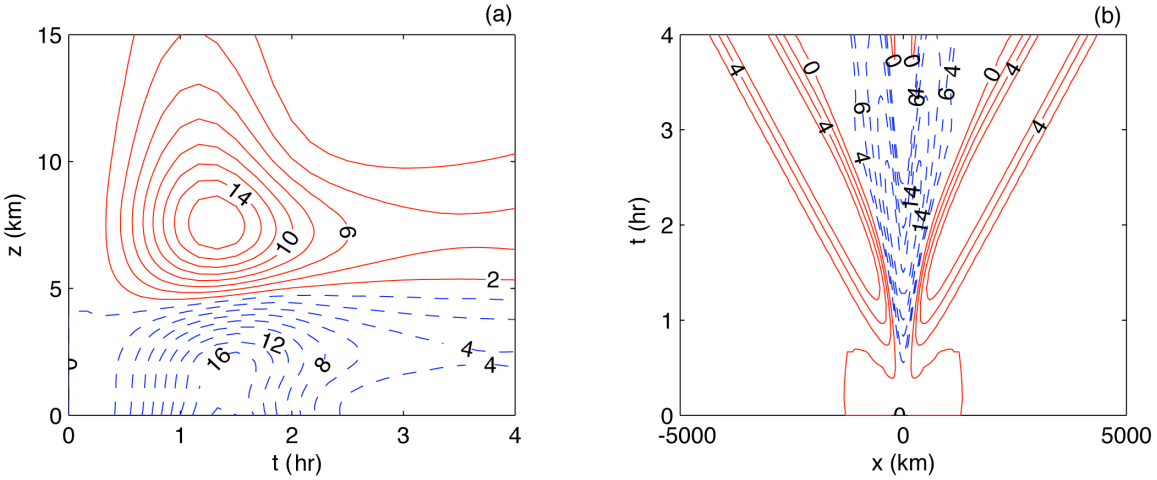

Figure 3.12: Temporal cross section of the pressure field at (a) $x = 0$ as a function of height z and time t and (b) at $z = 0$ as a function of distance x and time t following a heat injection of duration 2 hours. The contour interval is (a) 2 Pa and (b) 2 Pa for $|p| < 12$ Pa and 4 Pa otherwise.

Figure 3.13

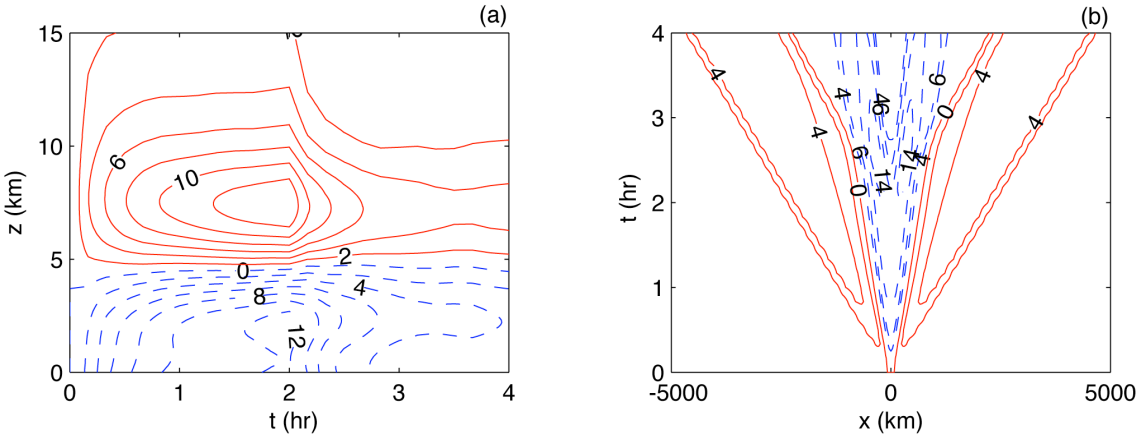

Figure 3.13: As in Fig. 3.12, except following a top-hat injection of heat.

3.3 Transient Response to Injection of Mass and Momentum

The preceding section explored the dependence of the adjustment process on the spatial and temporal details of a heat injection. This section examines how the type of injection affects the characteristics of the adjustment. As in the case of heating, the response to injection of mass and momentum involves acoustic-wave, Lamb-wave, nonhydrostatic buoyancy-wave, and hydrostatic buoyancy-wave regimes. The fundamental characteristics of these regimes are demonstrated in 3.2. The ability of the various types of injection to excite these regimes is examined here.

3.3.1 Injection of Mass

Let us consider the response to an injection of mass of the form

$$\rho = \rho_0 \left[\left(\frac{2 H_s}{d}\right)\sin(z)\cos(z) + \left(\frac{}{}+1\right)\cos^2(z)\right] H^*(z, d_g, d_g + d) \left[\frac{1}{1 + \left(\frac{x}{a}\right)^2}\right]\left[\frac{H^*(t, 0,)}{}\right]\sin^2\left[\frac{t}{}\right] \quad . \tag{3.3}$$

The geometry of (3.3) (Fig. 3.14) is a vertical source/sink dipole representing the transport of mass from lower levels to higher levels accomplished by a convecting cloud. The mass injection (3.3) conserves the total mass and generates a potential vorticity anomaly identical to that of the heating (3.1). The significance of potential-vorticity-equivalent injections is examined in detail in section 4.5.

Figure 3.14

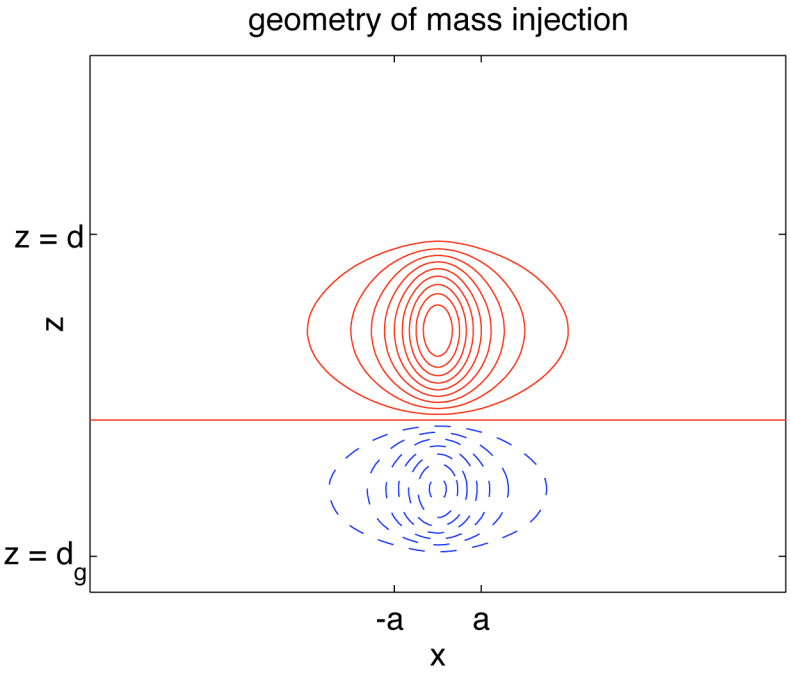

Figure 3.14: The geometry of the mass source/sink dipole (3.3).

The only significant observable difference between the response to this mass injection and the heat injection (3.1) occurs during the acoustic regime. Figure 3.15 presents the acoustic response following an impulsive mass injection (compare to Fig. 3.3) whose amplitude $\square\square$ = 2.36 g/m^3 which corresponds to a heating of amplitude $\square\square$ = .1 K (one-tenth of that in section 2). The acoustic response to the mass injection differs from the heat injection both quantitatively and qualitatively. The maximum pressure perturbation in Fig. 3.15 is 465 Pa, which is larger than that generated by a heating of amplitude $\square\square$ = .1 K in section 2. The magnitude of the pressure perturbation following the mass injection is therefore an order of magnitude larger than that of the equivalent heat injection. Such an extraordinary perturbation suggests that an instantaneous mass injection on this scale is severely unphysical. For example, a mass injection representing the vertical redistribution within a convecting cloud should have a time scale characteristic of the advection by the updraft. The instantaneous mass injection is therefore a severe approximation of this process. Four distinct wave fronts emerge from the perturbed region, rather than the two observed in Fig. 3.3. Expansion occurs in the upper source region while contraction occurs in the lower sink region, each of which generates both upward and downward propagating wave fronts. The contraction in the lower sink region initially generates a negative pressure perturbation on the lower boundary (see Fig.3.15b). A larger positive perturbation next emerges on the lower boundary as the downward propagating front originating from the source region reflects off the boundary. The subsequent buoyancy-wave response is qualitatively indistinguishable from that following the equivalent heat injection presented in section 2.

Figure 3.15

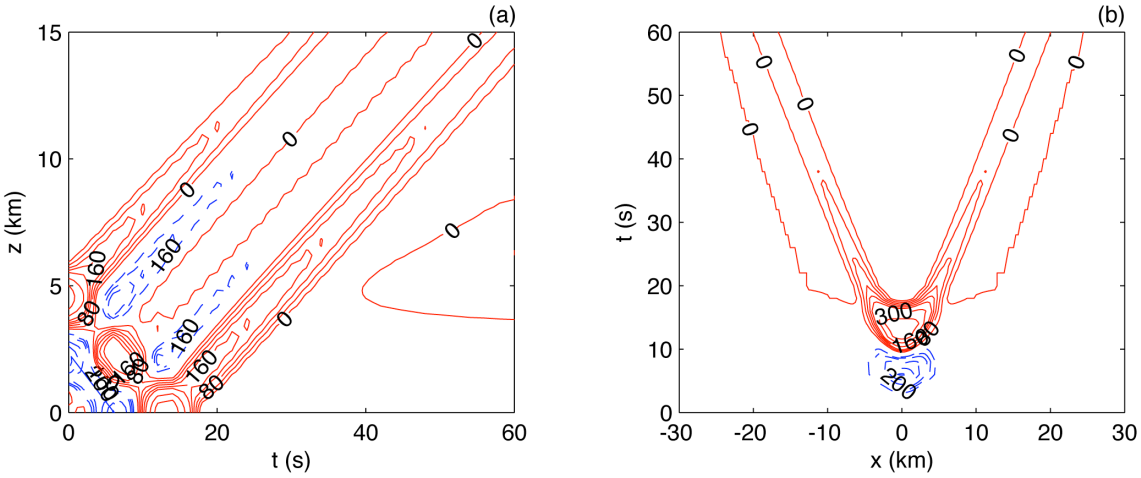

Figure 3.15: Temporal cross section of the pressure field at (a) $x = 0$ as a function of height z and time t and (b) at $z = 0$ as a function of distance x and time t following an impulsive mass injection. The contour interval is 40 Pa for |p'| < 200 Pa and 100 Pa thereafter.

3.3.2 Injection of x-momentum and z-momentum

Next we compare injection of x-momentum and z-momentum with geometry identical to the heating (3.1) with velocity amplitude 1 m/s . This pair of injections makes for an interesting comparison because neither is capable of generating a steady state under the assumption of homogeneity in the y-direction (see section 4.2). The difference between these injections therefore highlights many differences between adjustment in the vertical and horizontal directions.

The differences during the acoustic adjustment are demonstrated by comparing the evolution of the pressure field following impulsive injections of depth d = 5 km and half-width a = 2 km. The acoustic response to the injection of x-momentum (Fig. 3.16) is dominated by a positive (negative) eastward (westward) propagating Lamb wave. The convergence (divergence) induced upstream (downstream) of the x-momentum injection initially generates an elevated positive (negative) pressure perturbation. The subsequent increase (decrease) in the total column mass is accompanied by a positive (negative) perturbation along the lower boundary that propagates away horizontally as the Lamb wave of approximate amplitude 50 Pa. On the other hand, the response to the injection of z-momentum (Fig. 3.17) is dominated by vertically propagating acoustic waves. The amplitude of the fronts is similar to those generated by the injection of x-momentum. Once again, the waves originate from the regions of convergence and divergence. The imposed updraft initially generates a large positive (negative) pressure perturbation in the region of upper- (lower-) level convergence (divergence).

The differences in the buoyancy adjustment are demonstrated by comparing the evolution of the potential temperature field following impulsive injections of depth $d = 5$ km and half-width $a = 2$ km. The buoyancy wave response to the injection of x-momentum (Fig. 3.18) is dominated by a horizontal propagation of energy. The phase of these waves is primarily directed vertically because, unlike the acoustic waves, the phase and group velocity of the buoyancy waves are orthogonal. If we recall that the evolution of the potential temperature field depends on the vertical advection of the base state potential temperature, then it follows that the initial positive perturbation in the upper right quadrant and negative perturbation in the lower right quadrant indicate rising and sinking motions, respectively. Without the addition of heat, the perturbations in potential temperature are entirely attributed to advection of the base state. The buoyancy waves originate in the region of vertical divergence (convergence) located upstream (downstream) of the initial current that develops in response to the initial horizontal convergence (divergence). In contrast, the response to the injection of z-momentum (Fig. 3.19) is dominated by upward propagating waves. The phase of such waves is primarily oriented horizontally (e.g. see slope of dispersion curves in Fig.2.2). The waves originate in the initial updraft that induces the initial negative potential temperature perturbation in the updraft core. Because the response to the injection of z-momentum is primarily vertical, increasing the duration of the injection effectively suppresses the transient response, according to section 2.3. Recall that the nonhydrostatic buoyancy waves are of highest frequency and therefore preferentially filtered from the solution. However, the response to the injection of x-momentum is not as severely affected by the injection duration. In fact, the response to an injection of duration twenty minutes with $a = 25$ km

and d = 5 km (Fig. 3.20) is qualitatively similar to that generated by the impulsive injection. Furthermore, the maximum amplitude of the transients following a twenty minute injection of x-momentum are $|\Delta x|$ = 931 m, $|\Delta z|$ = 12.3 m, and $|\Delta\Pi|$ = .26 K, whereas those following the extended injection of z-momentum are considerably smaller, e.g. $|\Delta x|$ = 15 m, $|\Delta z|$ = 1.5 m, and $|\Delta\Pi|$ = .04 K .

Figure 3.16

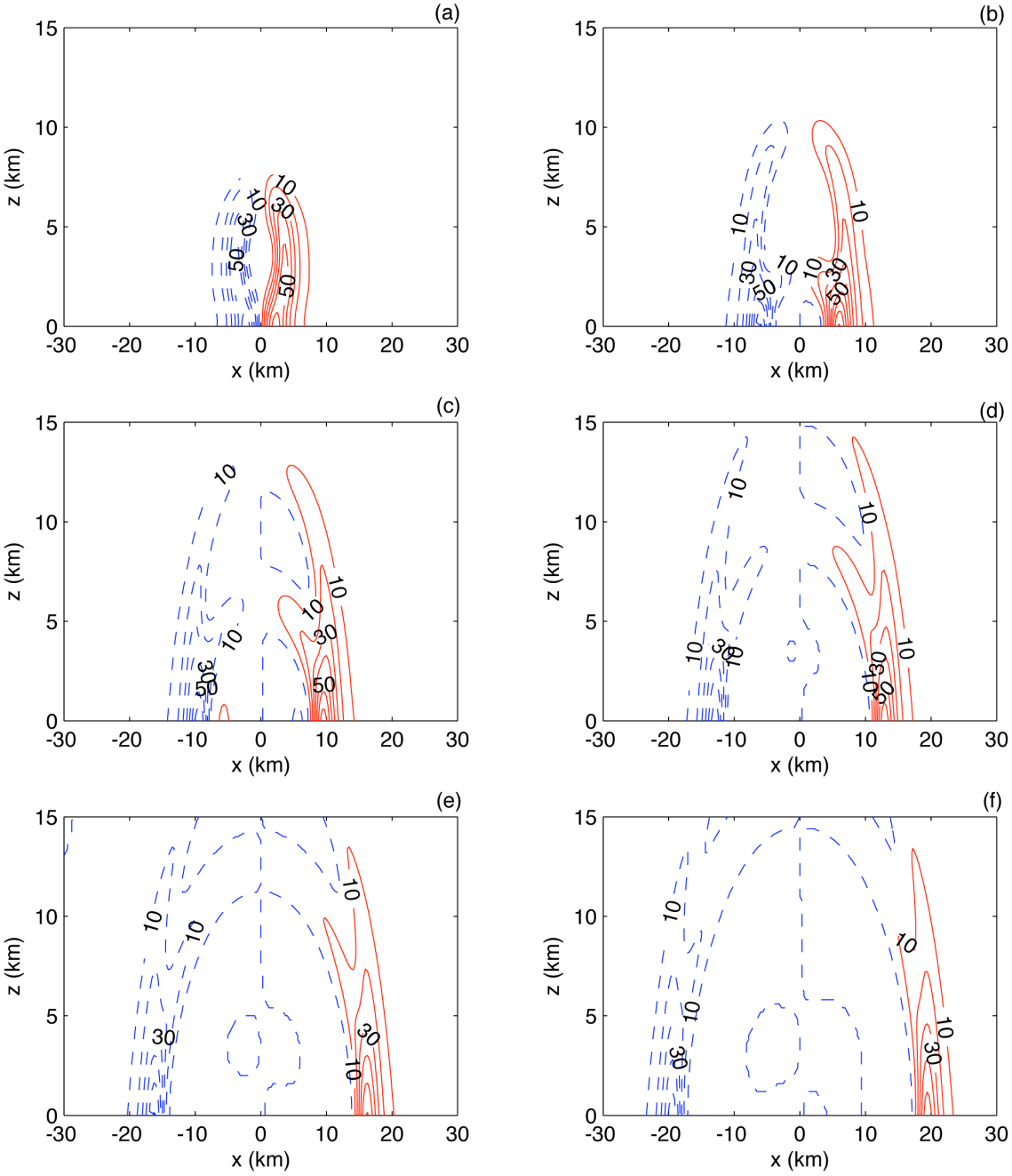

Figure 3.16: Contours of the pressure field at (a) 10 (b) 20 (c) 30 (d) 40 (e) 50 and (f) 60 seconds following an impulsive injection of x-momentum. The contour interval is 10 Pa.

Figure 3.17

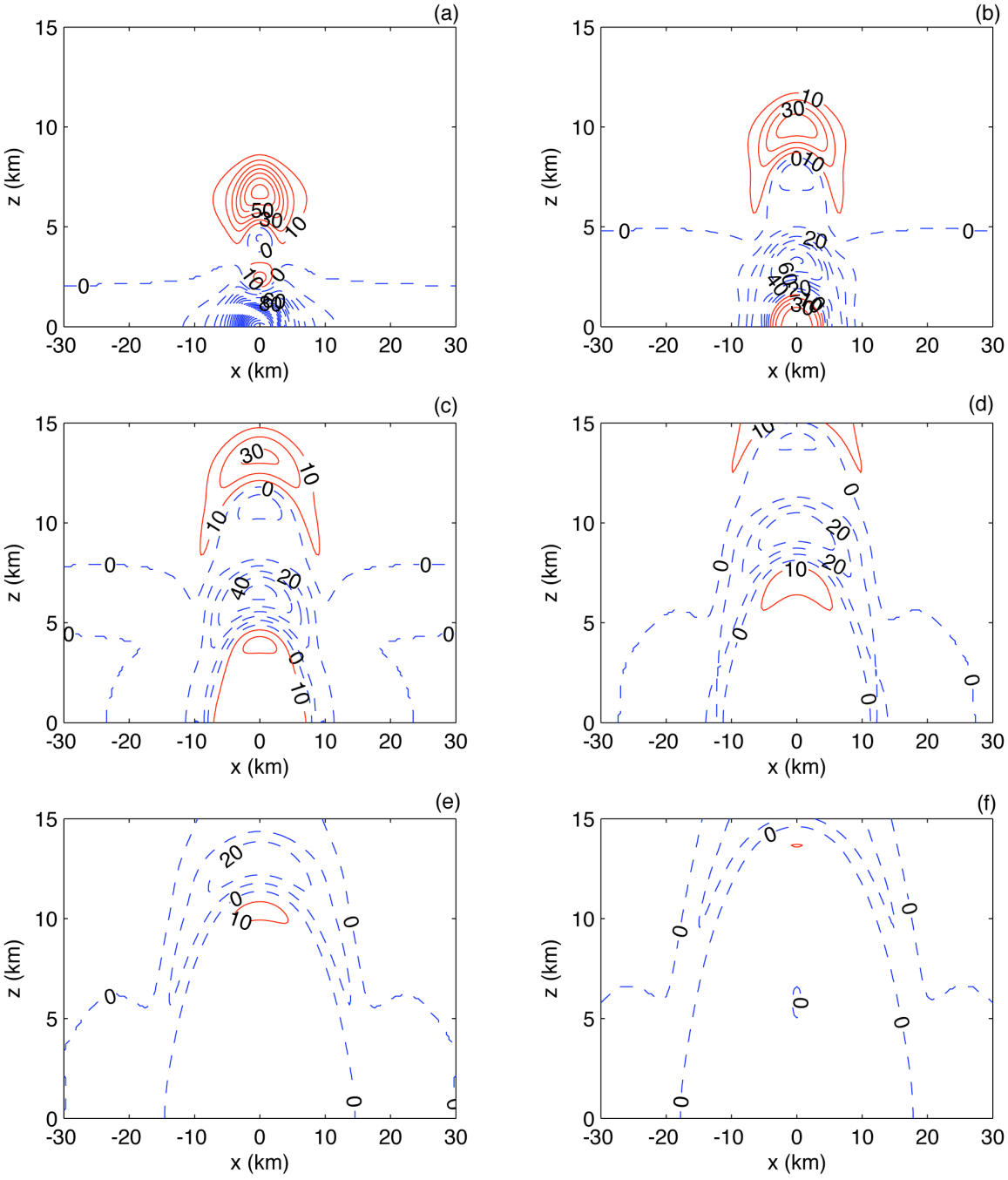

Figure 3.17: Contours of the pressure field at (a) 10 (b) 20 (c) 30 (d) 40 (e) 50 and (f) 60 seconds following an impulsive injection of z-momentum. The contour interval is 10 Pa.

Figure 3.18

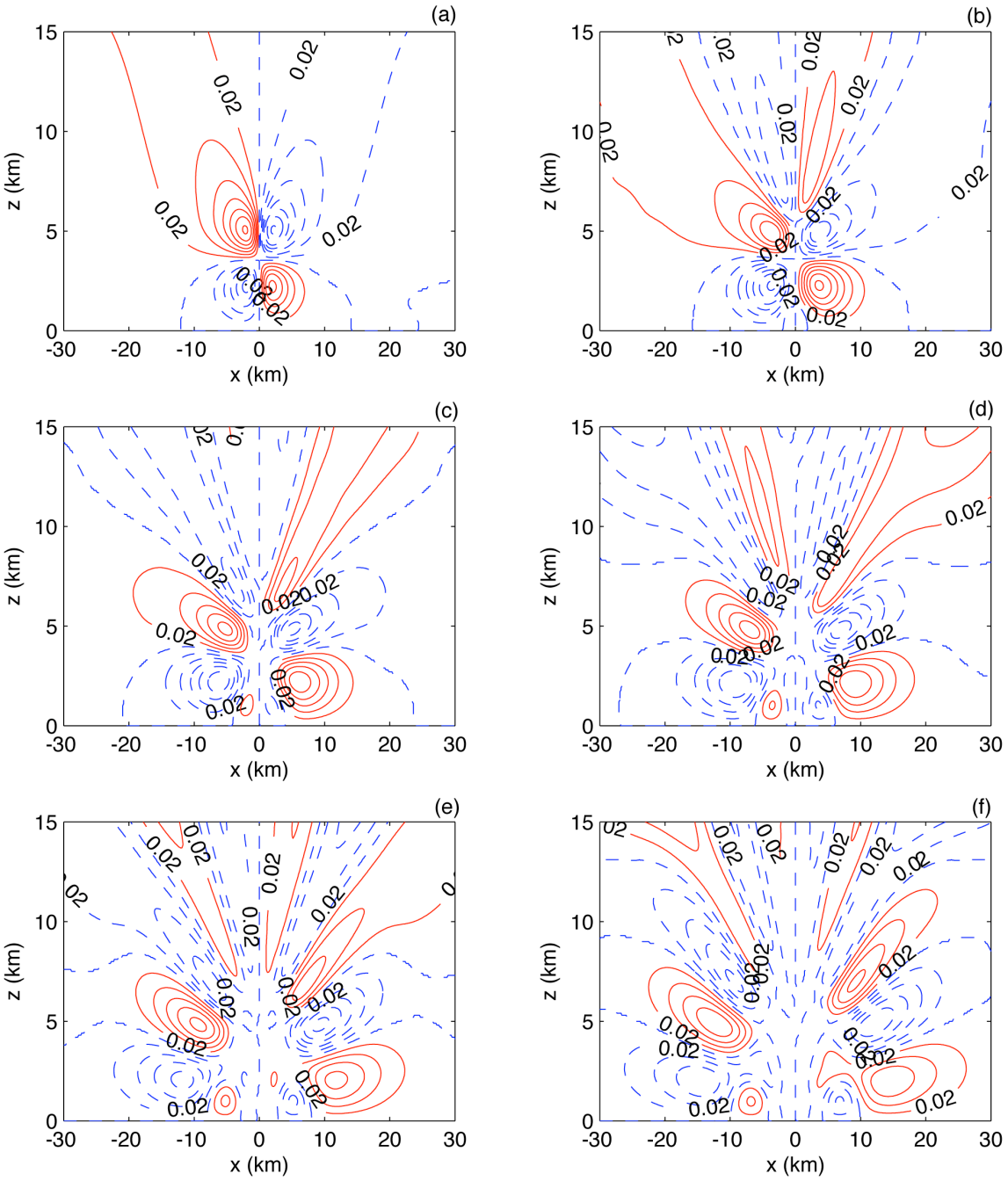

Figure 3.18: Contours of the potential temperature field at (a) 2 (b) 4 (c) 6 (d) 8 (e) 10 and (f) 12 minutes following an impulsive injection of x-momentum. The contour interval is .02 K.

Figure 3.19

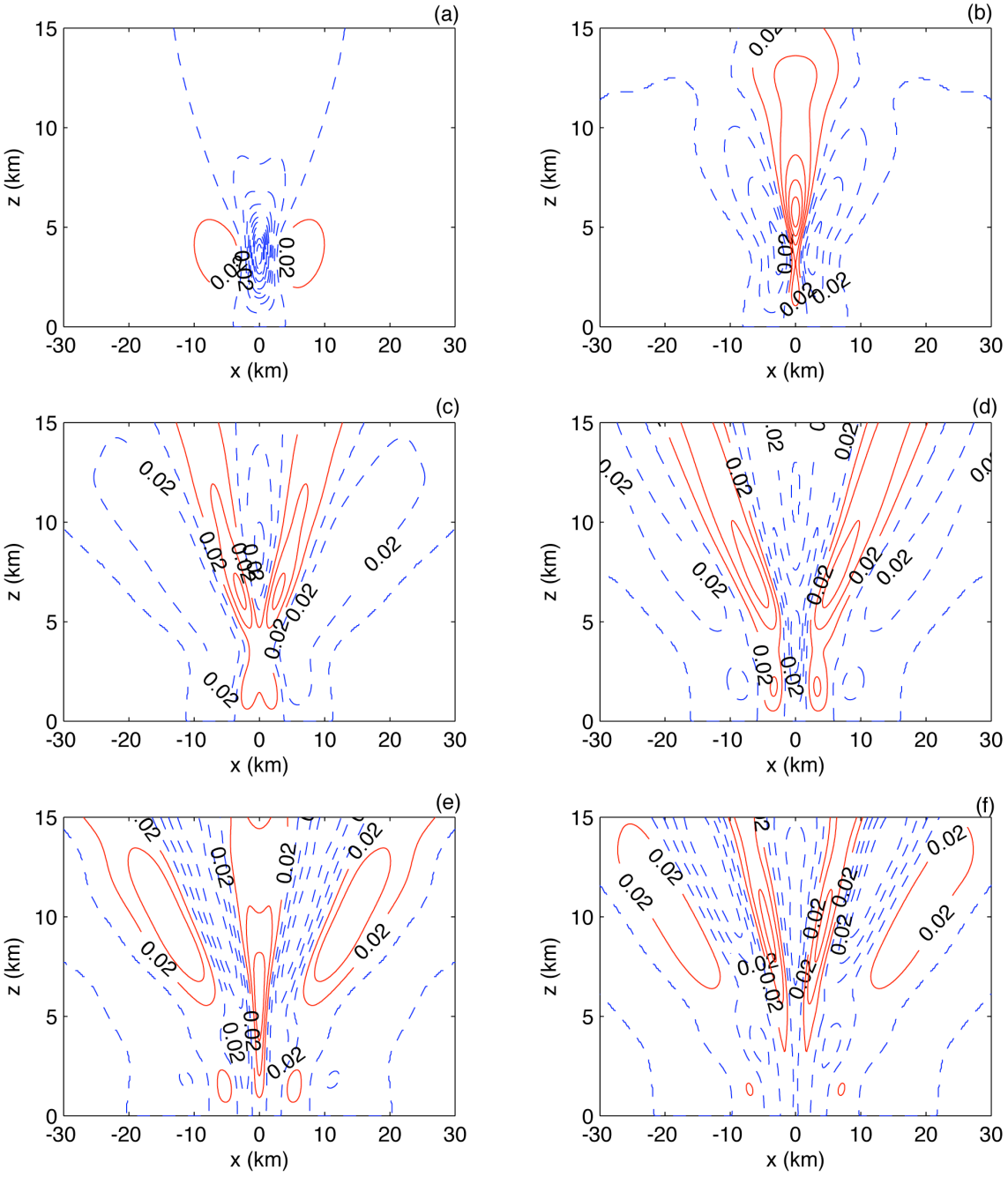

Figure 3.19: Contours of the potential temperature field at (a) 2 (b) 4 (c) 6 (d) 8 (e) 10 and (f) 12 minutes following an impulsive injection of z-momentum. The contour interval is .02 K.

Figure 3.20

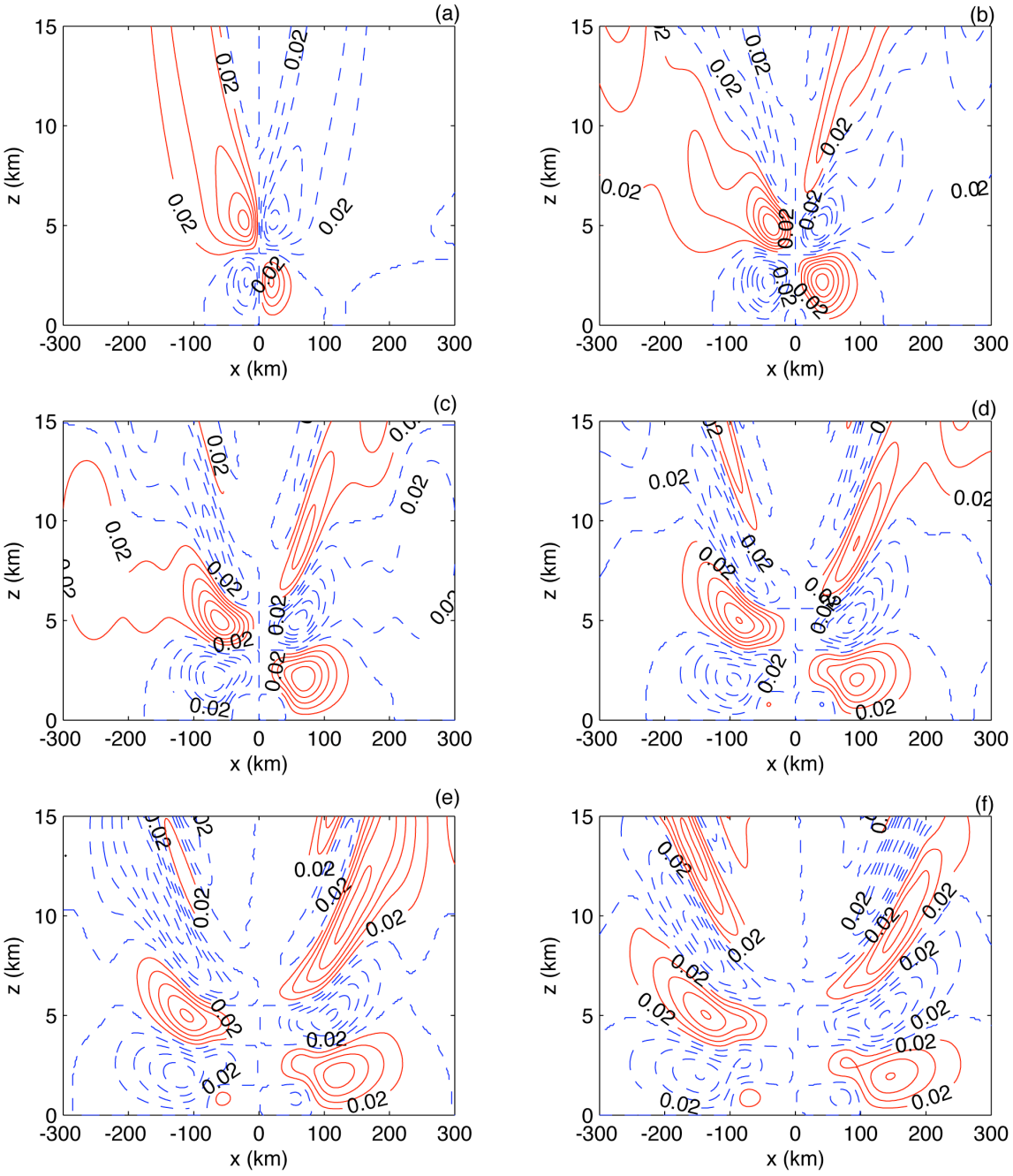

Figure 3.20: Contours of the potential temperature field at (a) 20 (b) 40 (c) 60 (d) 80 (e) 100 and (f) 120 minutes following an injection of x-momentum of duration 20 minutes. The contour interval is .02 K.

3.3.3 Injection of y-momentum

The injection of *y*-momentum induces a response quite different from that induced by the injections of *x*- and *z*-momentum. The assumption of homogeneity in the *y*-direction requires this injection to be nondivergent. The waves examined in section 3.3.2 were primarily generated in regions of convergence and divergence. Following an injection of *y*-momentum, the slow deflection of the current by Coriolis forces produces regions of convergence and divergence. The transient response to an injection of *y*-momentum is therefore expected to involve only the slowest class of waves.

Consider an injection of *y*-momentum with geometry given by (3.1) of depth d = 5 km, elevation d_g = 1 km, half-width a = 25 km, duration τ = 20 minutes, and amplitude 1 m/s. The initial imbalance associated with this injection resembles that of the classic Rossby adjustment problem. Figure 3.21 presents the evolution of the pressure field in the first two hours following the injection. Although the amplitude of the pressure field is only O(1Pa), there is a discernable Lamb wave signal. A temporal cross section of the pressure field along the lower boundary (Fig. 3.22) demonstrates the Lamb wave that induces a far-field change in pressure. By the end of the first hour (Fig. 3.21c), a high (low) pressure perturbation emerges on the right (left) periphery of the current. This localized perturbation indicates the convergence associated with the deflected current. The evolution of the potential temperature field (Fig. 3.23) demonstrates that vertical divergence (convergence) compensates the horizontal convergence (divergence) on the right (left) periphery of the current. Because the width of the current is very small compared to the Rossby radius of deformation $L_R \equiv d N_s / f$ = 970 km, the current itself

undergoes very little change. This dependence is illustrated in Table 3.1 that lists the amplitude of the steady-state current versus the half-width *a*. A wider current induces a steady state of smaller amplitude. Conversely, as the width of the initial current is increased, the amplitude of the transients also increases. This strange behavior is explained in section 4.4.

Figure 3.21

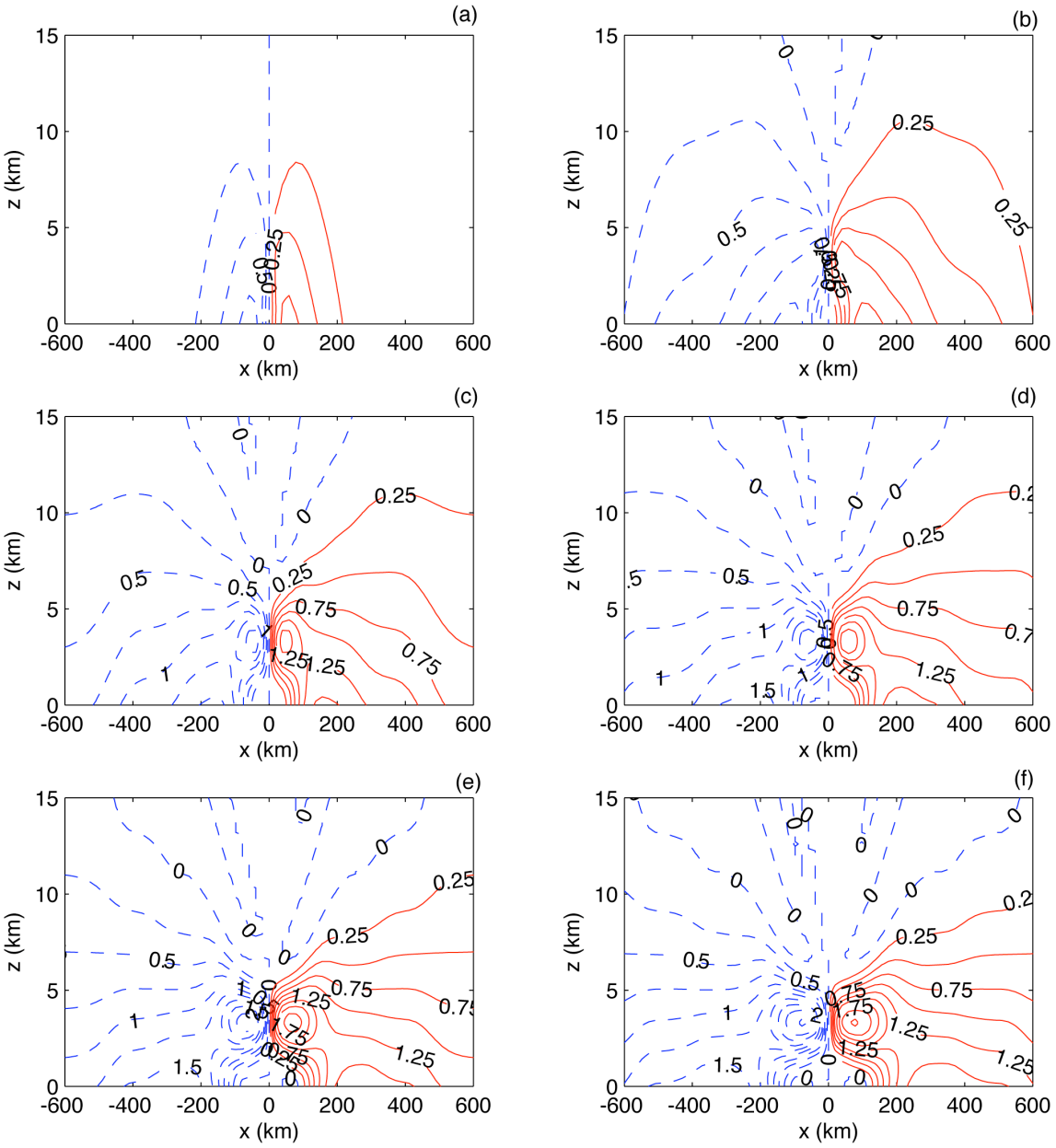

Figure 3.21: Contours of the pressure field at (a) 20 (b) 40 (c) 60 (d) 80 (e) 100 and (f) 120 minutes following an injection of y-momentum of duration 20 minutes. The contour interval is .25 Pa.

Figure 3.22

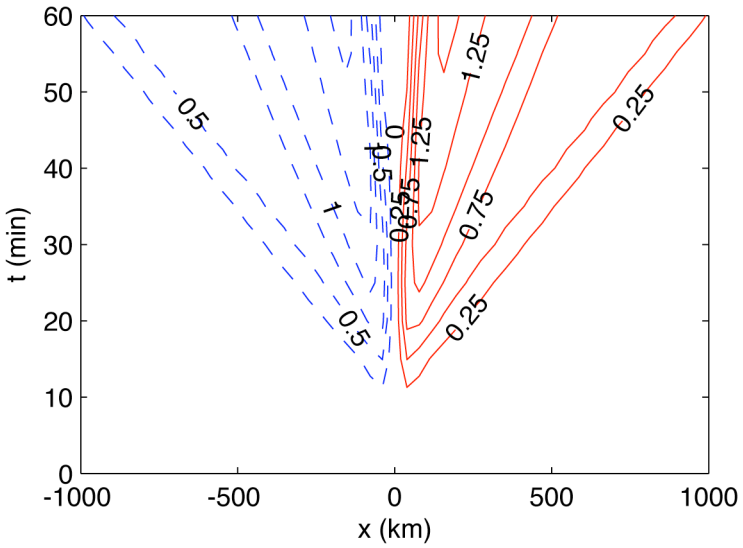

Figure 3.22: Temporal cross section of the pressure field at $z = 0$ as a function of distance x and time t following an injection of y-momentum of duration 20 minutes. The contour interval is .25 Pa.

Figure 3.23

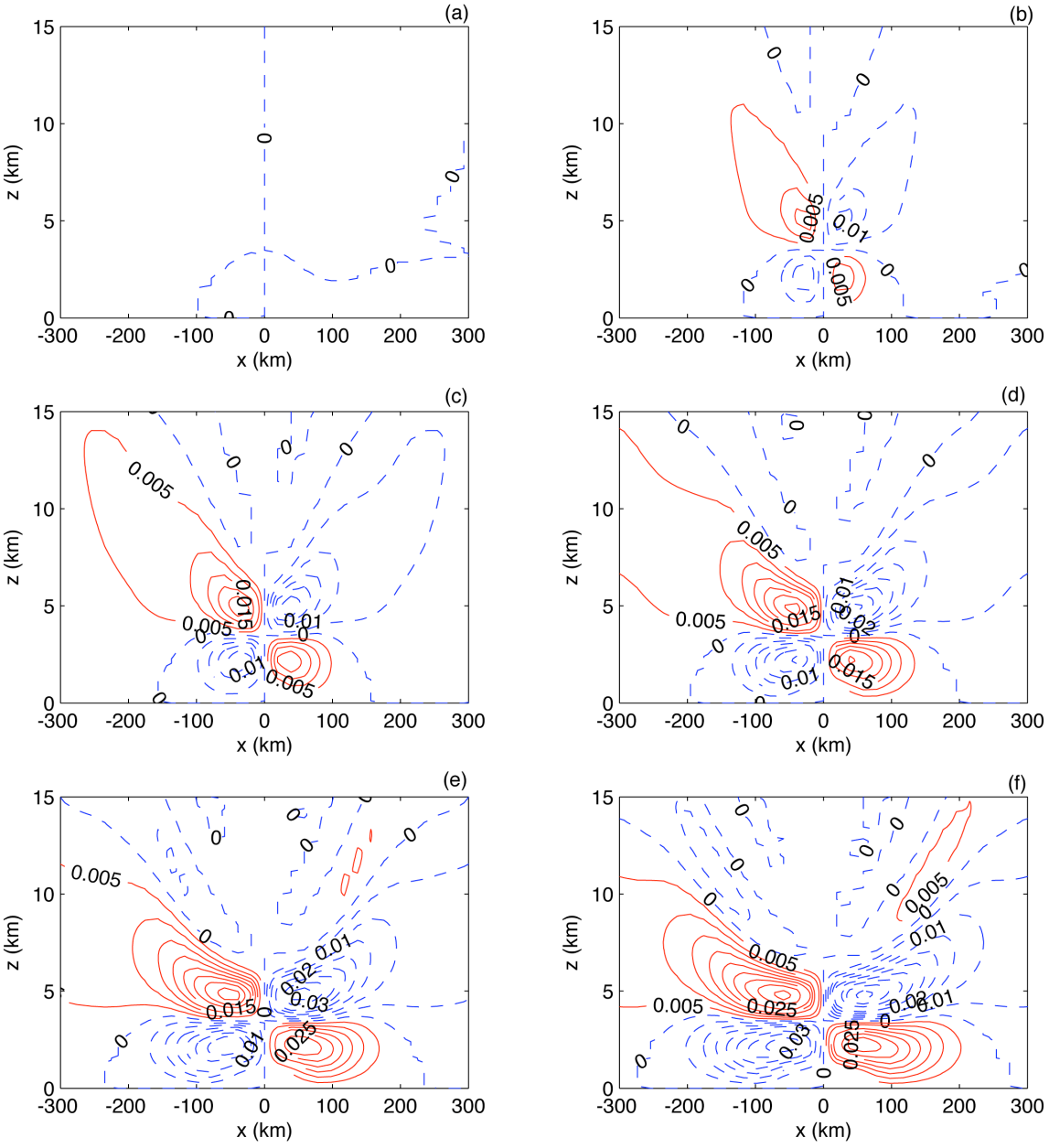

Figure 3.23: Contours of the potential temperature field at (a) 20 (b) 40 (c) 60 (d) 80 (e) 100 and (f) 120 minutes following an injection of y-momentum of duration 20 minutes. The contour interval is .005 K.

Table 3.1

Table 3.1: Maximum amplitude of the steady-state current (second column) as a function of the half-width a of the initial current (first column) following an injection of y-momentum of amplitude 1 m/s.

a (km)	**$|v_f|$ (m/s)**
2	.99
25	.89
100	.70
250	.50
1000	.23
2500	.12

3.4 Summary

Some basic properties of the adjustment process are demonstrated by considering a localized injection of heat. The comparison of adjustment to heat injection of varying spatial and temporal scales reveals the existence of several regimes comprising the adjustment. Here, we summarize the qualitative aspects of these regimes.

An instantaneous heat injection generates acoustic waves, which are primarily responsible for accomplishing an expansion of the heated region. With the exception of

the Lamb wave, acoustic waves are not excited by heating of duration exceeding several minutes. Though much diminished in amplitude, the Lamb wave may be generated by heating of a duration of several hours provided the horizontal scale is large. The parcel displacements associated with the acoustic waves are small relative to the buoyancy waves, though the pressure perturbation may be quite large.

An instantaneous heat injection also generates nonhydrostatic buoyancy waves, provided the vertical-horizontal aspect ratio is not very small. Such waves propagate much of their energy vertically and can accomplish a large vertical displacement of the heated column. The lowest vertical wavenumber modes have the largest horizontal group speed and are the first to emerge from the heated region. The primary signal associated with such waves is a vertical velocity (potential temperature) perturbation that is out of (in) phase with the heating accompanied by a pattern of upper/lower level outflow/inflow. Bretherton and Smolarkiewicz (1989) identify this signal as that required to remove the buoyancy excess associated with the cloud. As higher vertical wavenumber modes emerge slowly from the cloud, more complicated patterns of inflow and outflow are established both aloft and along the lower boundary. Chagnon and Bannon (2001) demonstrate that the lowest vertical wavenumber pattern contributes most significantly to the total displacement required to establish a balanced state. This balanced state is approximately trivial when the horizontal scale of the heating is very small compared to the Rossby deformation radius, which is O(1000km) for these experiments.

When the duration of heat injection is extended to twenty minutes and the aspect ratio is decreased to one tenth the transient motions are only weakly nonhydrostatic and occur on time scales longer than the shortest buoyancy period. Within two hours, the

transients disperse from the heated region leaving behind an approximately trivial balanced state. When the duration is extended to two hours and the aspect ratio is decreased one hundredth, the transient response involves only low frequency, hydrostatic buoyancy waves. After several hours the only transients remaining in the vicinity of the heated region are inertia-gravity waves oscillating slowly about a nontrivial balanced state.

The evolution of the inflow region beneath the heated core has some interesting properties. Following the initial upward displacement of the heated core and the onset of inflow, horizontally propagating rotors emerge along the lower boundary. The rotors result from the interaction of downward propagating buoyancy waves with the lower boundary. The velocity field associated with these rotors is directed opposite to the inflow and forces an outward and upward displacement of the inflow layer. Because the low-level inflow is believed to be essential to the self-aggregating properties of convective systems via the wave-CISK mechanism (Lindzen 1974, Raymond,1976), these lower boundary rotors could play a significant role in the evolution of organized cloud clusters.

The extent to which the type of injection affects the adjustment has also been examined. A vertical source/sink injection of mass induces an exaggerated acoustic response relative to that generated by an equivalent heating. However, the response during the buoyancy regime is indistinguishable from that following a heating. Injections of x-momentum and z-momentum primarily induce responses in which the propagation of energy is in the direction of momentum injection. For example, an injection of z-momentum is an efficient generator of vertically propagating buoyancy waves. Because

such buoyancy waves have relatively high frequency, i.e. approximately N_s, a long duration injection of z-momentum generates only a very weak response. Furthermore, the waves originate primarily from regions of convergence and divergence created by the injection. The response to an injection of y-momentum is very different because of the assumption of homogeneity in the y-direction. Convergence and divergence are generated very slowly following the deflection of the current by Coriolis forces. The response is therefore comprised mainly of hydrostatic, rotating buoyancy waves. The amplitude of the transient motions relative to the initial disturbance is proportional to the width of the initial disturbance. That is, unlike all of the other injection types, a smaller-scale injection of y-velocity projects most efficiently onto the steady state, whereas a larger-scale injection generates a maximum in wave energy.

Lamb's problem (1932) considered the vertical adjustment by a compressible atmosphere to horizontally homogeneous perturbations. The numerous recent extensions of Lamb's problem (Bannon 1995, Bannon and Sotack 1999, Kalashnik 2000, Duffy 2003) offer a theory to explain how an atmosphere establishes and maintains hydrostatic balance. Essentially, a warmed compressible atmosphere must expand vertically in order to establish hydrostatic balance. If the perturbation is introduced rapidly, then acoustic waves will provide most of the necessary displacement. The solution presented in this chapter places this theory in the more general context of vertical and horizontal adjustment. Strictly, Lamb's hydrostatic adjustment by acoustic waves explains only the horizontal wavenumber zero response. Nonhydrostatic buoyancy waves account for much of the adjustment when the injection aspect ratio is large. The time scale of these waves, and hence the time scale of hydrostatic adjustment, may be an order of magnitude longer

than the vertical acoustic adjustment. Furthermore, the acoustic adjustment is not confined to the vertical. The presence of a rigid lower boundary requires an increase/decrease in pressure throughout the depth of the atmosphere when the column attempts to expand/contract against the fixed lower boundary. This signal is communicated horizontally by the Lamb waves.

Any small set of experiments, such as those presented here, cannot adequately explore the vast parameter space describing the detail of the injection. The experiments involving a localized heat injection shown in this chapter describe the basic dynamics of adjustment. The comparison of the response to injections of heat, mass, and momentum indicate that the type of injection has a significant influence on the nature of the adjustment. However, a broader perspective of the relationship between the details of the injection and the response may be obtained by considering the potential vorticity distribution and energetics of these solutions. In chapter 4, we examine these issues.

Chapter 4

Potential Vorticity Conservation and Energy Partitioning

4.1 Introduction

Chapter 2 presented the solution to a linear compressible model of hydrostatic and geostrophic adjustment. In Chapter 3, the model solution was used to investigate the transient response of the statically stable large-scale environment to a rapidly-produced, localized imbalance. The imbalance is incorporated into the model as arbitrary nonhomogeneous "injection" terms in the momentum, mass, and thermodynamic equations. Specific solutions were demonstrated for idealized injection of heat of small, intermediate, and large scale as well as for injections of different type (i.e. mass and momentum). The goal of this chapter is to present a general picture depicting the relationship between the qualities of the imbalance generation mechanism and those of the response.

Potential vorticity (PV) and energy are useful properties to describe the general characteristics of an evolving geophysical flow. Both are globally conserved in the absence of injection functions. The complex transient dynamics of the externally forced solutions of chapter 3 and their dependence on the physical source (i.e. mass, momentum, heat) and spatial-temporal detail of the injection may be summarized conveniently using PV and energy.

The PV has been utilized by previous investigators in order to determine the steady hydrostatic and geostrophic response to an imbalance (e.g. Rossby 1938, Obukhov 1949, Schubert et al. 1980, Chagnon and Bannon 2001). In many applications, only the "mean" response to a given imbalance is of physical interest. When the transient dynamics on the *f*-plane are a matter of interest the application of PV must be made carefully because it uniquely determines the steady state but does not uniquely determine the transient character of the adjustment to that steady state.

Previous investigations of geostrophic adjustment have partitioned the energy associated with a given imbalance among the buoyancy waves and steady state (e.g., Veronis 1956, Vadas and Fritts 2001). Likewise, investigations of hydrostatic adjustment have partitioned the energy among acoustic waves and the steady state (Bannon 1995, Sotack and Bannon 1999). The energy of the transients was inferred by taking the difference between the energy of the initial imbalance and that remaining in the steady state. In the solution presented in the previous chapters, two distinct classes of transients are present: acoustic and Lamb waves and buoyancy waves. The previous method of inferring the energy partitioning is therefore insufficient. Chagnon and Bannon (2001) inferred the energy of the combined wave spectrum, but were unable to partition that energy into separate acoustic- and buoyancy-wave classes. Dikiy (1969) suggests that solutions of the type presented in chapter 2 can be written as a sum of distinct contributions from the steady state, acoustic, and buoyancy waves. A rigorous analysis of this assertion is given in appendix B that includes the injection terms.

This chapter examines the PV and energy of hydrostatic and geostrophic adjustment of a compressible atmosphere on the *f*-plane. This investigation elucidates the

dependence of the adjustment on injection type (e.g. mass, heat, or momentum) and spatial-temporal detail. Demonstration of the transient solution of chapter 3 is by itself insufficient for examining the large parameter space of the injection mechanisms.

4.2 Potential Vorticity Conservation

The PV is a scalar perturbation conserved by the compressible, homogeneous system (2.4) that consists of relative ζ_r and latent ζ_l vorticity:

$$q = \zeta_r + \zeta_l \quad , \tag{4.1}$$

where

$$\zeta_r \equiv \frac{\partial v}{\partial x} - \frac{\partial u}{\partial y} \quad , \quad \zeta_l = \zeta_e + \zeta_\theta \equiv -f\frac{\theta}{\theta_s} + \frac{f}{\theta_s}\frac{\partial}{\partial z}\left(\frac{\theta_s\, g\, \theta}{N_s^2\, \theta_s}\right) \quad . \tag{4.2}$$

For the moment, we relax the assumption of homogeneity in the y-direction. The latent (i.e. hidden or unrealized) vorticity is comprised of an elastic contribution ζ_e as well as a thermal stratification contribution ζ_θ. The elastic contribution is absent in the anelastic and Boussinesq approximations. The conservation of each contribution to the PV is described by

$$\frac{\partial \zeta_r}{\partial t} = -f\left(\frac{\partial u}{\partial x} + \frac{\partial v}{\partial y}\right) + \left(\frac{\partial \dot{v}}{\partial x} - \frac{\partial \dot{u}}{\partial y}\right) , \tag{4.3a}$$

$$\frac{\partial \zeta_e}{\partial t} = f\left(\frac{\partial u}{\partial x} + \frac{\partial v}{\partial y}\right) + \frac{f}{\theta_s}\frac{\partial}{\partial z}(\theta_s w) - f\frac{\dot{\theta}}{\theta_s} \quad , \tag{4.3b}$$

$$\frac{\partial \zeta_\theta}{\partial t} = -\frac{f}{\theta_s}\frac{\partial}{\partial z}(\theta_s w) + \frac{f}{\theta_s}\frac{\partial}{\partial z}\left(\frac{\theta_s\, g\, \dot{\theta}}{N_s^2\, \theta_s}\right) \quad . \tag{4.3c}$$

The sum of (4.3a-c) implies that in the absence of external injection the PV is conserved locally: $\partial q/\partial t = 0$. In the presence of external injection, the PV satisfies

$$\frac{\partial q}{\partial t} = \frac{\partial \dot{v}}{\partial x} - \frac{\partial \dot{u}}{\partial y} - f\frac{\dot{\rho}}{\rho_s} + f\frac{\partial}{\partial z}\left(\frac{\rho_s g \dot{\rho}}{N_s^2 \rho_s}\right) \quad . \tag{4.4}$$

Figure 4.1 depicts schematically the conservation of PV given by (4.3). Latent vorticity may be generated by injection of heat or mass, and relative vorticity may be generated by injection of horizontal momentum with vorticity. Following the initial generation, vorticity is converted among the various contributions. For example, consider an injection of heat. Initially, the injection of heat decreases/increases the thermal stratification above/below the level of maximum heating. Consequently, there is negative/positive latent vorticity in the region above/below the maximum heating. The associated pressure gradient next drives an expansion of the heated column. This initial expansion is primarily upward due to the restriction imposed by the rigid lower boundary and the distribution of mass in the basic state, as was observed in chapter 3. [It should be noted that some of the initial expansion occurs horizontally outward, accomplished by Lamb waves.] Below the maximum heating, the upward vertical expansion can result in either 1) a decrease in the perturbation density or 2) horizontal convergence. In the first case, some of the positive latent thermal-stratification vorticity is converted into positive latent elastic vorticity. In the second case, there is a conversion of positive latent vorticity to positive relative vorticity required by the conservation of absolute angular momentum. We therefore expect an injection of heat to induce a cyclone below the level of maximum heating whose strength is mitigated in part by the compressibility of the fluid. Similarly, we expect an anticyclone to develop above the level of maximum heating. Such

characteristics were observed in the steady state by Chagnon and Bannon (2001). Figure 4.1 does not by itself imply a causality relationship between the various injections, conversion mechanisms, and latent and relative vorticity. Causality is inferred by examining the complete dynamics of the system.

Equation (4.4) implies that injections of different type may generate equivalent distributions of potential vorticity and therefore the same steady state. Furthermore, the steady state depends only on the time integral of the injection and not its temporal details. In section 4.5 we compare the energy of PV-equivalent injections in order to demonstrate the extent to which they induce equivalent adjustment processes. The transient response to such injections may be very dissimilar.

Applying the assumption made in chapter 2 that the model is homogeneous in the *y*-direction, equation (4.4) implies that an injection of either *x*-momentum or *z*-momentum does not generate any perturbation PV and therefore does not induce a perturbation steady state. An injection of *x*-momentum and the subsequent deflection of this current by Coriolis forces may not produce a pressure gradient in the *y*-direction. Instead, the deflected current undergoes an inertial oscillation and there is no mechanism for the retention of a horizontal mass gradient in the asymptotic steady state. Similarly, an injection of *z*-momentum does not generate a response involving permanent changes to the fluid center of gravity. Furthermore, the global PV [defined as the total PV per unit mass $\int_V \Box_s q \; dV$] remains constant if the injection mechanism on the right-hand side of (4.4) satisfies several necessary conditions: an injection of heat must be zero on the upper and lower boundaries; an injection of mass must conserve the total fluid mass; and an

Figure 4.1

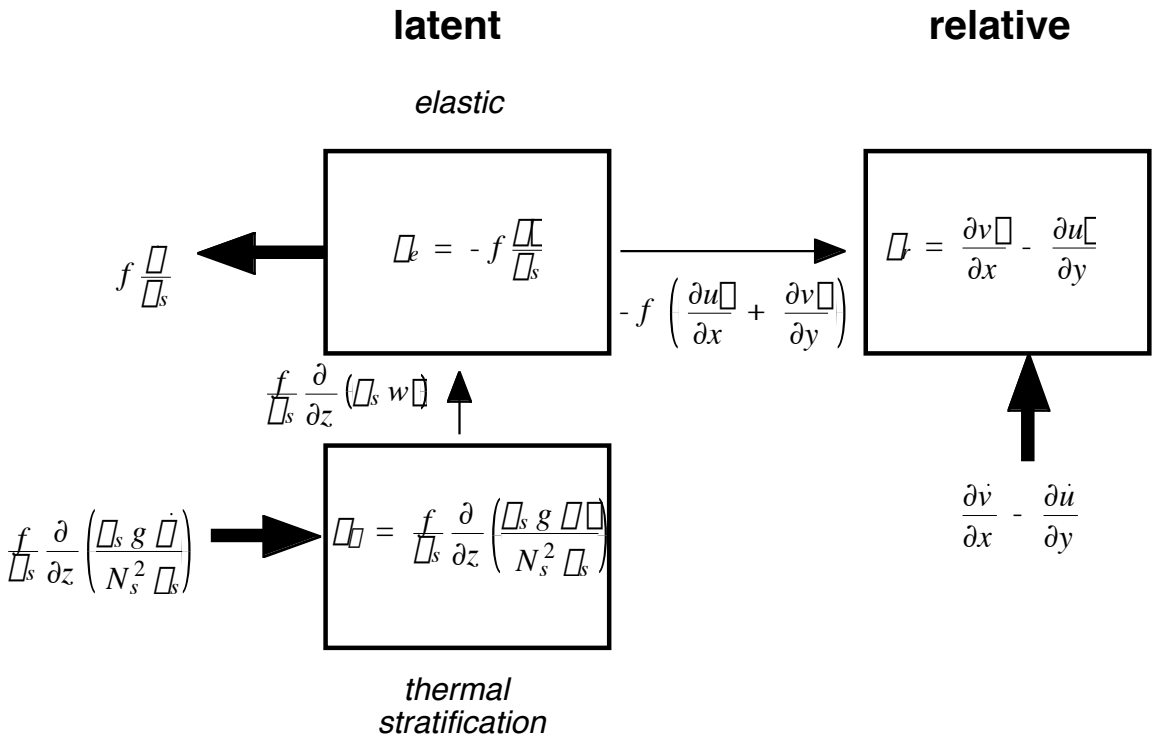

Figure 4.1: Schematic illustration of the potential vorticity balance. The potential vorticity is comprised of latent and relative vorticity. The latent vorticity is in turn comprised of a thermal stratification and an elastic contribution. Thick arrows denote generation mechanisms. Thin arrows denote positive conversion mechanisms.

injection of momentum must not induce a net torque about the vertical direction. An injection of momentum satisfying a periodic lateral boundary condition satisfies this criterion.

The PV written in terms of the field variable transformation introduced in chapter 2 is

$$Q \equiv \rho_s^{1/2} q = \frac{\partial V}{\partial x} + \frac{f}{\rho / H_s}\left(\frac{\partial}{\partial z} - \rho\right) S - \frac{f}{c_s^2} P \quad , \tag{4.5}$$

which may be written in spectral space as

$$Q_n = i k V_n - \frac{f\left(m^2 + \rho^2\right)}{\rho / H_s} S_n - \frac{f}{c_s^2} P_n \quad , \tag{4.6}$$

where Q is expanded about the vertical basis function f_n. Following the convention used in chapter 2, the subscript k denoting the Fourier transform of the horizontal structure is implied but omitted and solutions are assumed homogeneous in y-direction. It may be verified readily that any transient solution (2.19) of the homogenous system (i.e. with nonzero frequency ω_i) contains no PV, $Q_n = 0$. This is not generally the case for models in which the basic state contains nonzero gradients of PV. The perturbation in PV introduced by the injection mechanism is therefore comprised only of the hydrostatic and geostrophic (i.e. steady-state) class. In terms of Fig. 4.1, the buoyancy-wave, acoustic-wave, and Lamb-wave classes contain no PV. That is, the waves contain portions of relative and latent vorticity that are equal in magnitude but opposite in sign. For the steady-state class, which we can refer to interchangeably as the PV-conserving class, we may write (4.6) in terms of the steady contribution to the pressure field,

$$Q_n = Q_{n,\,steady} = -f\left(m^2 + \rho^2 + \frac{N_s^2}{f^2} k^2 + \frac{N_s^2}{c_s^2}\right) P_{n,\,steady} \quad . \tag{4.7}$$

The solution of (4.7) is a generalization of the solution presented in Chagnon and Bannon (2001).

4.3 Energy Conservation

Chagnon and Bannon (2001) presented a discussion of the available energetics, including the mechanisms of conversion between kinetic (KE), available potential (APE), and available elastic (AEE) energies. Figure 4.2 generalizes Fig. 1 of Chagnon and Bannon (2001) to include the additional injection types. Because the various types initially generate different forms of energy, we anticipate the subsequent energy balance and exchange to depend on the type. This dependence is the concern of section 4.4. The purpose of this section is to assess the basic properties of the energetics of the time-dependent solutions. The following will demonstrate that the energy is comprised of distinct contributions from each of the spatial modes, which in turn are comprised of distinct contributions from each class of transient. This kind of representation is not always possible, such as in the case of certain sheared flows (Held 1985), and must therefore be treated explicitly (see appendix B).

The energy density is

$$TE = \frac{1}{2}\left(U^*U + V^*V + W^*W + \frac{g^2}{N_s^2}S^*S + \frac{1}{c_s^2}P^*P\right), \tag{4.8}$$

where a superscript * denotes a complex conjugate. Equation (4.8), expressed in terms of the field variable transformation, is the traditional available energy density whose general

Figure 4.2

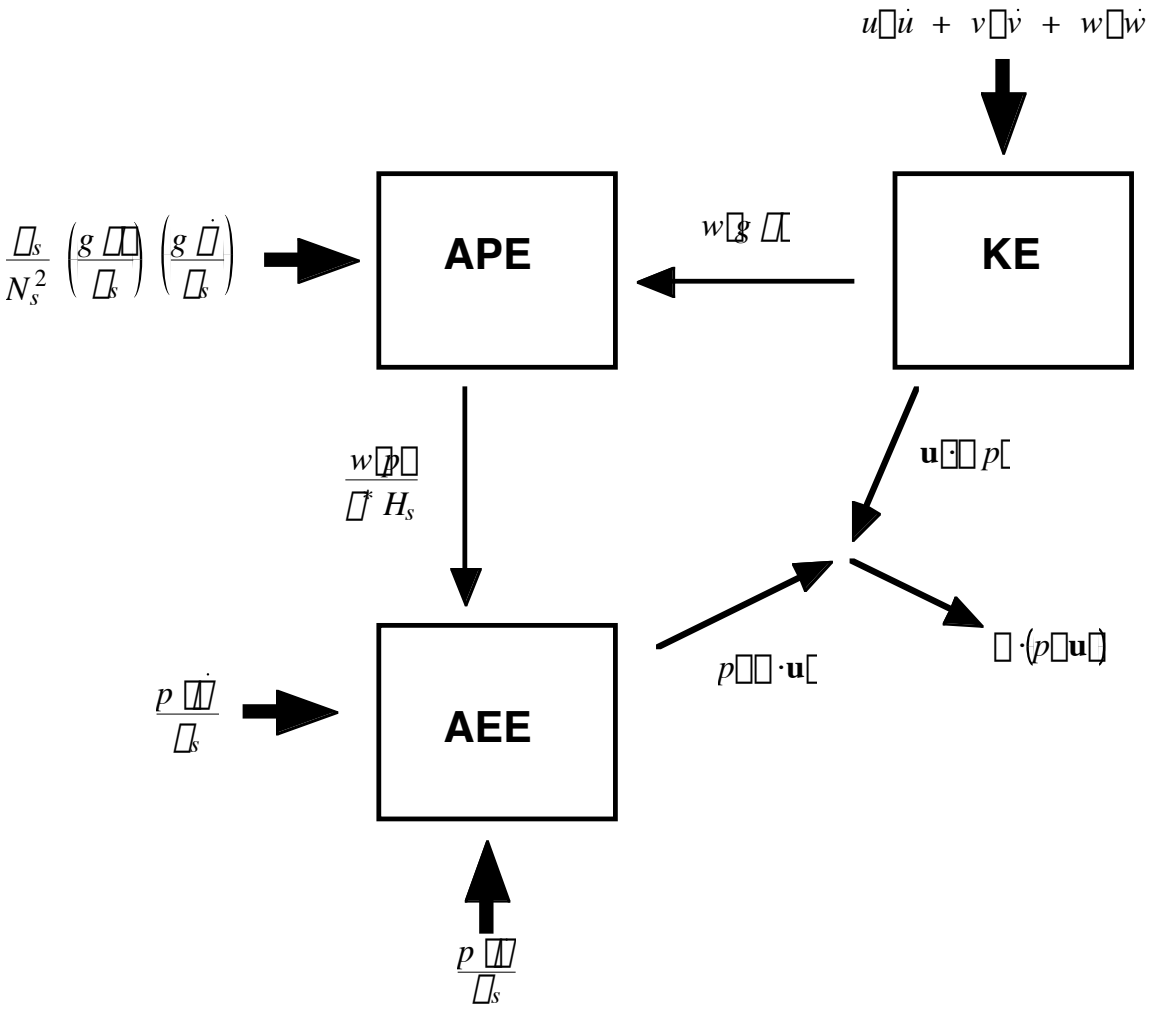

Figure 4.2: Schematic illustration of the energy conversion between available potential (APE), available elastic (AEE), and kinetic energy (KE). Thick arrows denote the generation mechanisms. Thin arrows denote positive conversion mechanisms.

conservation is represented in Fig.4.2. The first three terms comprise the KE, the fourth is the APE, and the last is the AEE. The energy density is governed by

$$\frac{\partial}{\partial t}(TE) + \nabla\cdot(P\,\mathbf{U}) = U^*\dot{U} + V^*\dot{V} + W^*\dot{W} + \frac{g^2}{N_s^2}S^*\dot{S} + \frac{1}{c_s^2}P^*\dot{P} \quad , \quad (4.9)$$

where $\nabla \equiv (\partial/\partial x, \partial/\partial y, \partial/\partial z)$ and $\mathbf{U} \equiv (U, V, W)$. The global integral of the divergence of the energy flux vector $P\mathbf{U}$ is zero for periodic or closed rigid boundaries. In the absence of an injection, the energy is conserved globally.

Because the spatial modes (2.12) are orthogonal, we may consider the conservation of the spectral energy density,

$$TE_n = \frac{D\left(m^2 + \nabla^2\right)}{2}\left[U_n^*U_n + V_n^*V_n + \left(m^2 + \nabla^2\right)\left(W_n^*W_n + \frac{g^2}{N_s^2}S_n^*S_n\right) + \frac{1}{c_s^2}P_n^*P_n\right]. \quad (4.10)$$

The spectral energy density is dependent on the horizontal k and vertical wavenumber m of the mode. Each mode is in turn comprised of acoustic-wave, buoyancy-wave, and PV-conserving classes. Appendix B demonstrates that there is no interaction among these distinct classes even in the presence of active injections. The spectral energy density may therefore be partitioned among the classes:

$$TE_n = TE_n^{PV} + TE_n^a + TE_n^b \ . \quad (4.11)$$

Following the shut-off of the injection mechanisms, the distinct acoustic-wave, buoyancy-wave, and PV-conserving (i.e. steady) contributions to the spectral energy density are time-independent. Each of these contributions consists of KE, APE, and AEE that undergo time-dependent conversions according to Fig. 4.2.

The spectral energy density excited by an injection may be generalized in terms of the partitioning of the temporal Green's function solution (i.e. the response to an

instantaneous injection). Let the spectral energy density of the temporal Green's function be given by

$$\widehat{TE}_n = \widehat{TE}_n^{PV} + \widehat{TE}_n^{a} + \widehat{TE}_n^{b} \quad . \tag{4.12}$$

We may then write the time-dependent spectral energy density in terms of the spectral energy density of the Green's function

$$TE_n(t) = r(0,t)\,\widehat{TE}_n^{PV} + r(\omega_a, t)\,\widehat{TE}_n^{a} + r(\omega_b, t)\,\widehat{TE}_n^{b} \quad , \tag{4.13}$$

where the filtering function r depends on the frequency of the contribution and is given by

$$r(\omega, t) = \left(\int_0^t e^{-i\omega t}\,\Omega_i(t)\,dt\right)\left(\int_0^t e^{i\omega t}\,\Omega_i(t)\,dt\right) \quad , \tag{4.14}$$

and $\Omega_i(t)$ is a function describing the time-dependence of the injection function. Through the representation of the energy partitioning (4.13) we may investigate separately the effects of the spatial and temporal characteristics of the injection on the partitioning. The temporal Green's function energy partitioning contains the dependence of the spatial characteristics as well as the type of injection. The filtering function (4.14) incorporates all of the time-dependent effects. The result (4.13-4.14) is a generalization of the buoyancy wave filtering demonstrated by Vadas and Fritts (2001).

Consider some examples of the filtering function. The first example is that of the Dirac delta function $\Omega_i(t) = \delta(t)$, for which the filtering function is $r(\omega,t) = 1$. In this case the partitioning is that of the temporal Green's function, which is demonstrated in the proceeding section. Another example is for a top-hat injection of duration τ, $\Omega_i(t)$ =

$[H(t) - H(t-\tau)]/\tau$, where H is the Heaviside step function. The filtering function for this injection is

$$r(\omega,t) = \frac{1}{(\omega\tau/2)^2} \begin{cases} \sin^2\left(\frac{\omega t}{2}\right), & t < \tau \\ \sin^2\left(\frac{\omega\tau}{2}\right), & t \geq \tau \end{cases} . \tag{4.15}$$

An injection that is somewhat smoother in time such as $\dot{\varepsilon}_i(t) = 2[H(t) - H(t-\tau)]\sin^2(\pi t/\tau)/\tau$ has a filtering function given by

$$r(\omega,t) = \frac{1}{(\omega\tau/2)^2}\left[\frac{\left(\frac{2\pi}{\tau}\right)^2}{\omega^2 - \left(\frac{2\pi}{\tau}\right)^2}\right]^2 \begin{cases} \sin^2\left(\frac{\omega t}{2}\right), & t < \tau \\ \sin^2\left(\frac{\omega\tau}{2}\right), & t \geq \tau \end{cases} . \tag{4.16}$$

Figure 4.3 presents the filtering functions (4.15-4.16) for $t > \tau$. Waves are filtered relative to the Green's function solution. The filtering is an increasing function of the wave frequency and of the injection duration. For example, an injection of duration exceeding several minutes should not generate much acoustic-wave energy. The sine-squared in time provides a smoother filter with less energy remaining in the higher order harmonics.

Figure 4.3

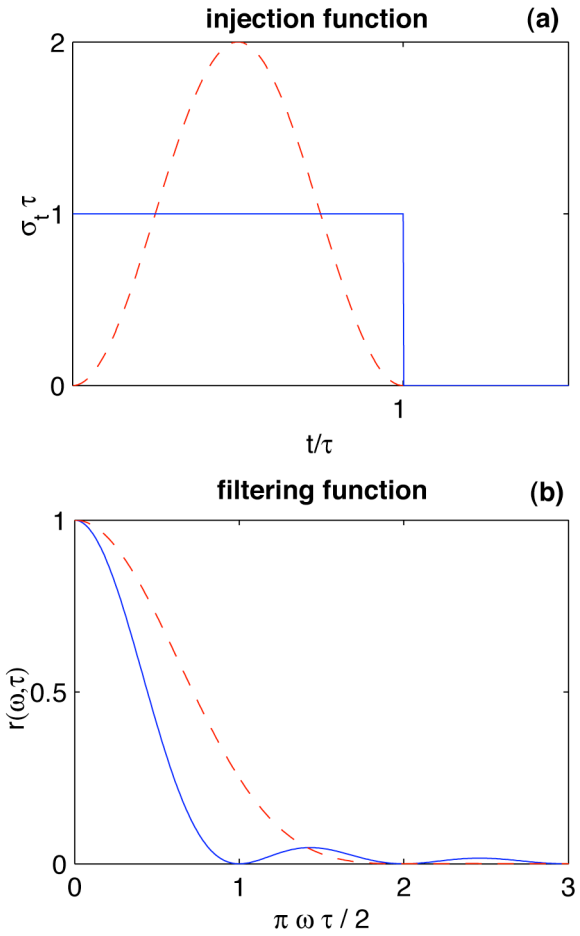

Figure 4.3: (a) Top-hat (solid) and sine-squared (dashed) injection functions $\sigma_t(t)$ and (b) their corresponding filtering functions for $t > \tau$ plotted as a function of the injection duration parameter τ times the frequency ω of the mode.

4.4 Energy Spectrum

This section demonstrates some basic properties of the energy spectrum and its partitioning. The presentation begins with the partitioning of each wave class among KE, APE, and AEE as a function of the horizontal k and vertical wavenumber m of the mode. The relative proportions of the time-averaged KE, APE, and AEE in each wave class are a function only of the dispersion relation and are independent of the properties of the injection mechanism. Next, we examine the effect of the injection type on the partitioning of the spectral energy density among each class (i.e. acoustic-wave, buoyancy-wave, Lamb-wave and PV-conserving contributions) following instantaneous injections. The qualities of the former partitioning are consistent with the characteristics of the latter partitioning. As in chapter 3, the basic state parameters are chosen to represent a typical stably-stratified, midlatitude, synoptic-scale environment: $T_* = 255$ K, $p_* = 1000$ mb, $\rho_* = 1.37$ kg m^{-3}, $N_s = .0194$ s^{-1}, $H_s = 7.48$ km, $c_s = 320$ m s^{-1} and $f = 10^{-4}$ s^{-1}.

4.4.1 Partitioning of Energy in Each Class Among KE, APE, and AEE

For each time-dependent class of a given (spatial) mode, the relative proportions of the time-averaged KE, APE, and AEE are fixed. [Note: at any instant in time there is an exchange between the energy terms according to Fig. 4.2, e.g. the KE may be zero at one instant and nonzero at some later instant at the expense of APE.] The ratios of these time-averaged energies, derived from the dispersion relation (2.16), are:

$$\overline{APE} : \overline{AEE} = \frac{c_s^2 \left(m^2 + \square^2\right) N_s^2}{\left(N_s^2 - \square^2\right)^2} \quad , \tag{4.17a}$$

$$\overline{KE_z} : \overline{APE} = \frac{\square^2}{N_s^2} \quad , \tag{4.17b}$$

$$\overline{KE_x} : \overline{APE} = \left(\frac{N_s^2 - \square^2}{f^2 - \square^2}\right)^2 \left(\frac{\square^2 + f^2}{N_s^2}\right)\left(\frac{k^2}{m^2 + \square^2}\right) \quad , \tag{4.17c}$$

where an overbar denotes the unweighted time-average, and the KE is separated into horizontal (KE_x) and vertical (KE_z) contributions. The overbar denoting the temporal average is omitted from the following figures.

Figure 4.4 presents this partitioning for the PV-conserving, acoustic-wave, and buoyancy-wave classes. For the PV class (Fig. 4.4a), the ratio of AEE to APE is largely independent of horizontal scale over the range of scales presented. In the steady state, this ratio depends on the magnitude of the pressure perturbation required to maintain a hydrostatic balance versus the horizontal gradient of mass required to support a geostrophic current. Except for the deep modes, the APE is much larger than the AEE in the steady state. For the deep mode, the hydrostatic pressure perturbation is larger relative to the density perturbation because the depth-scale of the vertical gradient is larger. The ratio of KE_x to APE in the steady state (note that $KE_z = 0$), implied by (4.17c) with $\square = 0$, is given by a modal Burger number, $k^2 N_s^2/(m^2 + \square^2) f^2$. At small horizontal scales the KE_x is very large compared to the APE required to maintain geostrophic balance. At very large horizontal scales the KE_x is small compared to the APE because the magnitude of horizontal gradients in APE is vanishingly small.

Figure 4.4

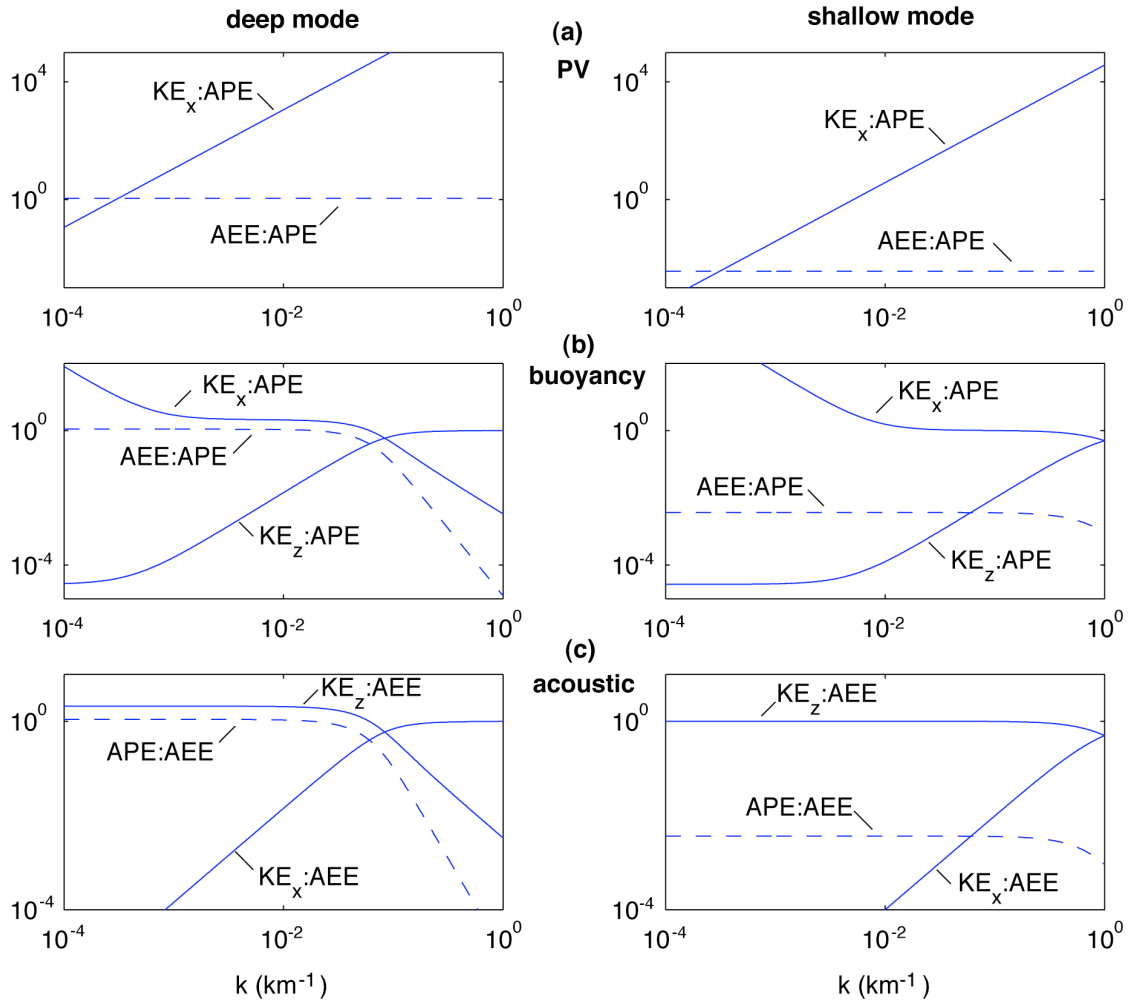

Figure 4.4: Ratios of KE to AEE or APE (solid lines) and APE to AEE or its inverse (dashed lines) for the (a) PV-conserving, (b) buoyancy-wave, and (c) acoustic-wave classes as a function of horizontal wavenumber k. The first column gives the ratios for a deep mode (m = 1/20 km) and the second for a shallow mode (m = 1/1 km).

For the buoyancy waves (Fig. 4.4b), AEE is only significant relative to the APE for the widest structures. Such buoyancy waves produce parcel displacements that are primarily horizontal and are approximately hydrostatic. The nonhydrostatic buoyancy modes contain larger proportions of APE relative to AEE. The restoring force of these waves is primarily the vertical buoyancy force. In the small horizontal scale limit, the energetics involves primarily vertical KE and APE, i.e. as $k \to \infty$, $KE_z:APE \to 1$. Such waves approach pure buoyancy oscillations that induce strictly vertical parcel motions. For the widest and shallowest structure, the KE associated with horizontal motions is very large compared to the APE, i.e. as $k \to 0$, $KE_x:APE \to \infty$. Such buoyancy waves are actually inertia gravity waves. Only through vertical motions are buoyancy waves able to convert energy efficiently between KE and APE, i.e. as $k \to 0$, $KE_z:APE \to f^2/N_s^2 << 1$.

For the acoustic waves (Fig.4.4c), the AEE is very large compared to the APE except for the deepest structures that contain approximately equal portions of APE and AEE. Only for these deepest structures are the vertical displacements associated with the acoustic waves large enough to affect a change in the potential temperature. Acoustic waves are most efficient at converting energy between KE and AEE. For relatively deep and narrow structures the particle motions are approximately horizontal and the acoustic energy is comprised of approximately equal parts of vertical KE and AEE, and vice versa for shallow and wide structures, i.e. if $m^2 >> k^2$, then $KE_z:AEE \to 1$ and if $k^2 >> m^2$ then $KE_x:AEE \to 1$.

For the Lamb mode (not shown in Fig. 4.4), the partitioning consists of only AEE and KE_x. For the acoustic class of the Lamb mode, i.e. the Lamb wave, the average proportions of these energies is

$$\overline{KE_x}:\overline{AEE} = \frac{c_s^2 k^2 + 2f^2}{c_s^2 k^2} \ . \tag{4.18}$$

At small horizontal scale, the Lamb wave contains approximately equal portions of AEE and KE_x. At large horizontal scale, the Lamb wave contains a much larger portion of KE. For the steady class of the Lamb mode:

$$\overline{KE_x}:\overline{AEE} = \frac{c_s^2 k^2}{f^2} \ . \tag{4.19}$$

As in Fig. 4.4a, the steady state contains a significant relative proportion of KE_x only at the narrowest horizontal scales. At such scales, only a small change in the horizontal distribution of mass is required to balance an injected current.

The partitioning of the energy in each class among KE, APE, and AEE is useful for explaining the partitioning of total energy associated with a given injection function among the classes of time dependence. In order to establish a framework for the following analysis, Fig. 4.5 schematically represents the partitioning of energy between the transient and the PV classes during adjustment. The injection generates a perturbation in the energy distributed in some manner between KE, APE, and AEE, denoted by the large box on the left in Fig 4.5. The magnitude and proportions of these energies are likely to differ from that of the PV-conserving class and an adjustment must take place. Depending on the nature of this unbalanced configuration, some of this energy is projected onto the acoustic, buoyancy, and Lamb waves as denoted by the boxes in the

middle of Fig. 4.5. The time-averaged energy in each of these classes is distributed among KE, APE, and AEE in a manner that depends on the modal partitioning in Fig. 4.4. Following the propagation and dispersion of the transients, the remaining energy is in the steady state that, according to Fig. 4.4, is restricted in its ability to contain certain average proportions of KE, APE, and AEE. These restrictions depend on the basic physical properties of the wave, including the restoring and energy conversion mechanisms.

Figure 4.5

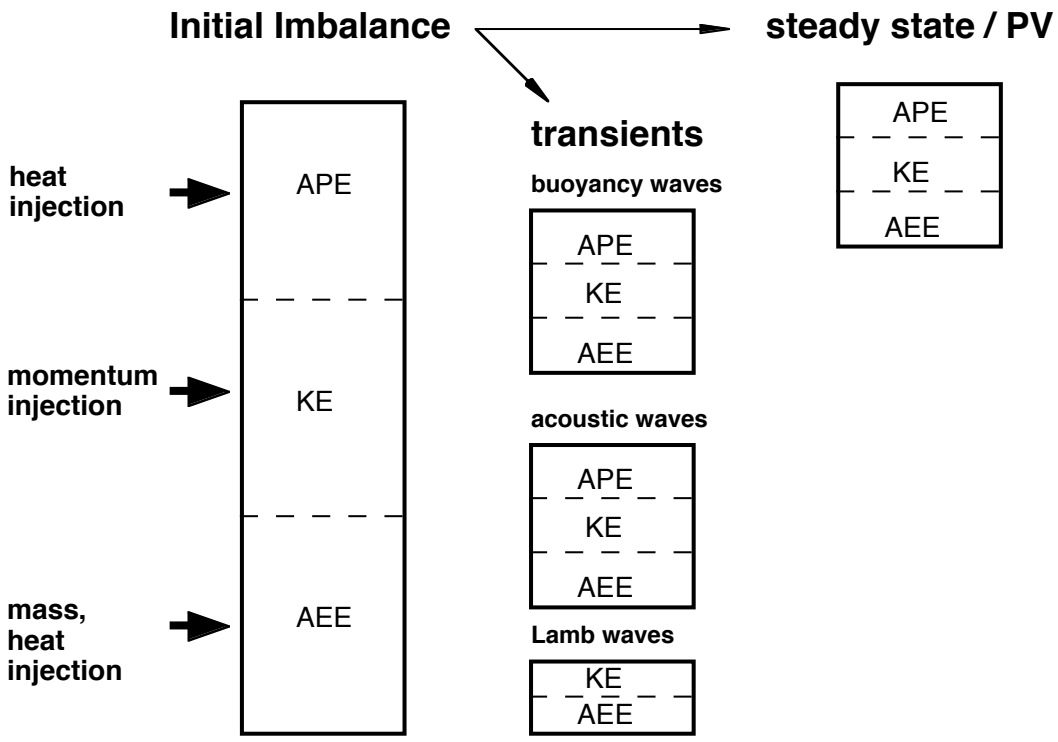

Figure 4.5: Schematic illustration of the transition from the energy configuration of the initial unbalanced state to the final balanced state. The boxes denote the total energy contained in each state. The dashed lines represent the time-averaged proportions of APE, KE, and AEE contributing to the total energy. The proportions drawn here are arbitrary and are generally dependent on the details of the initial disturbance.

4.4.2 Dependence of Energy Partitioning on Injection Type

The partitioning of energy among the PV, acoustic-wave, buoyancy-wave and Lamb-wave classes depends strongly on the injection type. In this subsection, we consider an instantaneous injection that projects equally onto all horizontal and vertical modes such that energy contained in each mode is constant and the partitioning is that of the temporal Green's function (4.12). Such an injection is unphysical, but may be used to demonstrate the dependence of the energy partitioning on the structure of the injections and its type. Essentially, we are interested in the ratios

$$\widehat{R}_n^a = \frac{\widehat{TE}_n^a}{\widehat{TE}_n}, \quad \widehat{R}_n^b = \frac{\widehat{TE}_n^b}{\widehat{TE}_n}, \quad \widehat{R}_n^{PV} = \frac{\widehat{TE}_n^{PV}}{\widehat{TE}_n}, \tag{4.20}$$

which, at a fixed horizontal wavenumber, are independent of the vertical structure of the injection function for all but the case of a heat injection. Because a heating projects initially onto both the pressure and potential temperature, which are represented by two distinct nonorthogonal vertical structures, the partitioning is complicated for a heating. We therefore construct two partitionings for the heat injection - one representing the generation of APE and one for the initial generation of AEE that both contribute to the actual partitioning associated with a heat injection. The actual partitioning is not a simple sum of these two cases and it is actually impossible to construct an injection of heat that generates nonzero APE and zero AEE. However, all other injections are capable of generating one initial form of energy exclusively.

Figure 4.6a presents the partitioning (4.20) for an injection of *x*-momentum. The injection of *x*-momentum generates no PV, and the partitioning consists only of acoustic and buoyancy contributions. The acoustic waves dominate the energy spectrum when the injection projects onto narrower, deeper structures, which may be understood by considering the initial response to this injection. Initially, all the fields except *x*-momentum are zero. Because the PV is zero, the horizontal KE associated with this perturbation must be removed entirely by the transients. For shallow and wide structures, buoyancy waves contain mainly horizontal parcel motions, while acoustic waves contain vertical parcel motions. The initial horizontal KE therefore projects onto inertia-gravity waves. For deep and narrow structures, horizontally propagating acoustic waves are more efficient at carrying the initial KE.

Figure 4.6b presents the partitioning (4.20) for an injection of *y*-momentum. The partitioning consists mainly of buoyancy waves dominant at low aspect ratio, and PV dominant at high aspect ratio. Acoustic waves are not generated significantly [maximum fraction < 10^{-3}%). Initially, all the fields except *y*-momentum are zero. There is no divergence associated with this current because the solutions are assumed homogeneous in the *y*-direction. The slow deflection of this current by the Coriolis force generates patterns of convergence and divergence and associated tendencies of pressure to the right and left of the current. These transient motions are accomplished by low frequency buoyancy waves, which are only efficiently excited when the injection aspect ratio is small. For a narrow and deep injection, the PV component is dominant. Figure 4.4a demonstrates that the ratio of KE_x to APE required in the steady state is large on scales that are narrow compared to the modal Rossby radius of deformation $L_R = N_s / f m$. The

initial distribution of KE therefore requires only a small change in APE to achieve the steady state. In other words, at small horizontal scale (compared to L_R), the pressure field does not require significant adjustment to balance the initial velocity - i.e. only a small change in APE is required to balance the KE associated with current. The small change in the horizontal gradient of pressure may then be accomplished by waves of low energy relative to the kinetic energy of the current.

Figure 4.6c presents the partitioning (4.20) for an injection of z-momentum. The partitioning does not contain a steady contribution since the injection of z-momentum does not generate any PV. Initially, all of the fields are zero except the vertical velocity. The initial state consists entirely of KE_z that must be removed by the transients. The acoustic waves dominate the partitioning at small aspect ratio - a behavior somewhat inverse to that of the x-momentum injection. Figure 4.4b,c demonstrates that acoustic waves of small aspect ratio or buoyancy waves with large aspect ratio are most efficient carrying a significant proportion of KE_z.

Figure 4.6d presents the partitioning (4.20) for an injection of mass. The partitioning consists of a PV-conserving contribution at small aspect ratio, a buoyancy-wave contribution at intermediate aspect ratio, and a very large acoustic-wave contribution significant at all but dominating at large aspect ratio. Initially, all of the fields are zero except the density and pressure. All of the initial energy is AEE. This energy must be converted into APE and KE in the steady state (Fig. 4.4a), with larger conversions for deeper structures. Only at very deep and wide scales may this energy project directly onto the steady state. Much of the initial AEE must therefore project onto the transients. Buoyancy waves are only generated significantly when the injection is

deep because only such buoyancy waves contain very much AEE (Fig. 4.4b). Acoustic waves are dominant otherwise since they consist largely of AEE (Fig. 4.4c). Because the acoustic waves primarily accomplish a vertical adjustment (i.e. have approximately equal portions of AEE and KE_z), much of the adjustment is dominated by vertically propagating acoustic waves.

For the reasons discussed above, we must analyze an injection of heat differently. We may consider heat injection in two parts: the initial generation of AEE (i.e. initial projection onto the pressure) and the initial generation of APE (i.e. initial projection onto potential temperature). The first is largest when the heating duration is short compared to the acoustic adjustment time scale (i.e. > several minutes). This response to the initial generation of AEE was treated above and is identical to the injection of mass. The response to the initial generation of APE is presented in Fig. 4.6e. The partitioning consists of a PV-conserving contribution that is large at wide scales and gives way to buoyancy waves at narrower scales. Acoustic waves comprise a significant portion of the spectrum only when the heating is deep and wide. To understand this partitioning, we consider the required energy conversions. The steady state may not contain APE exclusively (Fig. 4.4a). At wide and deep scales, the energy of the steady state consists of approximately equal parts of AEE and APE. The transients that are most capable of converting the initial APE in this manner are acoustic waves (Fig. 4.4c). At smaller scales the energy of the steady state must contain a significant portion of KE. The transients most capable of converting APE in this manner are buoyancy waves (Fig. 4.4b).

The Lamb mode is a distinct vertical structure and must be considered separately. Figure 4.7 presents the partitioning for the Lamb mode, which contains only an acoustic-

wave and steady class. Injections of x- and z-momentum (omitted from Fig. 4.7) do not generate any PV, and the Lamb mode contains only an acoustic class (i.e. Lamb waves). An injection of y-momentum (Fig. 4.7a) projects onto the steady state at narrow horizontal scale compared to L_R and the acoustic waves at wide horizontal scale. The proportion of AEE to KE in the steady state is very small at narrow horizontal scale and the initial current does not require very much conversion by the waves. At larger scales this conversion is accomplished by waves under the influence of the background rotation that we may refer to as inertia-Lamb waves. A heating or injection of mass (Fig. 4.7b) projects onto acoustic waves at narrow horizontal scale and a steady state at wider horizontal scale. Such injections generate a significant initial distribution of AEE. Only at the very widest scales on which the magnitude of horizontal gradients is small may the Lamb mode provide a significant steady-state contribution relative to its wave contribution.

Figure 4.6

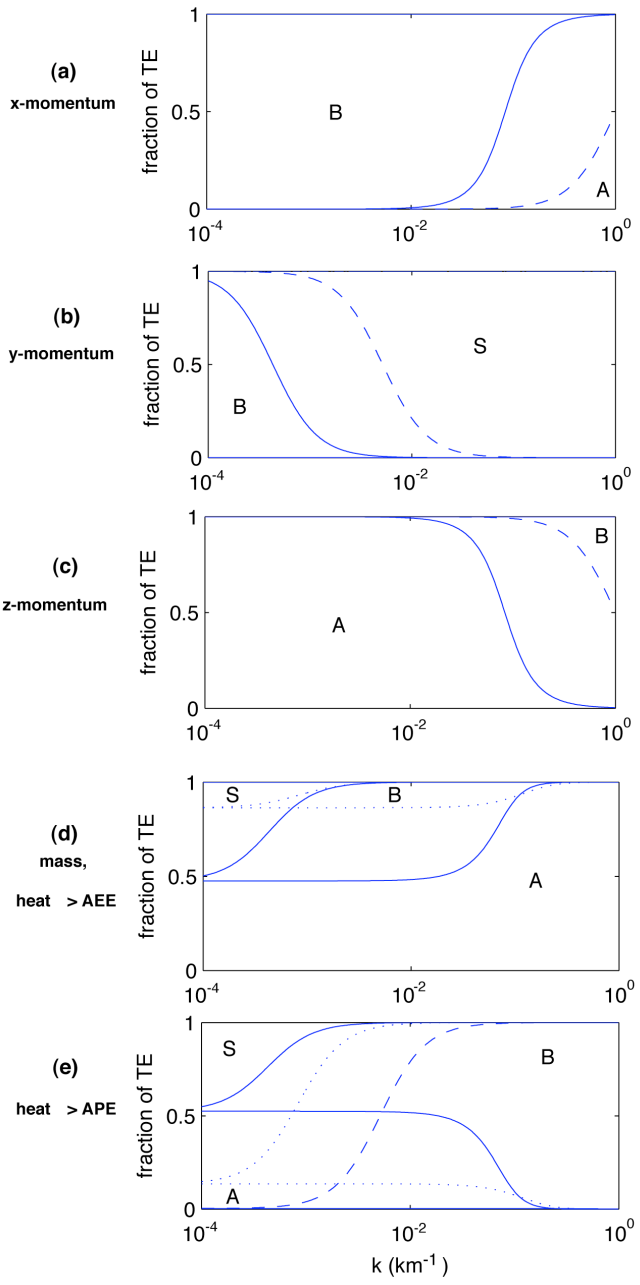

Figure 4.6: Partitioning of the total energy among steady (S), acoustic-wave (A), and buoyancy-wave (B) classes for injections of (a) x-momentum, (b) y-momentum, (c) z-momentum, (d) mass/heat (AEE), and (e) heat (APE) that project equally onto all horizontal modes. The solid lines mark the partitioning for a deep mode (m = 1/20 km), the dashed for a shallow mode (m = 1/1 km), and the dotted for an intermediate mode (m = 1/6.7 km).

Figure 4.7

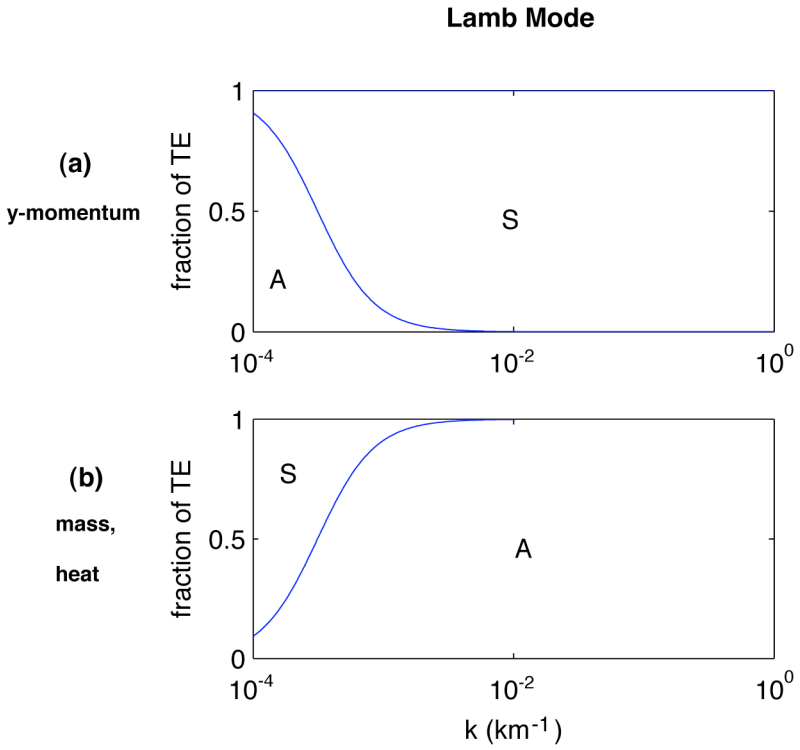

Figure 4.7: Partitioning of the total energy of the Lamb mode ($m = i\ell$) among steady (S) and acoustic-wave (A) classes for injections of (a) y-momentum, and (b) mass and heat that project equally onto all horizontal modes. Injection of x- and z- momentum generates only an acoustic-wave class in the Lamb mode.

4.5 Energetics of PV-Equivalent Injections

Section 4.2 presented the conservation of PV and sections 4.3 and 4.4 presented the energy partitioning for the hydrostatic and geostrophic adjustment problem. This section considers the energy partitioning for localized injections of heat, mass, and y-velocity that generate equivalent distributions of PV. Such injections generate adjustment processes that asymptote toward identical steady states and therefore comprise an interesting set of cases for comparison. While holding the steady state constant among

cases under examination, we are able to identify some basic similarities and differences in the nature of the transient response to injections of different type.

The injection function projects preferentially onto the spatial modes according to its geometry. Each of these modes may be separated into the classes of time dependencies, as in (4.13). After summing over all of the modes, we may separate the resulting "total" energy into the total of each class. Such is the partitioning presented here.

We first consider an injection of heat of the form,

$$\dot{\theta} = \theta_0 \left[\cos^2(z_\theta) H^*(z, d_g, d_g + d) \right] \left[\frac{1}{1 + \left(\frac{x}{a}\right)^2} \right] \left[\frac{H^*(t, 0, \tau)}{\tau} \right] , \tag{4.21}$$

where $z_\theta = \pi (z - d_g - d/2)/d$, $H^*(x, x_1, x_2) = H(x - x_1) - H(x - x_2)$ and H is the Heaviside step function. The mass-injection that generates an equivalent PV distribution is given by

$$\begin{aligned} \dot{q} = \theta_0 \left[\left(\frac{2 \pi H_s}{\pi d} \right) \sin(z_\theta) \cos(z_\theta) + \left(\frac{\pi}{\tau} + 1 \right) \cos^2(z_\theta) \right] H^*(z, d_g, d_g + d) \\ \cdot \left[\frac{1}{1 + \left(\frac{x}{a}\right)^2} \right] \left[\frac{H^*(t, 0, \tau)}{\tau} \right] , \end{aligned} \tag{4.22}$$

where $\theta_0 = \dot{q}_s \tau / \rho_s$. For the following presentation, the injection is of width $a = 25$ *km*, depth $d = 9$ *km*, and elevation $d_g = 1$ *km*. Figure 4.8a plots the geometry of the potential vorticity anomaly induced by (4.21-4.22). The vertical dipole is similar to but smoother than the distribution chosen in Chagnon and Bannon (2001).

Figure 4.9 presents the energy partitioning as a function of duration τ. The steady-state response to an injection of heat as in Fig. 4.9a is equivalent to that generated by the mass source/sink dipole in Fig. 4.9b. The energy partitioning for these PV-equivalent injections is quite different for short duration. When $\tau < 10^2$ *s* - the

Figure 4.8

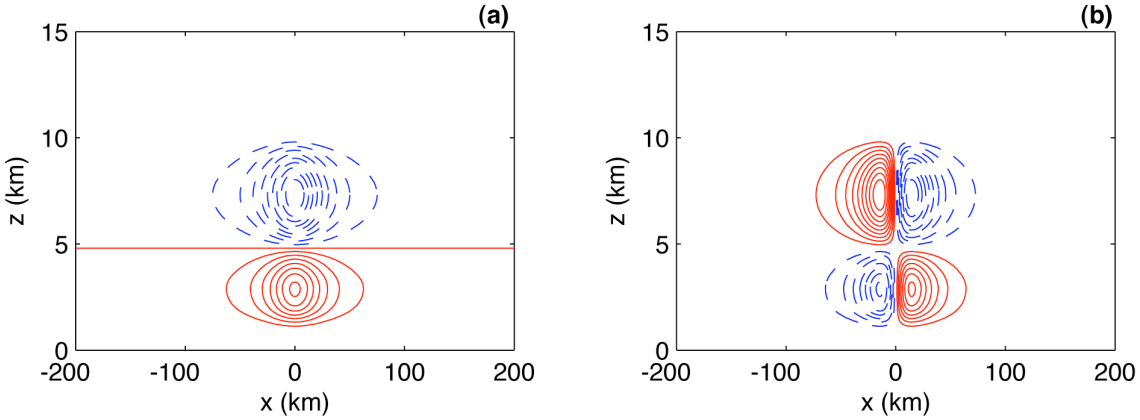

Figure 4.8: Geometry of the potential vorticity perturbation generated in (a) by either an injection of heat (4.21) or mass (4.22) and in (b) by either an injection of heat (4.23) or y-momentum (4.24).

approximate duration of acoustic wave attrition - the response to a mass injection is dominated by acoustic waves for the reasons described in section 4.4b. If we assume that injections of short and long duration generate the same steady state, then the energy associated with a short duration injection is much larger than that associated with a long duration injection because the fraction of energy in the steady is state is much smaller for a short duration injection. For example, the instantaneous injection of heat produces approximately 5.8 times the total energy of a 10,000 second injection. In addition, the total energy of a short duration mass injection is much larger than that of an equivalent heat injection of similar duration. For example, an instantaneous injection of mass produces approximately 33.2 times the total energy of an injection of heat. For longer duration injection $\Delta > 10^2\ s$, the energy partitioning is very similar between the two cases. On such time scales the waves that are not filtered by (4.14) are responsible primarily for achieving a horizontal (geostrophic) adjustment, which is largely insensitive to the manner by which the PV has been introduced.

Next we compare PV-equivalent heat and *y*-momentum injections. Consider a heating of the form

$$\dot{\theta} = \theta_0 \left[\cos^2(z\pi)\, H^*(z, d_g, d_g + d)\right]\left[\frac{2x/a}{\left(1 + \left(\frac{x}{a}\right)^2\right)^2}\right]\left[\frac{H^*(t,0,\Delta)}{\Delta}\right], \tag{4.23}$$

and the PV-equivalent injection of *y*-momentum,

$$\dot{v} = \Delta v \left[\left(\frac{2\pi H_s}{\pi d}\right)\sin(z\pi)\cos(z\pi) + \left(\frac{\pi + 1}{\pi}\right)\cos^2(z\pi)\right] H^*(z, d_g, d_g + d) \left[\frac{1}{\left(1 + \left(\frac{x}{a}\right)^2\right)}\right]\left[\frac{H^*(t,0,\Delta)}{\Delta}\right], \tag{4.24}$$

Figure 4.9

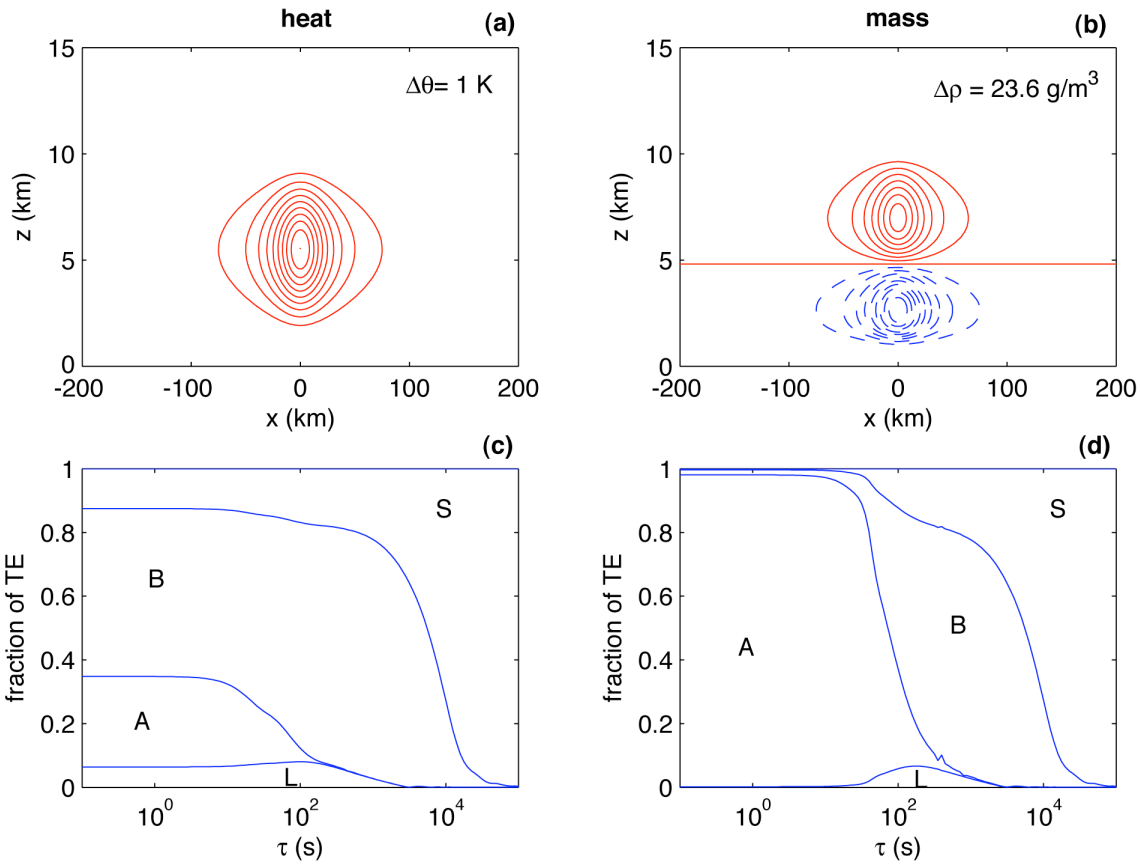

Figure 4.9: Potential-vorticity-equivalent injections of (a) heat and (b) mass and their corresponding total energy partitioning (c), (d) as a function of injection duration τ. Either injection produces the dipole potential vorticity distribution of Fig.4.8a. Hereafter, the time-dependent classes contributing to the total energy (which is summed over all spatial modes) are denoted acoustic wave (A), buoyancy wave (B), steady state (S), and Lamb wave (L).

where $\Delta v = f a \Delta\Delta / \Delta_s$. The PV distribution associated with these injections, shown in Fig. 4.8b, is quadrupolar (i.e. dipoles in both the vertical and horizontal directions).

Figure 4.10 presents the energy partitioning as a function of duration Δ. The steady-state response to an injection of heat with dipole structure in the horizontal (Fig. 4.10a) is the same as that generated by a *y*-momentum injection that is monopolar in the horizontal but dipolar in the vertical (Fig. 4.10b). Qualitatively, the thermally direct circulation developing from such heating in Fig. 4.10a may be expected to generate a *y*-momentum field similar to that in Fig. 4.10b. Because the time-scale associated with the latter injection is, in reality, much longer than that associated with the heating, the transient response to these PV-equivalent injections is expected to be quite different on shorter time scales. Indeed, for all but the longest duration $\Delta > 10^4$ *s*, the energy partitioning is very different. The response to the *y*-momentum injection involves only the PV-conserving contribution and the low frequency inertia-gravity waves. Such transients primarily accomplish a horizontal (geostrophic) adjustment. The response to a heating is likely to involve a vertical adjustment by acoustic and nonhydrostatic buoyancy waves, as was presented in part chapter 3. Because the steady-state generated by these two injections is identical but the fraction of energy residing in the steady state differs, the injection of heat generates a more energetic transient response than the PV-equivalent *y*-momentum injection. For example, an instantaneous injection of heat produces approximately 290 times the total energy of an injection of *y*-momentum. A heat injection of duration 1000 seconds produces approximately 84.5 times the total energy of the *y*-momentum injection, whereas a duration of 10,000 seconds produces

Figure 4.10

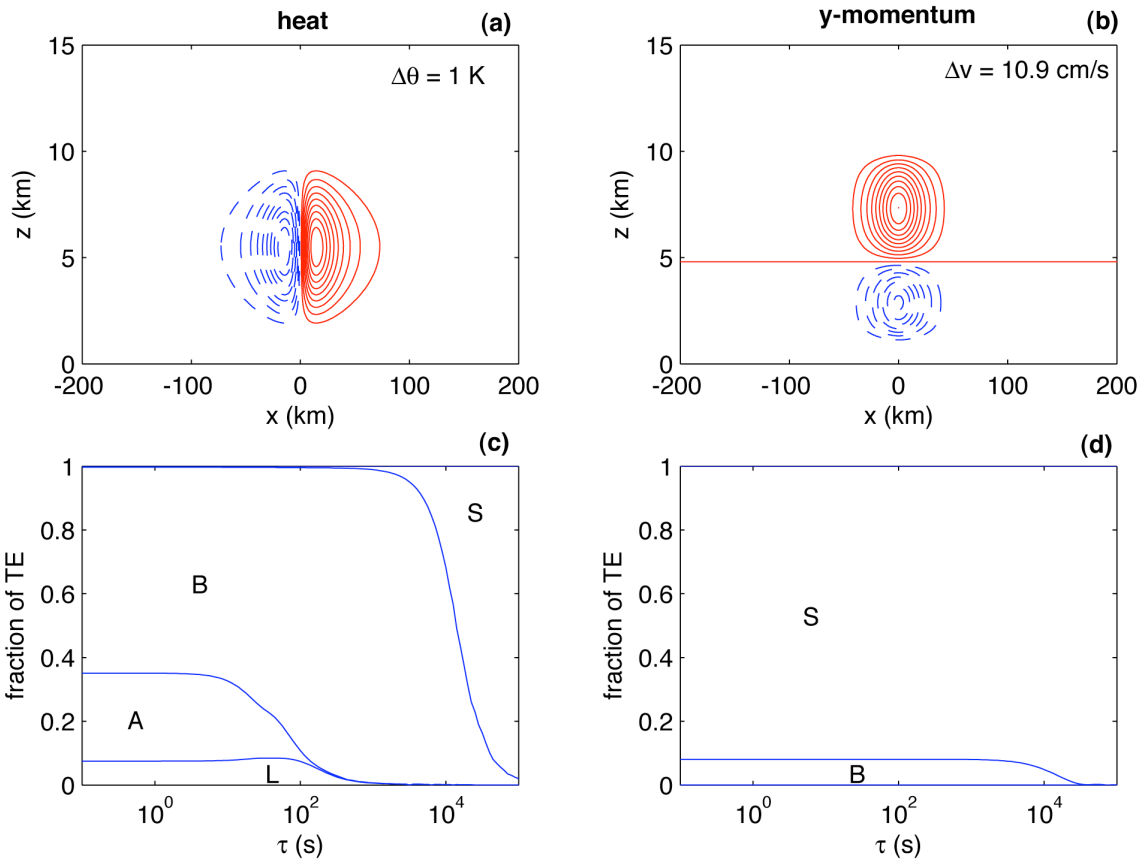

Figure 4.10: Potential-vorticity-equivalent injections of (a) heat and (b) *y*-momentum and their corresponding total energy partitioning (c), (d) as a function of injection duration τ. Either injection produces the quadrupole potential vorticity distribution of Fig.8b.

approximately 2.98 times the total energy and a duration of 100,000 seconds produces approximately no difference.

Another set of PV-equivalent injections that generate very different transient responses are those with identical spatial structure, origin and time-integrated amplitude but of different temporal dependence. For example consider the set of heat injections of the form (4.21) with fixed depth $d = 9\ km$, and elevation $d_g = 1\ km$, of varying duration τ but whose horizontal geometry projects equally onto all horizontal modes (i.e. horizontal white noise). Such heatings generate equivalent distributions of PV independent of τ. Varying τ, however, strongly impacts the characteristics of the energy spectrum. Figure 4.11 presents the horizontal white noise spectra for durations ranging from one minute to six hours. The PV of a given horizontal structure k is identical in each of the cases. The filtering function (4.14) preferentially removes the highest frequency waves, such that acoustic waves are generated only by injections of duration of several minutes or less. The high frequency buoyancy waves, which are of narrowest horizontal scale, are preferentially filtered such that waves of scale less than 10 km are not significantly generated by a heat injection of one hour duration. Similarly, the narrowest horizontal scale Lamb waves are preferentially filtered such that waves of scale less than 100 km are not significantly generated by heating of one hour duration.

Figure 4.11

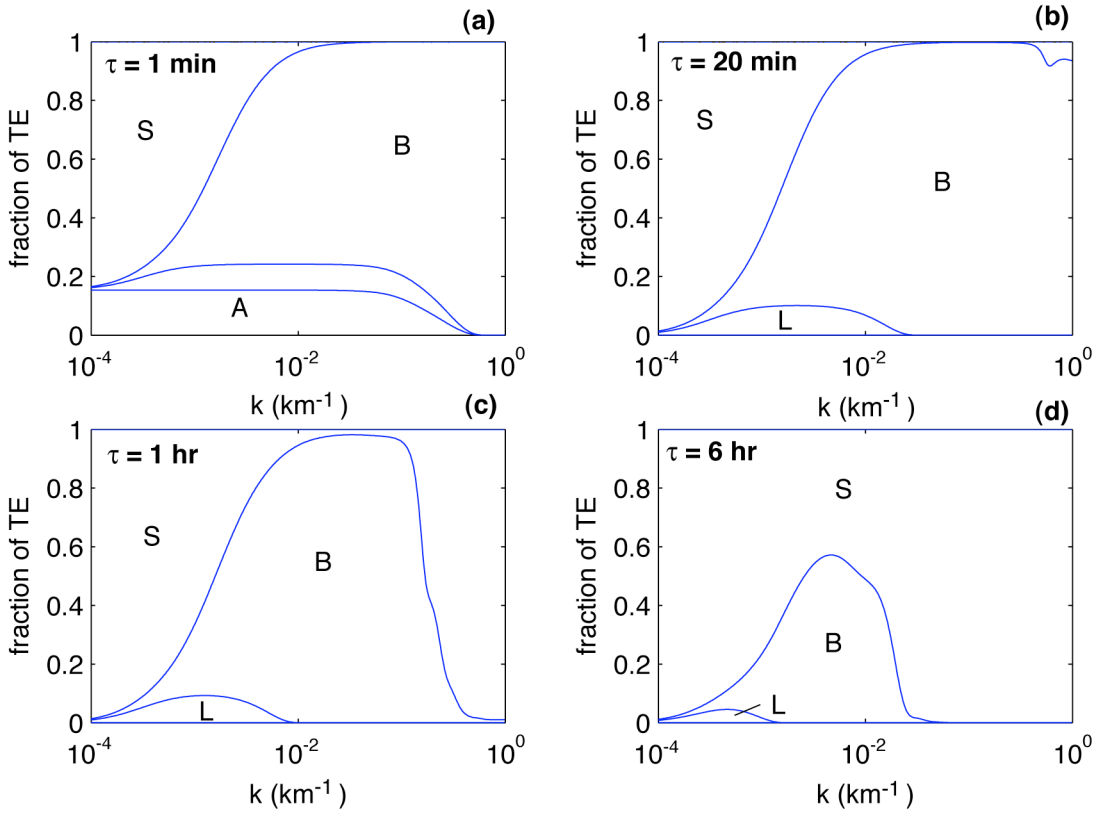

Figure 4.11: Partitioning of the total energy (summed over all vertical modes) among the time-dependent classes following an injection of heat of duration (a) 1 minute, (b) 20 minutes, (c) 1 hour, and (d) 6 hours that projects equally onto all horizontal modes and is 9 km deep and elevated 1 km above ground.

4.6 Summary

Chapters 2 and 3 presented an analytic solution to a hydrostatic and geostrophic adjustment problem. The model was constructed under the assumption that hydrostatic and geostrophic imbalance may be generated rapidly and on small scales by such phenomena as convection, and that the response to these disturbances by the larger-scale environment is approximately linear. This notion has formed the basis for many investigations into the relationship between the source and wave spectrum as well as the function of waves in the adjustment process. The advantage of the present study is its generality; it considers adjustment of a fully compressible atmosphere with a rigid lower boundary to injections of various spatial and temporal scale and type. Chapter 4 exploits a useful tool - the energy partitioning - to explore the vast parameter space associated with the wave source. Additionally, the consideration of potential vorticity in the context of energy partitioning clarifies some interesting relationships between adjustment processes that asymptote toward identical steady states.

Depending on the type of the imbalance generation mechanism in the governing equations (i.e. whether the imbalance is introduced via a prescribed injection of heat, mass or momentum), the characteristics of the wave spectrum may be very different. For example, we have demonstrated that nonhydrostatic buoyancy waves dominate the wave spectrum at narrow horizontal scales when the injection is a rapid one of vertical momentum. Lane et al (2001) were able to diagnose this same behavior in an anelastic numerical simulation of convection. The present analysis demonstrates that the potential

for the updraft to generate these buoyancy waves is largest for the deepest updrafts. A rapid, deep injection of heat is also capable of generating these waves efficiently.

Wider, hydrostatic, rotating buoyancy waves are efficiently generated by the injection of non-divergent horizontal momentum with vorticity. Such injections constitute the imbalance generation mechanism of the classic Rossby adjustment problem. Strictly, the classic Rossby adjustment problem is analogous to the injection of *y*-momentum of the present problem. The injection of a divergent horizontal current generates a response in the along current direction. Such an injection therefore does not efficiently generate nonhydrostatic buoyancy waves whose group velocity is mainly directed vertically. However, if introduced rapidly and on small scales, such an injection efficiently generates horizontally propagating acoustic waves.

The rapid injection (or rapid redistribution) of mass is a very efficient generator of acoustic waves. The large pressure perturbations associated with such injections are directly removed by the acoustic waves. Similarly, a rapid heating generates a large pressure perturbation to which acoustic waves may respond. The significance of these sources in nature is much less than what one may conclude from the examination of the temporal Green's function energy spectra presented in section 4.4. A restriction is placed on the ability of any injection to generate particular waves: the duration of the injection must be less than or equal to the period of the waves. Vadas and Fritts (2001) presented a similar conclusion with respect to Boussinesq buoyancy waves generated by time-dependent sources of momentum and heat. Sotack and Bannon (1999) conclude that acoustic waves are not generated significantly by heating of duration exceeding two minutes.

In nature, the injections that generate imbalance have characteristic time, length, and depth scales that are not mutually independent. The issue of the *origin* of the injection function determines these qualities. The analysis presented in this thesis is not suited to address this issue of origin. However, we can safely speculate about some qualities of the imbalance origin. For example, the rapid redistribution of mass associated with a convective updraft is not generated instantly but in an amount of time related to the depth and speed of the updraft. For smaller turbulent eddies within a cloud, this time-scale may be small enough to constitute a source of acoustic waves. However, for the largest scales within the cloud, the redistribution of mass is too slow to generate acoustic waves. The heating associated with phase changes occurs on very small spatial and short time scales. However, the organization of this heating into finite regions within the cloud is accomplished by the convecting updrafts. Thus, the ability of heating to generate coherent acoustic signals from finite regions within the cloud is limited by the local convective time scales. It is therefore expected that the acoustic signal emerging from a cloud is only as coherent as the turbulent convective regions in which the waves are generated.

The generation of acoustic waves is not the only potential consequence of compressibility. The presence of a lower boundary restricts the ability of the perturbed region to expand/contract in the vicinity of the boundary. Consequently, a Lamb wave may propagate horizontally along the lower boundary when the injection induces expansion near that boundary. Unlike internal acoustic waves, the Lamb waves may be generated by injection of longer duration, as Nicholls et al (2000) have observed during the numerical simulation of convection. Because the frequency of these waves decreases

with increasing horizontal scale, a slow but wide convective cluster may generate a Lamb wave signal.

Injections that have identical spatial structure but are applied slowly so as to not generate acoustic waves must still be accompanied by the same net expansion or compression required by the given total input of potential vorticity. Chagnon and Bannon (2001) investigate the properties of the steady state corresponding to localized heating of a compressible atmosphere. The current study emphasizes that the manner by which the steady state is achieved depends strongly on the manner by which the potential vorticity is introduced. This principle applies to the required generation of both buoyancy and acoustic waves. The interpretation of this is simple: A very rapid injection generates a severely unbalanced initial configuration. Such an unbalanced configuration requires the production of a large amount of wave energy in order to accomplish the adjustment. A injection that is more gradual generates a less severely unbalanced configuration requiring much less wave energy to accomplish the adjustment. From the perspective of the surrounding environment, the transient response to these injections is quite different. If a heating is applied slowly enough such that acoustic waves and nonhydrostatic buoyancy waves are not excited, then the air located above the heating will experience a slow vertical displacement toward an equilibrium position rather than oscillations about the equilibrium position.

Whether it is most appropriate to model the imbalance associated with a region of convection as a heating or mass redistribution is ambiguous and returns us to the issue of imbalance origin, the discussion of which is admittedly speculative. In reality, convection can accomplish all of these injections and the process of convective adjustment has thus

been modeled as a response to both heat and mass injection. In a Boussinesq model, Shutts (1994) argues that the transient response to these injections should be precisely equivalent. A comparison of injections that generate equivalent distributions of potential vorticity provides insight into the compatibility of these studies. The potential vorticity associated with a warmed column of air is equivalent to that generated by a vertical mass source/sink dipole. However, a very rapid injection of mass generates a much larger acoustic response than does the heating. If the duration of the injection exceeds several minutes, then the response to the PV-equivalent heating and mass injections are very similar. It is therefore essential to carefully consider the time-scale associated with the injection. For example, an instantaneous redistribution of mass on the cloud scale is physically absurd.

The results of the current study may be used to comment on the notion that the response to a given injection and the "averaged" injection are in some sense equivalent or asymptotic. The steady state corresponding to the PV introduced by a given injection is independent of the temporal characteristics of the injection. Furthermore, if we define a reasonable spatial averaging operator, then it may be shown that the spatially averaged steady-state response to a given injection is equivalent to the steady-state response to the spatially averaged injection; that is, these averaging operators commute between the injection and steady state. These properties do not hold for the transient response. We have demonstrated that by "averaging" the temporal structure of a given injection we will preferentially filter high frequency waves; by spatially averaging a given injection we project less energy onto finer scale structures. As Holton et al (2002) have argued, the mutual dependence of the spatial and temporal characteristics of the transients

complicates matters. A temporal averaging operator acts, in some sense, as a spatial averaging operator, and vice versa. For applications in which the nature of the transients is of primary concern, these matters must be taken into consideration.

Chapter 5

Conclusion

5.1 Contribution

The analysis presented in this thesis addresses some basic theoretical aspects of hydrostatic and geostrophic adjustment. Section 1.2 summarizes the historical precedent for this work. Beginning with the seminal work of Rossby (1937, 1938), Obukhov (1949), and Lamb (1932), followed by the general reviews of Blumen (1972) and Gill (1982) up to contemporary investigation of convective adjustment and gravity wave generation, it has been well established that the adjustment of a geophysical fluid to sources of hydrostatic and geostrophic imbalance is accomplished by inertia-buoyancy waves; In a compressible atmosphere, acoustic and Lamb waves may also take part in the adjustment. The interest in this process is often motivated by a desire to characterize the wave spectrum, which may be relevant to another process (e.g. wave drag in the stratosphere or the generation and organization of convection) or may be the subject of a parameterization in a numerical model.

Most investigations prescribe some initial disturbance to which the numerical or analytic model atmosphere must respond. This approach limits the capacity to analyze the relationship between the source and wave spectrum that is a central issue of this thesis. The spatial-temporal detail, type, and origin of the imbalance generation mechanism may take a wide variety of forms in the atmosphere. For example, consider an imbalance in

the synoptic-scale environment whose origin is a cluster of convection. Associated with this convection may be heating due to phase changes, a rapid redistribution of the mass field, and accelerations associated with the release of instability, all of which are realized as "injections" of heat, mass, or momentum into the larger-scale environment. Furthermore, these injections occur over a range of spatial and temporal scales. In reality, the characteristics of the wave source may therefore be quite complicated. Until recently, the parameter space of the imbalance generation mechanism has not been explored in detail. Vadas and Fritts (2001) began examining this parameter space in a vertically-infinite, linear Boussinesq model atmosphere. Holton et al (2002) warned that the analysis is complicated by the fact that the spatial and temporal characteristics of the waves are mutually dependent (i.e. via a dispersion relation).

This thesis improves the existing theory by providing a general picture of the relationship between the source and the wave spectrum in a fully compressible, semi-infinite model atmosphere. This relationship is demonstrated via the transient characteristics of the response (chapter 3) as well as the potential vorticity conservation and energy partitioning (chapter 4). The results extend the notion advanced by Vadas and Fritts (2001) that the excitation of particular waves is restricted by the period of the wave relative to the duration of the injection. Furthermore, the results indicate that the type of injection strongly affects the characteristics of the response. For example, an injection of vertical velocity is a very efficient generator of nonhydrostatic buoyancy waves *provided* the geometry and duration of the injection allow their generation. A useful way to contrast the response to injections of different type is to concoct injections that generate equivalent distributions of potential vorticity. Such injections must generate

responses that asymptote to the same hydrostatic and geostrophic state. The ways in which the transient responses differ (presented in section 4.5) emphasizes the sensitivity to the nature of the injection.

Finally, a significant contribution of this thesis is its treatment of compressible dynamics. The previous work on the hydrostatic adjustment by acoustic waves (e.g. Bannon 1995, Sotack and Bannon 1999, Duffy, 2003) was restricted to a horizontally homogeneous atmosphere. Chagnon and Bannon (2001) presented the steady state in an atmosphere with horizontal dependence, but did not include the transient solution. The solutions presented here elaborate on this previous work by demonstrating the transient dynamics in fully compressible, horizontally varying atmosphere. Appendix C provides another elaboration on the problem of acoustic adjustment. Here, Bannon's (1995) solution of Lamb's problem is generalized to a moist atmosphere subject to injections of heat, mass, and moisture of arbitrary vertical structure. It is shown that the steady state is sensitively dependent on the vertical structure of the injection and that a moisture injection induces a response that incorporates some features of the response to both mass and heat injection.

5.2 Practical Implications

Acoustic waves present a challenge to designers of numerical models of the atmosphere. The time-scale of acoustic waves is several orders of magnitude shorter than the next fastest motions supported by the atmosphere (e.g. see Fig. 2.2). Consequently, the existence of these waves places a severe restriction on the time step and resolution of

stable finite-difference schemes (e.g. Durran 1999, chapter 2). The additional cost of the increased computation time has led many designers to seek alternatives such as sound-proof equations and time-splitting techniques. Unfortunately, the approximations introduced by these alternatives are a potential source of error. Recent advancements in computing methods and resources have made the integration of fully compressible models more practical (e.g. Bryan and Fritsch 2002). In order to test the accuracy of these models in simulating compressible flow, an analytic benchmark is required. The solutions presented in this thesis could provide such a benchmark for fully compressible numerical models. Furthermore, it is generally assumed that a fully compressible model is better than an anelastic one. This may be the case sometimes, but is it always? How much of a practical advantage is gained by using a fully compressible model rather than an anelastic one? In this manner, the solutions presented in this thesis may also provide a benchmark for anelastic models. Appendix D provides an analytic framework for a comparison between fully compressible and anelastic models.

Another practical issue in numerical modeling is subgridscale parameterization. Processes that occur on temporal and spatial scales shorter and smaller than those explicitly resolved by the model must be represented in some artificial but dependable manner. In order to design effective parameterizations, some general relationship between the small scale process and the larger, grid-resolved processes must be assumed. The analytic solutions presented in this thesis may provide some insight into the design of such parameterizations. For example, it is well known that gravity waves generated in the troposphere play an important role in the dynamics of the stratosphere (see Kim et al. 2003 for a review). The sources that give rise to these gravity waves are often too fine to

be resolved by global circulation models. The successful parameterization of wave drag and secondary generation requires a description of the source spectrum. The solutions presented in this thesis may provide some insight into these issues.

5.3 Shortcomings

In spite of the contributions to theory made by this thesis and the potential applications thereof, there are several ways in which the analysis could be extended and improved. As a conclusion to this thesis, it is appropriate to consider some of these shortcomings and suggest improvements for future investigation.

The resting isothermal basic state prescribed in the model of chapter 2 is not generally applicable to the real atmosphere. This choice simplifies the analysis, but has the unrealistic property that wave velocity is independent of height. In reality, the vertical temperature profile may be such that waves are refracted and potentially trapped within ducts. These features may significantly affect the qualities of the transient solution presented in chapter 3. A solution similar to the one presented here but against a nonisothermal basic state would improve the practical value of the analysis. Duffy (2003) performed such an analysis of the vertical hydrostatic adjustment and observed the same qualitative behavior as in the isothermal case. However, when applied in a context as general as the one in this thesis, such changes to the basic state profile significantly increase the difficulty of the problem.

In this thesis, the origin of the initial imbalance is not addressed. We assume the details of this imbalance are arbitrary quantities that may be specified by the user.

Furthermore, we do not address the possibility that the waves generated by the imbalance may interact with and influence the very mechanism that gave rise to the waves. This nonlinear relationship between the waves and the source may be essential to describing the evolution and organization of cloud systems (e.g. Lindzen 1975. Raymond 1976).

Bibliography

Arfken, G., 1970: *Mathematical Methods for Physicists*. Academic Press, 815 pp.

Bannon, P. R., 1995: Hydrostatic adjustment: Lamb's problem. *J. Atmos. Sci.,* **52,** 1743-1752.

Blumen, W., 1972: Geostrophic adjustment. *Rev. Geophys. Space Phys.,* **10,** 485-528.

□□□, and R. Wu, 1995a: Geostrophic adjustment: frontogenesis and energy conversion. *J. Phys. Oceanogr.,* **25,** 428-438.

□□□ 1995b: Geostrophic adjustment of a zero potential vorticity flow initiated by a mass imbalance. *J. Phys. Oceanogr.,* **25,** 439-445.

Bolin, B., 1953: The adjustment of a non-balanced velocity field towards geostrophic equilibrium in a stratified fluid. *Tellus,* **5,** 373-385.

Bretherton, C., 1988: Group velocity and the linear response of stratified fluids to internal heat or mass sources. *J. Atmos. Sci.,* **45,** 81-93.

□□□ and P. K. Smolarkiewicz, 1989: Gravity waves, compensating subsidence and detrainment around cumulus clouds. *J. Atmos. Sci.,* **46**, 740-759.

Bryan, G. H., and J. M. Fritsch, 2002: A benchmark simulation for moist nonhydrostatic numerical models. *Mon. Wea. Rev.,* **130,** 2917-2928.

Cahn , Jr., A., 1945: An investigation of the free oscillations of a simple current system. *J. Meteor.,* **2,** 113-119.

Chagnon, J. M., and P. R. Bannon, 2001: Hydrostatic and geostrophic adjustment in a compressible atmosphere: Initial response and final equilibrium to an instantaneous localized heating. *J. Atmos. Sci.,* **58,** 3776-3792.

Csanady, G. T., 1971: On the equilibrium shape of the thermocline in a shore zone. *J. Phys. Oceanogr.,* **1,** 263-270.

Cole, J. D., and C. Greifinger, 1969: Acoustic-gravity waves from an energy source at the ground in an isothermal atmosphere. *J. Geophys. Res.,* **74,** 3693-3703.

Dikiy, L. A., 1969: A variational principle in the theory of meteorological-field adaptation. *(Izv.) Atmos. and Oceanic Phys.,* **5,** 188-191, translated by J. Findlay.

Duffy, D. G., 2003: Hydrostatic adjustment of nonisothermal atmospheres. *J. Atmos. Sci.,* **60,** 339-353.

Durran, D. R., 1999: *Numerical Methods of Wave Equations in Geophysical Fluid Dynamics*. Springer-Verlag New York, 465 pp.

Eckart, C., 1960: *Hydrodynamics of Oceans and Atmospheres*. Pergamon Press, 290pp.

Gill, A. E., 1982: *Atmosphere-Ocean Dynamics*. Academic Press, 662pp.

Glendening, J. W., 1993: Nonlinear displacement of the geostrophic velocity jet created my mass imbalance. *J. Atmos. Sci.,* **50,** 1617-1628.

Fritts, D. C., and L. Yuan, 1989: An analysis of gravity wave ducting in the atmosphere: Eckart's resonances in thermal and Doppler ducts. *J. Geophys. Res.,* **94,** 455-466.

Held, I. M., 1985: Pseudomomentum and orthogonality of modes in shear flows. *J. Atmos. Sci.,* **42,** 2280-2288.

Holton, J. R., 1983: The influence of gravity wave breaking on the general circulation of the middle atmosphere. *J. Atmos. Sci.,* **40,** 2497-2507.

------- ,J. H. Beers, and X. Zhou, 2002: On the vertical scale of gravity waves excited by localized thermal injection. *J. Atmos. Sci.,* **59,** 2019-2023.

Iga, K., 2001: Transition modes in stratified compressible fluids. *Fluid Dyn. Res.,* **28,** 465-486.

Kalashnik, M.M., 2000: Hydrostatic adjustment theory. *Investiya Atmos. Ocean. Phys.,* **30,** 203-209.

Kim, Y.-.J., S. D. Eckermann, and H.-Y. Chen: 2003: An overview of the past, present, and future of gravity-wave parameterization for numerical climate and weather prediction models. *Atmos.-Ocean.* **41**. 65-98.

Lamb, H., 1932: *Hydrodynamics*. Dover, 738 pp.

Lane, T. P, and M. J. Reeder, 2001: Convectively generated gravity waves and their effect on the cloud environment. *J. Atmos. Sci,* **58,** .

----------, ----------, and T. L. Clark, 2001: Numerical modeling of gravity wave generation by deep tropical convection. *J. Atmos. Sci,* **58,** 1249-1274.

Lighthill, J. 1978: *Waves in Fluids*. Cambridge University Press, 504 pp.

Lin, Y. L., and R. B. Smith, 1986: Transient dynamics of airflow near a local heat source. *J. Atmos. Sci.,* **43,** 40-49.

Lindzen, R. S., 1974: Wave-CISK in the tropics. . *J. Atmos. Sci.,* **31,** 156-179.

McDonald, N. R., 1990: Far-field flow forced by the entrainment of a convective plane plume in a rotating stratified fluid. *J. Phys. Oceanogr.,* **20,** 1791-1798.

Nicholls, M. E., Pielke, R. A., and W. R. Cotton, 1991: Thermally forced gravity waves in an atmosphere at rest. *J. Atmos. Sci.,* **48,** 1869-1884.

□ □ □ and □ □ □ , 1994a: Thermal compression waves. I: Total energy transfer. *Quart. J. Roy. Meteor. Soc.,* **120,** 305-332.

□ □ □ and □ □ □ , 1994b: Thermal compression waves. II: Mass adjustment and vertical transfer of total energy. *Quart. J. Roy. Meteor. Soc.,* **120,** 333-359.

□ □ □ and □ □ □ , 2000: Thermally induced compression waves and gravity waves generated by convective storms. *J. Atmos. Sci.,* **57,** 3251-3271.

Obukhov, A. M., 1949: On the question of geostrophic wind. *Bulletin of the USSR Academy of Sciences,* **13,** 281-306. (translated to English from Russian by J. G. Howcroft)

Ou, H. W., 1983: Some two-layer models of the shelf-slope front. : Geostrophic adjustment and its maintenance. *J. Phys. Oceanogr.,* **13,** 1798-1808.

□ □ □ , 1984: Geostrophic adjustment. : A mechanism for frontogenesis. *J. Phys. Oceanogr.,* **14,** 994-1000.

Pierce, A. D., 1963: Propagation of acoustic-gravity waves from a small source above the ground in an isothermal atmosphere. *J. Acoustical. Soc. of Amer.,* **35,** 1798-1807.

Raymond, D. J., 1976: Wave-CISK and convective mesosystems. *J. Atmos. Sci.,* **33,** 2392-2398.

□ □ □ , 1986: Prescribed heating of a stratified atmosphere as a model for moist convection. *J. Atmos. Sci.,* **43,** 1101-1111.

Rossby, C.-G., 1937: On the mutual adjustment of pressure and velocity distribution in simple current systems, 1. *J. Mar. Res.,* **1,** 15-18.

□ □ □, 1938: On the mutual adjustment of pressure and velocity distribution in simple current systems, 2. *J. Mar. Res.,* **1,** 239-263.

Schubert, W. H., J. H. Hack, P. L. Silva Dias, and S. R. Fulton, 1980: Geostrophic adjustment in an axisymmetric vortex. *J. Atmos. Sci,* **37,** 1464-1484.

Shutts, G., 1994: The adjustment of a rotating, stratified fluid to localized sources of mass. *Quart. J. Roy. Meteor. Soc.,* **120,** 361-386.

Sotack, T., and P. R. Bannon, 1999: Lamb's hydrostatic adjustment for heating of finite duration. *J. Atmos. Sci.,* **56,** 71-81.

Tjim, A. B. C., and A. J. Van Delden, 1999: The role of sound waves in sea-breeze initiation. *Quart. J. Roy. Meteor. Soc.,* **125,** 1997-2018.

Vadas, S. L., and D. C. Fritts, 2001: Gravity wave radiation and mean responses to local body forces in the atmosphere. *J. Atmos. Sci.,* **58,** 2249-2279.

Veronis, G., 1956: Partitioning of energy between geostrophic and non-geostrophic oceanic motions., *Deep Sea Res.,* **3,** 157-177.

Appendix A

Coefficients of the Temporal Green's Function

Section 2.3 generalizes the forced solutions in terms of a temporal Green's function. The Green's function is of the form $\widehat{\underset{\sim}{\square}}_{\mathbf{n}} = \underset{\approx}{\mathbf{E}}_{\mathbf{n}} \underset{\sim}{\square}_{\mathbf{n}}$ where the eigenvector matrix $\underset{\approx}{\mathbf{E}}_{\mathbf{n}}$ and the vector of time dependencies $\underset{\sim}{\square}_{\mathbf{n}}$ are provided in (2.19). Conditions on the coefficients C_i of the temporal Green's function are given by (2.24), which may be written as the linear algebraic system $\underset{\approx}{\mathbf{E}}_{\mathbf{n}}\, \underset{\sim}{\mathbf{C}}_{\mathbf{n}} = \underset{\sim}{\mathbf{F}}^{\mathbf{o}}_{\mathbf{n}}$ where the i-th element of $\underset{\sim}{\mathbf{C}}_{\mathbf{n}}$ is C_i and the i-th element of $\underset{\sim}{\mathbf{F}}^{\mathbf{o}}_{\mathbf{n}}$ is $F^o{}_i = \square_k s_{\square i}$. For example $F^o{}_1 = \square_k s_{U,n}$. Solving for the coefficients involves inverting $\underset{\approx}{\mathbf{E}}_{\mathbf{n}}$, the result of which is complicated and not obviously meaningful. Rather than explicitly provide $\underset{\approx}{\mathbf{E}}^{-1}_{\mathbf{n}}$, we provide only the explicit solution for the coefficients C_i:

$$C_1 = \frac{g f}{\square_a \square_b \square}\left[\begin{array}{c} F_2^o\,(B_{42} - B_{44}) + F_4^o\,(B_{24} - B_{22}) \\ + F_5^o\left(E_{21}(B_{42} - B_{44}) + E_{41}(B_{22} - B_{24}) + \dfrac{\square_a \square_b \square}{g f}\right) \end{array}\right], \qquad \text{(A1)}$$

$$C_3 = \frac{1}{2\square}\left[\begin{array}{c} F_1^o\,E_{34} + F_2^o \dfrac{g f}{\square_a \square_b} B_{44} - F_3^o\,E_{14} - F_4^o \dfrac{g f}{\square_a \square_b} B_{24} \\ + F_5^o \dfrac{g f}{\square_a \square_b}(B_{24}\,E_{41} - B_{44}\,E_{21}) \end{array}\right], \qquad \text{(A2)}$$

$$C_3 = \frac{1}{2\square}\left[\begin{array}{c} -F_1^o\,E_{34} + F_2^o \dfrac{g f}{\square_a \square_b} B_{44} + F_3^o\,E_{14} - F_4^o \dfrac{g f}{\square_a \square_b} B_{24} \\ + F_5^o \dfrac{g f}{\square_a \square_b}(B_{24}\,E_{41} - B_{44}\,E_{21}) \end{array}\right], \qquad \text{(A3)}$$

$$C_4 = \frac{1}{2\Delta}\left[\begin{array}{c} -F_1^o E_{32} - F_2^o \frac{gf}{\alpha_a \alpha_b} B_{42} + F_3^o E_{12} + F_4^o \frac{gf}{\alpha_a \alpha_b} B_{22} \\ + F_5^o \frac{gf}{\alpha_a \alpha_b}(B_{42} E_{21} - B_{22} E_{41}) \end{array}\right], \qquad \text{(A4)}$$

$$C_5 = \frac{1}{2\Delta}\left[\begin{array}{c} F_1^o E_{32} - F_2^o \frac{gf}{\alpha_a \alpha_b} B_{42} - F_3^o E_{12} + F_4^o \frac{gf}{\alpha_a \alpha_b} B_{22} \\ + F_5^o \frac{gf}{\alpha_a \alpha_b}(B_{42} E_{21} - B_{22} E_{41}) \end{array}\right], \qquad \text{(A5)}$$

where

$$\Delta = \frac{i k \alpha_a \alpha_b (N_s^2 - f^2)(\alpha_b^2 - \alpha_a^2)}{(N_s^2 - \alpha_a^2)(N_s^2 - \alpha_b^2)(f^2 - \alpha_a^2)(f^2 - \alpha_b^2)},$$

and $B_{22} = E_{22} - E_{21}$, $B_{24} = E_{24} - E_{21}$, $B_{42} = E_{42} - E_{41}$, and $B_{44} = E_{44} - E_{41}$.

Appendix B

Orthogonality of the Energetics

Section 4.3 presents the characteristics of the energy which, as we assert, may be partitioned distinctly among the orthogonal spatial modes which in turn may be partitioned distinctly among the acoustic-wave, buoyancy-wave, and PV-conserving time-dependent classes. This appendix proves these assertions by exploiting the qualities of the solution presented in part chapter 2.

It is convenient to recall the form of the linear system of partial differential equations,

$$\frac{\partial \underset{\sim}{\square}}{\partial t} + \underset{\approx}{\mathbf{A}}\,\underset{\sim}{\square} = \underset{\sim}{\mathbf{F}} \quad , \tag{2.4}$$

where the solution state vector is $\underset{\sim}{\square}^{\mathbf{T}} = (U, V, W, S, P)$, the injection vector is $\underset{\sim}{\mathbf{F}} = (\dot{U}, \dot{V}, \dot{W}, \dot{S}, \dot{P})$, and $\underset{\approx}{\mathbf{A}}$ is a spatial matrix operator. The energy density (4.8) may be written in terms of the solution vector $\underset{\sim}{\square}$:

$$TE = \frac{1}{2}\,\underset{\sim}{\square}^{*\mathbf{T}}\,\underset{\approx}{\mathbf{D}}\,\underset{\sim}{\square} \quad , \tag{B1}$$

where the diagonal matrix operator $\underset{\approx}{\mathbf{D}}$ is

$$\underset{\approx}{\mathbf{D}} = \begin{bmatrix} 1 & 0 & 0 & 0 & 0 \\ 0 & 1 & 0 & 0 & 0 \\ 0 & 0 & 1 & 0 & 0 \\ 0 & 0 & 0 & \frac{g^2}{N_s^2} & 0 \\ 0 & 0 & 0 & 0 & \frac{1}{c_s^2} \end{bmatrix}, \tag{B2}$$

and the sum of the conversion terms is zero,

$$\int_0^{2D} \int_{-} \underset{\sim}{\Phi}^{*\mathbf{T}} \underset{\approx}{\mathbf{D}} \underset{\approx}{\mathbf{A}} \underset{\sim}{\Phi} \, dx \, dz = 0. \tag{B3}$$

The energy is therefore governed by

$$\frac{\partial}{\partial t} \int_0^{2D} \int_{-} TE \, dx dz = \int_0^{2D} \int_{-} \underset{\sim}{\Phi}^{*\mathbf{T}} \underset{\approx}{\mathbf{D}} \underset{\sim}{\mathbf{F}} \, dx \, dz \quad . \tag{B4}$$

Because the spatial modes are orthogonal, we may consider the conservation of the spectral energy density (4.10):

$$TE_n = \frac{1}{2} \underset{\sim}{\Phi}_{\mathbf{n}}^{*\mathbf{T}} \underset{\approx}{\mathbf{D}}_{\mathbf{n}} \underset{\sim}{\Phi}_{\mathbf{n}} N_n \ , \tag{B5}$$

where N_n is the domain integral of the n-th vertical basis function squared

and

$$\underset{\approx}{\mathbf{D}}_{\mathbf{n}} =$$

$$\begin{bmatrix} 1 & 0 & 0 & 0 & 0 \\ 0 & 1 & 0 & 0 & 0 \\ 0 & 0 & (m^2 + \square^2) & 0 & 0 \\ 0 & 0 & 0 & \frac{g^2}{N_s^2}(m^2 + \square^2) & 0 \\ 0 & 0 & 0 & 0 & \frac{1}{c_s^2} \end{bmatrix} . \tag{B6}$$

First, let us consider solutions of the homogeneous problem of the form (2.19)

$\underset{\sim}{\square}_{\mathbf{n}} = \underset{\approx}{\mathbf{E}}_{\mathbf{n}} \underset{\sim}{\square}_{\mathbf{n}}$ where $\underset{\approx}{\mathbf{E}}_{\mathbf{n}}$ is the matrix of eigenvectors of $\underset{\approx}{\mathbf{A}}_{\mathbf{n}}$. The spectral energy density (B5) may be written as

$$TE_n = \frac{1}{2} \underset{\sim}{\square}_{\mathbf{n}}^{*\mathbf{T}} \underset{\approx}{\mathbf{M}}_{\mathbf{n}} \underset{\sim}{\square}_{\mathbf{n}} N_n \ . \tag{B7}$$

The elements of the wave interaction matrix $\underset{\approx}{\mathbf{M}}_{\mathbf{n}}$ are

$$\begin{aligned} M_{ij} = {} & E_{1i}^* E_{1j} + E_{2i}^* E_{2j} + (m^2 + \square^2) E_{3i}^* E_{3j} \\ & + \frac{g^2 (m^2 + \square^2)}{N_s^2} E_{4i}^* E_{4j} + E_{5i}^* E_{5j} \ . \end{aligned} \tag{B8}$$

Using the dispersion relation, it may be shown that $M_{ij} = 0$ when i is not equal to j . The wave interaction matrix $\underset{\approx}{\mathbf{M}}_{\mathbf{n}}$ is therefore diagonal, which implies that there is no interaction among the distinct time-dependent contributions to the energy. The diagonal elements of $\underset{\approx}{\mathbf{M}}_{\mathbf{n}}$ are

$$M_{ii} = \frac{1}{c_s^2} + \frac{k^2\left(\sigma_i^2 + f^2\right)}{\left(f^2 - \sigma_i^2\right)^2} + \frac{\left(m^2 + \beta^2\right)\left(\sigma_i^2 N_s^2\right)}{\left(N_s^2 - \sigma_i^2\right)^2} \quad . \tag{B9}$$

The spectral energy density may therefore be partitioned among the steady, acoustic, and buoyancy contributions as in (4.11), $TE_n = TE_n^{PV} + TE_n^a + TE_n^b$, where

$$\begin{aligned} TE_n^{PV} &= M_{11} C_1^* C_1 \ , \\ TE_n^a &= M_{22} C_2^* C_2 + M_{33} C_3^* C_3 \ , \\ TE_n^b &= M_{44} C_4^* C_4 + M_{55} C_5^* C_5 \ , \end{aligned} \tag{B10}$$

and the C_i are the coefficients of the PV-conserving, acoustic-wave, and buoyancy-wave contributions defined in (2.19). For solutions of the homogeneous problem, the distinct PV-conserving, acoustic-wave, and buoyancy-wave contributions to the energy are time-independent.

Next consider the energetics of solutions to the forced equation (2.4). Section 3 of chapter 2 demonstrated the structure of these solutions to be of the general form $\underset{\sim}{\eta}_{\mathbf{n}}(t) = \underset{\approx}{\mathbf{E}}_{\mathbf{n}} \underset{\sim}{\mathbf{G}}_{\mathbf{n}}(t)$ where the i-th element of $\underset{\sim}{\mathbf{G}}_{\mathbf{n}}$ is $G_i = c_i(t)\, exp(i\sigma_i t)$ with $c_i(t)$ defined in (2.25). Following the analysis of the energetics of the homogeneous solutions, we may also write the energy of the forced solution as

$$TE_n = \frac{1}{2} \underset{\sim}{\mathbf{G}}_{\mathbf{n}}^{*\mathbf{T}} \underset{\approx}{\mathbf{M}}_{\mathbf{n}} \underset{\sim}{\mathbf{G}}_{\mathbf{n}} N_n \ . \tag{B11}$$

The spectral energy density of the forced solutions may therefore be partitioned in a manner similar to that of the homogeneous solutions. The spectral energy density of the temporal Green's function, denoted in (4.12) as $\widehat{TE}_n = \widehat{TE}_n^{PV} + \widehat{TE}_n^a + \widehat{TE}_n^b$, is given by

$$\begin{aligned} \widehat{TE}_n^{PV} &= M_{11} C_1^* C_1 \ , \\ \widehat{TE}_n^{a} &= M_{22} C_2^* C_2 + M_{33} C_3^* C_3 \ , \\ \widehat{TE}_n^{b} &= M_{44} C_4^* C_4 + M_{55} C_5^* C_5 \ , \end{aligned} \tag{B12}$$

where the coefficients C_i are provided in (A1-A5). The representation (4.13) of time-dependent spectral energy density of the forced solution (B11) in terms of the spectral energy density of the Green's function and a filtering function $r(\square,t)$ follows directly from the relationship between the temporal Green's function and the general solution of the forced problem (2.22) given by (2.24) and (2.25).

Appendix C

Lamb's Hydrostatic Adjustment of a Moist Atmosphere

Lamb (1932) originally considered the vertical adjustment of a compressible atmosphere to localized sources of hydrostatic imbalance. Acoustic waves are generated in the region of localized imbalance and propagate into the surrounding environment. The displacements and net pressure change associated with the passage of the acoustic waves are exactly those required to adjust the column to hydrostatic balance.

Lamb's problem - in which the source of imbalance is a prescribed, infinitesimally deep harmonic oscillation - was reformulated by Bannon (1995) for a heating of finite depth wherein the acoustic waves are generated in regions of vertical heating gradient. The motivation for this design is the conceptualization of a cumulus cloud as a source of heating associated with phase changes within the cloud. Sotack and Bannon (1999) demonstrated that a heating must be applied very rapidly (time scale of less than 2 minutes) in order to generate a significant acoustic response. A finite-depth heating of the kind employed by Bannon (1995) is only capable of modeling the averaged or net cloud heating. The appropriate time scale of this net heating exceeds the critical duration of several minutes, and is probably an inappropriate model source of acoustic waves. The steady state however depends only on the time-integrated distribution of potential vorticity. The steady state response to the averaged injection may therefore be meaningful. Bannon (1995) only considered the steady state following a top-hat heating

of a dry atmosphere. This appendix addresses Lamb's problem in a moist atmosphere following injection of heat, mass, and moisture of arbitrary geometry.

The vertical adjustment of a moist atmosphere to injection of mass, heat, and momentum is studied via a horizontally homogeneous, compressible, moist set of equations in which the liquid and ice phases as well as the multi-velocity nature of the fluid are ignored. Linearizing the moist equations of Bannon (2002) about an isothermal, dry, resting atmosphere yields the equations governing the perturbations,

$$\frac{\partial w}{\partial t} = -\frac{1}{\rho_s}\frac{\partial p}{\partial z} - g\frac{\rho}{\rho_s} + \dot{w}, \tag{C.1a}$$

$$\frac{\partial \rho}{\partial t} + \frac{\partial}{\partial z}(\rho_s w) = \dot{\rho}_{ph} + \dot{\rho}_{co}, \tag{C.1b}$$

$$\frac{\partial \theta}{\partial t} + w\frac{d\theta_s}{dz} = \frac{\theta_s}{c_v T_s}\dot{q} + \frac{\theta\theta_s}{\rho_s}\dot{\rho}_{ph}, \tag{C.1c}$$

$$\frac{p}{p_s} = \frac{\rho}{\rho_s} + \frac{\theta}{\theta_s}, \tag{C.1d}$$

where most variable have the same meaning as in section 2.1 except the moist air density is $\rho = \rho_a(1 + r)$ where ρ_a is the dry air density, r is mixing ratio, $\gamma = c_p / c_v$ is the ratio of specific heats for dry air, θ is the virtual potential temperature, $\varepsilon = 1/\gamma - 1$ is a parameter of the heating due to the introduction of mass through phase change $\dot{\rho}_{ph}$, $\dot{\rho}_{co}$ represents mass redistribution by convective motions, $\dot{q}$ is an external heating rate, and $\dot{w}$ is an injection of vertical velocity. The form of (C.1) is very similar to the horizontally homogeneous limit of the dry set (2.1). The only significant differences are that 1) the density and potential temperature are redefined, and 2) the injection of moisture is

explicitly coupled to an injection of heat representing condensational warming or evaporational cooling

As in section 2.1, it is convenient to introduce the mass-weighted field variable transformation (2.3). The transformed injections are

$$\dot{W} = \rho_s^{1/2}\,\dot{w}\ ,\quad \dot{R}_{ph} = \rho_s^{1/2}\,\dot{\theta}_{ph}\ ,\quad \dot{R}_{co} = \rho_s^{1/2}\,\dot{\theta}_{co}\ ,$$
$$\dot{S} = \frac{\rho_s^{1/2}}{C_{vm}\,\theta_s}\,\dot{q}\quad . \tag{C.2}$$

We now seek the steady-state solution to the nonhomogeneous system (C.1). The statement of potential vorticity conservation for this system is

$$\frac{\partial Q}{\partial t} = g\left(\frac{\partial}{\partial z} - \frac{1}{2H_s}\right)\dot{S} - N_s^2\,\dot{R}_{co} + \left[\theta\, g\left(\frac{\partial}{\partial z} - \frac{1}{2H_s}\right) - N_s^2\right]\dot{R}_{ph}\ , \tag{C.3}$$

where mass-weighted PV (section 4.2) is defined here as

$$Q = g\left(\frac{\partial}{\partial z} - \frac{1}{2H_s}\right)S - N_s^2\,R\quad . \tag{C.4}$$

In the one-dimensional Lamb's problem, the injection of momentum does not generate a PV anomaly. Integrating (C.2) over all time and using the hydrostatic and geostrophic relations yields an equation governing the steady-state pressure,

$$\left[\frac{d^2}{dz^2} - \frac{1}{4H_s^2}\right]P_f = \left(\frac{\partial}{\partial z} - \frac{1}{2H_s}\right)\int_0 \dot{S}\,dt - N_s^2\int_0 \dot{R}_{co}\,dt + \left[\theta\, g\left(\frac{\partial}{\partial z} - \frac{1}{2H_s}\right) - N_s^2\right]\int_0 \dot{R}_{ph}\,dt\quad . \tag{C.5}$$

The Green's function of (C.5) satisfies

$$\left[\frac{d^2}{d z^2} - \frac{1}{4 H_s^2}\right] g_f(z \mid z_0) = \delta(z - z_0) \quad . \tag{C.6}$$

The steady-state response to a generalized nonhomogeneous term on the right hand side of (C.5) of the form δ_z is

$$P_f(z) = \int_0 g_f(z \mid z_0)\, \delta_z(z_0)\, d z_0 \quad . \tag{C.7}$$

If we require that the steady state pressure field be bounded at $z \to$ and that $w = 0$ at $z = 0$, i.e.

$$\left(\frac{d}{d z} + \alpha\right) P_f = 0 \quad at \;\; z = 0 \;\; , \tag{C.8}$$

then the Green's function is

$$g_f(z \mid z_0) = - H_s \exp\left(-\frac{|z - z_0|}{2 H_s}\right) - \frac{H_s}{\alpha} \exp\left(-\frac{z + z_0}{2 H_s}\right). \tag{C.9}$$

The second term in (C.9) represents the direct effect of the lower boundary at $z = 0$. If we replace the rigid lower boundary condition with a boundedness condition at $z \to -$ then we retrieve only the first term in (C.9). Suppose the time-integrated injection is given by

$$\int_0 \dot{\delta}\, dt = \bar{F}_\delta(z) \quad . \tag{C.10}$$

Note that (C.10) isolates the vertical structure of the injection. Then we may generalize the solution (C.7) as

$$P_f(z) = \int_0 K_\delta(z \mid z_0)\, \bar{F}_\delta(z_0)\, d z_0 \;\; , \tag{C.11}$$

where $K_{\alpha}(z \mid z_0)$ is the kernel function for an external injection of the quantity α whose time integrated vertical structure is given by $\overline{F}_{\alpha}$. These kernel functions are determined using (C.9)), the form of the operators acting on the injections in (C.5) , as well as the requirement that the injection be zero on the boundary:

$$K_q(z \mid z_0) = g\, H(z - z_0) \exp\left(-\frac{z - z_0}{2 H_s}\right), \tag{C.12a}$$

$$K_{co}(z \mid z_0) = g\, \alpha \exp\left(-\frac{|z - z_0|}{2 H_s}\right) + \frac{g}{\alpha} \exp\left(-\frac{z + z_0}{2 H_s}\right), \tag{C.12b}$$

$$K_{ph}(z \mid z_0) = \alpha K_q(z \mid z_0) + K_{co}(z \mid z_0) \quad . \tag{C.12c}$$

The second term in (C.12b) represents the effect of the lower boundary on the acoustically adjusted state (AAS) following a mass injection. No such term exists in (C.12a) because the AAS is insensitive to the existence of a lower boundary when forced by heating. The simple reason for this is that a heating cannot change the total weight of the fluid column in this one-dimensional adjustment problem. Similarly, the solution (C.12) indicates that no pressure perturbation may develop beneath an injection of heat, the reason for which is that the hydrostatic pressure perturbation is directly proportional to the change in the total column mass. Similarly, a change in pressure may be induced beneath a mass injection if and only if the mass injection does not conserve the total column mass.

Figure C.1 presents some examples of the steady-state solution (C.12) following injection of heat, “dry” mass, and moisture. The net vertical displacement $\alpha = \alpha z\,(t \alpha \quad)$ is computed in a manner similar to (3.2) . The first row of solutions in Fig C.1 represents the response to a top-hat injection of depth 5 km elevated 2 km above the lower

boundary. The response to each injection type is a positive pressure perturbation and a net upward expansion of the disturbed region with maximum displacement aloft. The maximum pressure perturbation following the heat injection is located at the top of the heating, whereas that following a mass injection is located on the lower boundary. As discussed above, the increase in the total weight of the column following the mass injection contributes significantly to the steady state pressure. Furthermore, the heat injection induces only net upward expansion with minimum at the bottom and maximum at the top of the disturbed region. In contrast, the mass injection induces some sinking at the bottom of the disturbed region. The response to injection of moisture incorporates features of the response to both mass and heat injection

The second row of solutions in Fig C.1 represents the response to a sinusoidal injection that is positive aloft and negative below. The steady state response is of smaller magnitude than that which followed the top-hat injection. Because the sinusoidal mass injection does not change the total weight of the column there is no surface pressure perturbation in the steady state. The pressure perturbation following the heat injection is negative with maximum amplitude in the center of the disturbed region - a much different profile than that following the top-hat heating. Net sinking occurs within the disturbed region with slighter sinking (rising) aloft following the heat (mass) injection. Unlike the net vertical displacement following a top-hat moisture injection, the response to a sinusoidal moisture injection is of larger amplitude than either the heat or mass injection both inside and disturbed region and aloft.

The small set of solutions represented in Fig. C.1 demonstrates several interesting qualities of Lamb's adjustment. The details of the hydrostatic steady state depend sensitively on the details of the injection. Comparison of Fig C.1b to Fig C.1e indicates that cooling located beneath a region of warming may completely reverse the sign of the hydrostatic pressure perturbation from positive to negative. The response to a moisture injection, which involves both heat and mass injection, is not always a simple combination of the response to similar mass and heat injection. In fact, it is possible (Fig. Ce,f) for the response to the moisture injection to be of larger amplitude than that following either a similar mass or heat injection.

Figure C.1

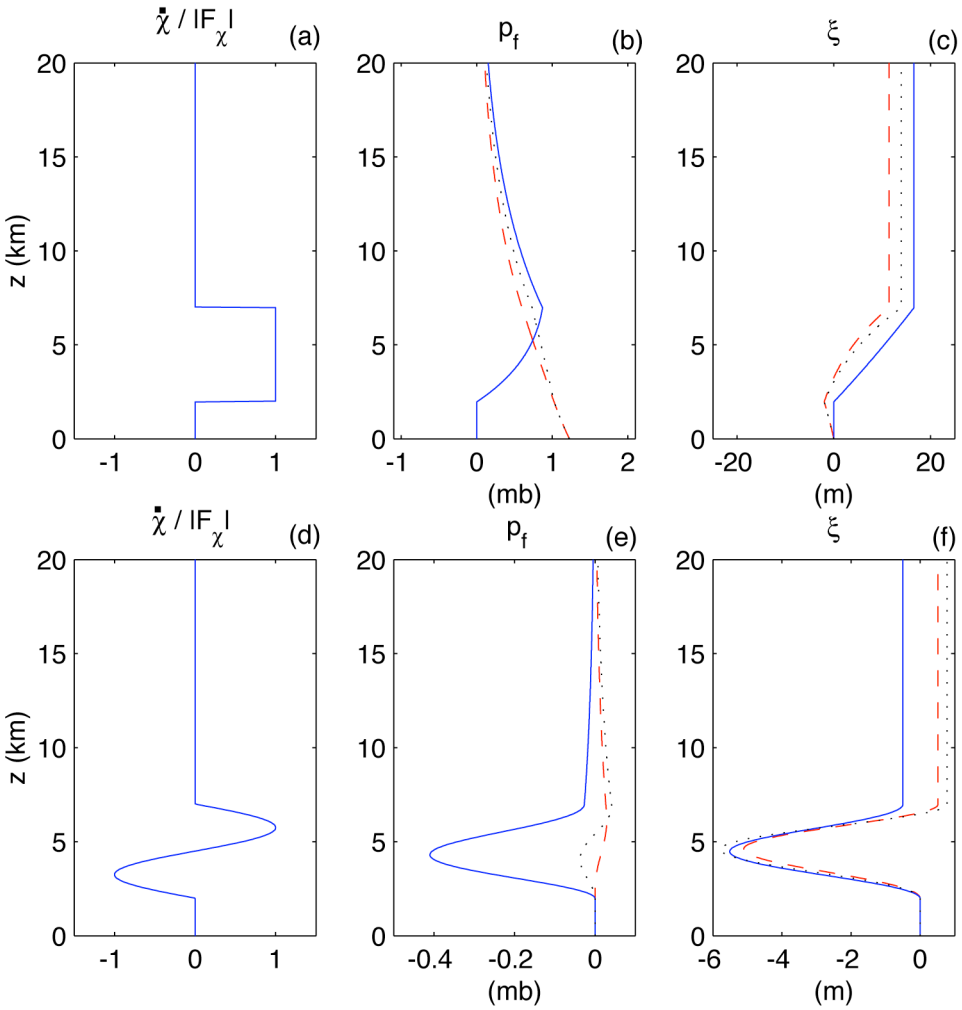

Figure C.1: Profiles of the steady-state (b,e) pressure field, and (c,f) vertical displacement field following injection of heat (solid lines), mass (dashed lines), and moisture (dotted lines) of amplitude 1 K and 2.5 g/m^3 whose geometry is (a) a top hat and (d) sinusoidal.

Appendix D

Transient Response of an Anelastic Atmosphere to Sources of Hydrostatic and Geostrophic Imbalance

The purpose of this appendix is to examine the response of an anelastic atmosphere to rapid, localized injection of heat, mass, or momentum. In chapter 2, we produced a prototypical solution of this adjustment problem in a fully compressible model linearized about an isothermal, resting base state. Here, we make all the same assumptions about the linearization procedure and qualities of the injection functions, but we also make the anelastic approximation. This approach will allow for a direct comparison between the transient solutions in the fully compressible and anelastic contexts.

This analysis potentially has practical, technical value. Fully compressible dynamics are being incorporated into the latest generation of numerical models of atmospheric flow. Although such models are ideal in a theoretical sense, they also potentially introduce a number of practical difficulties affecting the cost of integration and clarity of results. An anelastic model could alleviate some of these problems, but what are the specific costs of this approximation? Do they outweigh the gains? A detailed analysis of the consequences of this approximation on the accurate representation of such basic dynamical processes as hydrostatic and geostrophic adjustment is required. The analysis presented in this appendix will not answer these questions completely, but will

supply information with which an informed decision can be made regarding the prudence of anelastic versus fully compressible models.

The formalism describing the evolution of perturbations about an isothermal resting base state on an *f*-plane, excited by external injection of heat, mass, and momentum is described in chapter 2. We therefore skip much of the introduction, and will proceed to describe the anelastic approximation to this model. The mass conservation and Poisson's relations are respectively

$$\Box_a \frac{\partial \Box}{\partial t} + \frac{\partial}{\partial x}(\Box_s u\Box) + \frac{\partial}{\partial z}(\Box_s w\Box) = \Box \quad , \tag{D.1a}$$

$$\frac{\Box}{\Box_s} = \frac{p\Box}{\Box p_s} - \frac{\Box}{\Box_s} \quad , \tag{D.1b}$$

where $\Box_a$ is a flag denoting the anelastic approximation [= 1, compressible; = 0, anelastic] as is $\Box_*$ [= $\Box$= 7/5, compressible; = 1, anelastic]. The remaining equations in the governing set of (2.1) are unchanged by the anelastic approximation. The meaning of the field variable transformation is also unchanged by the anelastic approximation. The boundary condition in terms of the field variable transformation is therefore

$$\left(\left(\frac{\partial}{\partial z} + \Box_*\right)U \ , \left(\frac{\partial}{\partial z} + \Box_*\right)V \ , W, S, \left(\frac{\partial}{\partial z} + \Box_*\right)P\right) = \underset{\sim}{0}^{\mathbf{T}} \ , z = 0, 2D \quad , \tag{D.2}$$

where Eckart's (1960) vertical expansion coefficient is generalized as

$$\Box_* \equiv \left(\frac{1}{\Box_*} - \frac{1}{2}\right)\frac{1}{H_s} \ . \tag{D.3}$$

The expansion coefficient $\Box_*$ is larger in the anelastic approximation ($1/2H_s$) than in the compressible model ($.214/H_s$). This implies that the gradient of the anelastic pressure field in the vicinity of the boundary is larger than in the fully compressible case. This

may typically be realized as a larger pressure perturbation along the boundary. In the anelastic atmosphere, any vertical mass convergence must immediately be compensated by horizontal mass divergence. Therefore, the mass convergence that occurs in the vicinity of the rigid boundary may produce an exaggerated pressure perturbation to accomplish this horizontal mass divergence. In the compressible case, the vertical mass convergence may result in a local increase in the density field.

The diagnostic form of the anelastic continuity equation (D.1a) reduces the order of the linear system (2.4) from fifth order in time to third order. To demonstrate this explicitly, we may derive a single equation from (2.4) with (D.1a,b) for the evolution of the pressure field,

$$L\left\{\frac{\partial P}{\partial t}\right\} = \sum_{\square = S, U, V, W, R} M_{\square}(F_{\square}), \tag{D.4}$$

where

$$L = \frac{1}{c_*^2}\left[\square_a\left(\frac{\partial^2}{\partial t^2} + f^2\right) - c_*^2 k^2\right]\left[\frac{\partial^2}{\partial t^2} + N_s^2\right] - \left[\frac{\partial^2}{\partial t^2} + f^2\right]\left[\frac{\partial^2}{\partial z^2} - \square_*^2\right], \tag{D.5a}$$

$$M_S = \left[\frac{\partial^2}{\partial t^2} + f^2\right]\left[\square_a\left(\frac{\partial^2}{\partial t^2} + N_s^2\right) - g\left(\frac{\partial}{\partial z} - \square_*^2\right)\right], \tag{D.5b}$$

$$M_U = -ik\left[\frac{\partial^2}{\partial t^2} + N_s^2\right]\left[\frac{\partial}{\partial t}\right], \tag{D.5c}$$

$$M_V = -ifk\left[\frac{\partial^2}{\partial t^2} + N_s^2\right], \tag{D.5d}$$

$$M_R = \left[\frac{\partial^2}{\partial t^2} + N_s^2\right]\left[\frac{\partial^2}{\partial t^2} + f^2\right], \tag{D.5e}$$

$$M_W = -\left[\frac{\partial^2}{\partial t^2} + f^2\right]\left[\frac{\partial}{\partial z} - \square_*\right]\left[\frac{\partial}{\partial t}\right], \tag{D.5f}$$

and $c_*^2 = \gamma R T_s$ .We could have just as well formulated the problem of chapter 2 in this manner to solve for the pressure field subject to the injections. However, in this approach the retrieval of the other fields from the pressure field is a difficult task. It is much simpler to solve for the structure of the solution state vector via the eigenvector approach. Such an approach is possible in the anelastic case when the system is written in terms of the tendency of horizontal divergence, vertical vorticity, and potential temperature. Nonetheless, we proceed with the solution of (D.4) subject to the initial and boundary conditions (D.2) and (D.3) because it provides the most convenient framework for comparing the anelastic to the fully compressible solution. An analogy to the structure of the homogeneous solution state vector in the fully compressible case is made in order to determine the structure of homogeneous solution state vector in the anelastic case.

Consider the properties of the homogeneous solutions of (D.4). We seek a separable solution to the vertically and temporally dependent Fourier modes, e.g.

$$P(z,t) = f(z)\,h(t) \quad . \tag{D.6}$$

Here and subsequently we have dropped the notation that explicitly indicates dependence on the parameter *k* of the Fourier transform. Substituting (D.6) into the homogeneous form of (D.4), we obtain the vertical and temporal structure equations,

$$f''(z) + m^2 f(z) = 0 \quad , \tag{D.7a}$$

$$\alpha_a h''(t) + \beta h'(t) + \gamma h(t) = 0 \quad , \tag{D.7b}$$

where

$$\begin{aligned} \beta &= \left(c_*^2 k^2 + \alpha_a f^2\right) + c_*^2\left(\alpha_*^2 + m^2\right) + \alpha_a N_s^2 \quad , \\ \gamma &= c_*^2 f^2\left(\alpha_*^2 + m^2\right) + N_s^2\left(c_s^2 k^2 + \alpha_a f^2\right) \quad . \end{aligned} \tag{D.8}$$

Equation (D.7a) is identical to (2.11a). The structure equations are related by a vertical decay scale, *m*. As in chapter 2, section 2, we identify equation (D.7a) with prescribed boundary conditions as a Sturm-Liouville boundary-value problem. The set of all solutions to the Sturm-Liouville problem is an orthogonal basis set for all piecewise continuous functions between the boundary points. The homogeneous solution to (D.4) may therefore be expressed as a linear combination of these basis functions. If we impose the finite atmosphere boundary condition (D.3), then the vertical basis functions are,

$$\begin{gathered} f_0 , f_1 , f_2 , f_3 , \ldots \ ; \\ f_0 = e^{-m z} \ where \ m = \alpha_* \ , \\ f_n = m \cos[m z] - \alpha_* \sin[m z] \quad where \quad m = \frac{n \pi}{2 D} \ . \end{gathered} \tag{D.9a}$$

The set (D.9a) is identical to the set (2.11a) except for the definition of the expansion coefficient α_*, as explained above. Each of the functions in (D.9a) has a corresponding temporal structure, *h(t),* which is a general solution to the temporal structure equation (D.7b). The corresponding set of temporal structure functions is

$$\begin{gathered} h_0, h_1 , h_2 , h_3 , \ldots \ ; \\ h_n = C_1 + \left(C_2 e^{-i \omega_a t} + C_3 e^{i \omega_a t}\right) + \alpha_i \left(C_4 e^{-i \omega_b t} + C_5 e^{i \omega_b t}\right) , \end{gathered} \tag{D.9b}$$

where the coefficients C_i have the same meaning as in (2.19) and are determined by initial conditions, and ω_a and ω_b are the high and low positive roots, respectively, of the dispersion relation

$$\omega^2_{a,b} = \frac{1}{2}\left(\sigma \pm \sqrt{\sigma^2 - 4 \kappa}\right) . \tag{D.10}$$

The higher root ω_a is characteristic of an acoustic wave and the lower root ω_b is characteristic of a buoyancy wave. In the anelastic approximation only the lower root exists. The frequency given by ω_0 with the corresponding vertical structure function f_0

defines the Lamb wave, which is absent in the anelastic approximation. The anelastic approximation therefore completely filters acoustic waves from the solution. Furthermore, the anelastic approximation affects the frequency of buoyancy waves (particularly at high frequency).

The structure of the other fields are related to the pressure field by the set

$$\left[\frac{\partial^2}{\partial t^2} + f^2\right] U = i k \frac{\partial P}{\partial t} + \frac{\partial F_U}{\partial t} + f F_V \quad , \tag{D.11a}$$

$$\left[\frac{\partial^2}{\partial t^2} + f^2\right] V = -i k f P + \frac{\partial F_V}{\partial t} - f F_U \quad , \tag{D.11b}$$

$$\left[\frac{\partial^2}{\partial t^2} + N_s^2\right] W = -\left[\frac{\partial}{\partial z} + \square_*\right] \frac{\partial P}{\partial t} + \frac{\partial F_w}{\partial t} + g F_s \quad , \tag{D.11c}$$

$$\left[\frac{\partial^2}{\partial t^2} + N_s^2\right] S = \frac{N_s^2}{g}\left[\frac{\partial}{\partial z} + \square_*\right] P + \frac{\partial F_S}{\partial t} - \frac{N_s^2}{g} F_W \quad . \tag{D.11d}$$

In (D.11), the pressure terms are considered nonhomogeneous forcings in addition to the injection terms. The homogeneous solutions to (D.11a,b) and (D.11c,d) are pure inertial oscillations arising from the Coriolis and buoyancy forces, respectively. However, the initial conditions (D.2) imply that the general solution to (D.11) includes only the particular part. If we consider solutions to the homogeneous system (2.1) with (D.1), then the solution is only comprised of the particular solution corresponding to the nonhomogeneous pressure term. The homogeneous solutions for U and V are therefore described by the same set of vertical basis functions as P but those for S and W are described by a new set of basis functions that are identically zero on the lower boundary as in (2.12b),

$$g_n = \left[\frac{d}{d z} + \square_*\right] f_n = -\left(m^2 + \square_*^2\right) \sin[m z] \quad \text{where} \quad m = \frac{n \square}{2D} \quad . \tag{D.12}$$

$$g_1, g_2, g_3, \ldots$$

The anelastic approximation does not affect the structure of the individual modes describing the vertical velocity and entropy fields (D.12).

For the compressible case, the structure of the homogeneous solution implied by (D.11) must be the same as that given by the eigenvalue-eigenvector procedure in (2.19). Because the system (D.11) is of the same general form for the anelastic approximation, we conclude that the structure of the buoyancy-wave and steady classes must resemble that in the compressible atmosphere. We may therefore generalize the homogeneous solution state vector (2.19) to include the anelastic approximation:

$$\underset{\sim}{\square}_n = \begin{bmatrix} 0 & \frac{-k\,\square_a}{f^2 - \square_a^2} & \frac{k\,\square_a}{f^2 - \square_a^2} & \frac{-k\,\square_b}{f^2 - \square_b^2} & \frac{k\,\square_b}{f^2 - \square_b^2} \\ \frac{i\,k}{f} & \frac{i\,k\,f}{f^2 - \square_a^2} & \frac{i\,k\,f}{f^2 - \square_a^2} & \frac{i\,k\,f}{f^2 - \square_b^2} & \frac{i\,k\,f}{f^2 - \square_b^2} \\ 0 & \frac{i\,\square_a}{N_s^2 - \square_a^2} & \frac{-i\,\square_a}{N_s^2 - \square_a^2} & \frac{i\,\square_b}{N_s^2 - \square_b^2} & \frac{-i\,\square_b}{N_s^2 - \square_b^2} \\ \frac{1}{g} & \frac{\square / H_s}{N_s^2 - \square_a^2} & \frac{\square / H_s}{N_s^2 - \square_a^2} & \frac{\square / H_s}{N_s^2 - \square_b^2} & \frac{\square / H_s}{N_s^2 - \square_b^2} \\ 1 & 1 & 1 & 1 & 1 \end{bmatrix}_n \begin{bmatrix} C_1 \\ \square_a\ C_2\, e^{-i\,\square_a t} \\ \square_a\ C_3\, e^{i\,\square_a t} \\ C_4\, e^{-i\,\square_b t} \\ C_5\, e^{i\,\square_b t} \end{bmatrix}_n . \tag{D.13}$$

The solution state vector $\underset{\sim}{\square}_n$ is defined in chapter 2. In summary, the effect of the anelastic approximation on the homogeneous solution is 1) elimination of the acoustic and Lamb waves from the solution, 2) an increase in the magnitude of the vertical expansion coefficient, and 3) a decrease in the frequency of high frequency buoyancy waves.

Next, we consider solution of the nonhomogeneous system (2.4). In the general context of this appendix, the system takes the form

$$\frac{d}{dt}\begin{bmatrix} U_n \\ V_n \\ W_n \\ S_n \\ P_n \end{bmatrix} + \underset{\sim}{\mathbf{A_n}}\,\underset{\sim}{\mathbf{\Phi_n}} = \underset{\sim}{\mathbf{F_n}} \quad , \tag{D.14}$$

where

$$\underset{\sim}{\mathbf{A_n}} = \begin{bmatrix} 0 & -f & 0 & 0 & ik \\ f & 0 & 0 & 0 & 0 \\ 0 & 0 & 0 & -g & 1 \\ 0 & 0 & \frac{}{H_s} & 0 & 0 \\ ik\,c_*^2 & 0 & -c_*^2\left(m^2+ \right) & 0 & 0 \end{bmatrix} , \tag{D.15}$$

and $\underset{\sim}{\mathbf{F_n}}$ has the same meaning as in chapter 2 except in the anelastic approximation the pressure injection does not contain a contribution from the heating, $\dot{P} = c_*^2\left(\dot{R} + \dot{S}\right)$. Let us consider the Green's function solution of (D.14) where $\underset{\sim}{\mathbf{F}}_n = \underset{\sim}{\hat{\mathbf{F}}_\mathbf{n}}\,(t)$ and (t) is the Dirac delta function. In the fully compressible atmosphere we obtain the solution presented in chapter 3, section 3 and appendix A. The anelastic solution is not as straightforward. Because the mass conservation equation is diagnostic, we are unable to assume that the fields are bounded at $t = 0$. Rather, the instantaneous injection of mass must be accompanied by an instantaneous mass divergence, according to (D.1a). We are therefore unable to assume that the integral of $\underset{\sim}{\mathbf{A_n}}\,\underset{\sim}{\mathbf{\Phi_n}}$ about an infinitesimal region containing $t = 0$ is zero.

Alternatively, we turn to the nonhomogeneous form of the pressure tendency equation (D.4). In the same manner as before, we expand the injection terms about the

vertical basis functions. The injection term acting on the n-th basis function has the general form

$$M_{n,\square}(F_{n,\square}) = \square_{n,\square}(t) \quad , \tag{D.16}$$

where $\square_{n,\square}$ is depends on the injection type and geometry. The equation governing the evolution of the n-th contribution to the pressure field is

$$\left\{\frac{1}{c_*^2}\left[\square_a\left(\frac{d^2}{dt^2} + f^2\right) + c_*^2 k^2\right]\left[\frac{d^2}{dt^2} + N_s^2\right] + \left[\frac{d^2}{dt^2} + f^2\right]\left[m^2 + \square_*^2\right]\right\}\frac{dP_n(t)}{dt} = \square_{n,\square}(t) \quad . \tag{D.17}$$

Because $\square_{n,\square}$ is a complicated function of the injection mechanism (D.5), it is most convenient to solve (D.17) via a Laplace transform, e.g.

$$\begin{aligned} L_T[f(t)] &= f^{\square}(\square) = \int_0 f(t)\, e^{-\square t}\, dt \quad , \\ L_T^{-1}[f^{\square}(\square)] &= f(t) = \frac{1}{2\square i}\int_{c-i}^{c+i} f^{\square}(\square)\, e^{\square t}\, d\square \quad . \end{aligned} \tag{D.18}$$

We now seek the temporal Green's function solution $\widehat{P}_n$ for which the nonhomogeneous term in (C.17) is a function of higher order delta functions according to (D.5), which we denote $\widehat{\square}_{n,\square}(t)$. As in chapter 3, section 3, it may be shown that the solution corresponding to an arbitrary temporal injection $\square_t$ is related to the Green's function via the convolution:

$$P_n(t) = \int_0^t \widehat{P}_n(t - t\square)\,\square_t(t\square)\, dt\square \quad . \tag{D.19}$$

The Laplace transformed solution for the Green's function for the fully compressible solution is given by

$$\hat{P}_n^{\square}(\square) = \frac{c_*^2 \hat{\square}_n^{\square}(\square)}{[\square][\square^2 + \square_a^2][\square^2 + \square_b^2]}, \quad n \geq 1$$
$$\hat{P}_0^{\square}(\square) = \frac{c_*^2 \hat{\square}_0^{\square}(\square)}{[\square][\square^2 + \square_0^2][\square^2 + N_s^2]}, \quad n = 0, \tag{D.20a}$$

and for the anelastic approximation is

$$\hat{P}_n^{\square}(\square) = \frac{c_*^2 \hat{\square}_n^{\square}(\square)}{\square[\square][\square^2 + \square_b^2]}, \quad n \geq 1$$
$$\hat{P}_0^{\square}(\square) = \frac{c_*^2 \hat{\square}_0^{\square}(\square)}{\square[\square][\square^2 + N_s^2]}, \quad n = 0 . \tag{D.20b}$$

The denominator of the solution (D.20a) indicates three potential sources of the solution: a $\square = 0$ source corresponding to the steady state, a $\square = i\square_a$ source corresponding to an acoustic wave, and a $\square = i\square_b$ source corresponding to a buoyancy wave. For the Lamb mode $\square = iN_s$ is not a source; the function in the numerator is proportional to this term. These are precisely the eigenvalues we found in chapter 2, section 2. [Note: The function in the numerator does not contain any singularities]. The acoustic-wave class is, once again, filtered from the anelastic solution (D.20b). The inverse transform of (D.20) indicates that the Green's function resembles a solution to the homogeneous system,

$$\hat{P}_n(t) = A_n + \square_a (B_n \cos(\square_a t) + C_n \sin(\square_a t)) + D_n \cos(\square_b t) + E_n \sin(\square_b t), \tag{D.21}$$

where the coefficients are provided in table D1. It may be shown that the solution for the fully compressible atmosphere is identical to that obtained in section 2.3 and appendix A.

Consider a heat injection of the form (3.1) with geometry and duration the same as that applied in section 3.2.1 (i.e. d_g = 1km, d = 5 km, a = 2 km, $\square$ 0). The anelastic response to this cumulus-scale heating is compared to the fully compressible solution of

section 3.2.1. The largest difference is apparent during the acoustic stage (Fig. D.1). The initial anelastic pressure field is of considerably smaller amplitude (approximately 21 mb) than that generated in the fully compressible model (see Fig. 3.3). The filtering of the acoustic waves results in a smooth relaxation of the pressure field by the buoyancy waves during the first several minutes following the heating. The buoyancy-wave response in the anelastic model is compared to that in the compressible model by examining the evolution of the potential temperature field (Fig. D.2). The remarkable similarity between these models indicates that the anelastic model approximates the shape and speed of the nonhydrostatic buoyancy-wave adjustment quite well, with slight differences appearing in the wave amplitude.

Table D.1: Coefficients of the Green's function solution for the field variable transformation of pressure subject to injections of heat, mass, and momentum. To obtain the coefficients of the Lamb mode, let $m = i\alpha$ and $D_n = E_n = 0$. When the anelastic approximation is used, $a_- = -1$, $a_1 = a_2 = \alpha$. When the model is compressible, $a_- = 1$, $a_1 = \alpha_b^2 - \alpha_a^2$, $a_2 = \alpha_a^2$.

injection type	**steady state**	**acoustic**	**buoyancy**
S	$A_n = \frac{\alpha_a \left(f^2 N_s^2\right) s_n + g f^2 \left(m^2 + \alpha_*^2\right) \tilde{s}_n}{a_2 \alpha_b^2}$	$B_n = \frac{\left(f^2 - \alpha_a^2\right)\left[\left(N_s^2 - \alpha_a^2\right) s_n + g \left(m^2 + \alpha^2\right) \tilde{s}_n\right]}{\alpha_a^2 \left(\alpha_a^2 - \alpha_b^2\right)}$ $C_n = 0$	$D_n = \frac{\left(f^2 - \alpha_b^2\right)\left[\alpha_b\left(N_s^2 - \alpha_b^2\right) s_n + g \left(m^2 + \alpha_*^2\right) \tilde{s}_n\right]}{\alpha_b^2 a_1}$ $E_n = 0$
U	$A_n = 0$	$B_n = 0$ $C_n = \frac{i k \left(N_s^2 - \alpha_a^2\right) s_n}{\alpha_a \left(\alpha_b^2 - \alpha_a^2\right)}$	$D_n = 0$ $E_n = \frac{i k \left(N_s^2 - \alpha_b^2\right) s_n}{\alpha_b a_1}$
V	$A_n = - \frac{i k f N_s^2 s_n}{a_2 \alpha_b^2} a_-$	$B_n = \frac{i k f \left(N_s^2 - \alpha_a^2\right) s_n}{\alpha_a^2 \left(\alpha_a^2 - \alpha_b^2\right)}$ $C_n = 0$	$D_n = \frac{i k f \left(N_s^2 - \alpha_b^2\right) s_n}{\alpha_b^2 a_1}$ $E_n = 0$
W	$A_n = 0$	$B_n = 0$ $C_n = \frac{\left(f^2 - \alpha_a^2\right)\left(m^2 + \alpha^2\right)}{\alpha_a \left(\alpha_b^2 - \alpha_a^2\right)}$	$D_n = 0$ $E_n = - \frac{\left(f^2 - \alpha_b^2\right)\left(m^2 + \alpha_*^2\right) \tilde{s}_n}{\alpha_b a_1}$
R	$A_n = \frac{f^2 N_s^2 s_n}{a_2 \alpha_b^2}$	$B_n = \frac{\left(f^2 - \alpha_a^2\right)\left(N_s^2 - \alpha_a^2\right)}{\alpha_a^2 \left(\alpha_a^2 - \alpha_b^2\right)}$ $C_n = 0$	$D_n = \frac{\left(f^2 - \alpha_b^2\right)\left(N_s^2 - \alpha_b^2\right) s_n}{\alpha_b^2 a_1}$ $E_n = 0$

Figure D.1

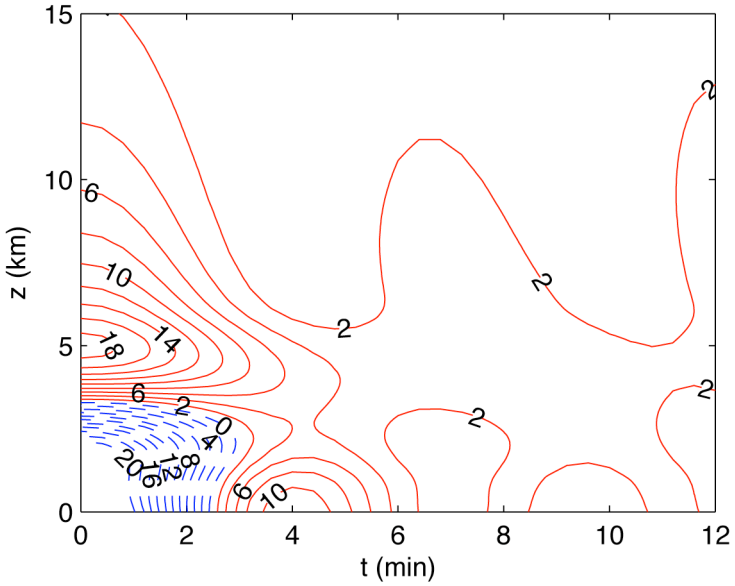

Figure D.1: Temporal cross section of the anelastic pressure field at $x = 0$ as a function of height z and time t following an impulsive injection of heat of amplitude 1 K. The contour interval is 1 Pa.

Figure D.2

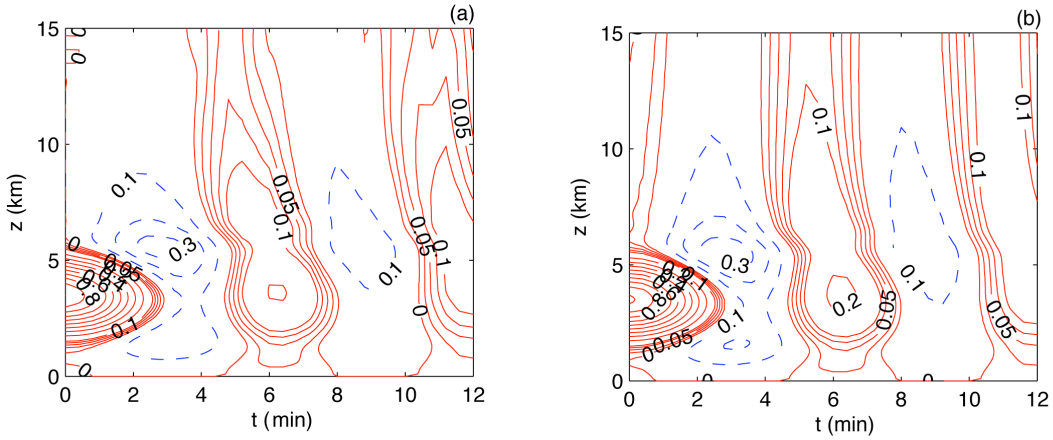

Figure D.2: Temporal cross section of the potential temperature field at $x = 0$ km as a function of height z and time t following an impulsive heating in (a) a fully compressible atmosphere and (b) an anelastic atmosphere. The contour interval is .025 K for |□□| < .1 K and .1 K otherwise.

VITA

Jeffrey M. Chagnon

Jeffrey M. Chagnon was born on September 29, 1975 in Patchogue, N.Y. His mother Kathryn (Haughey) is a registered nurse and his father Jeffrey L. Chagnon is a retired police detective. He has a younger sister Michelle, a younger brother Michael, and is married to Rachael A. Khoury from Altoona, PA.

Jeffrey attended elementary and secondary school in Miller Place, N.Y. and graduated in 1993. He earned a Bachelor of Science Degree in Meteorology and a Bachelor of Arts Degree in Mathematics from the State University of New York College at Oswego in 1997 with Summa Cum Laude honors. He then earned a Master of Science Degree in Meteorology from the Pennsylvania State University in 2001. For the 2001-2002 academic year, Jeffrey was awarded a Muan/Wilson Graduate Fellowship from the College of Earth and Mineral Sciences at the Pennsylvania State University.